EVOLUTION OF MICROSTRUCTURE IN Nb-BEARING MICROALLOYED STEELS PRODUCED BY THE COMPACT STRIP PRODUCTION PROCESS

by

Arturo Ruiz-Aparicio

BS, Universidad Nacional Autonoma de Mexico, 2000

Submitted to the Graduate Faculty of

the School of Engineering in partial fulfillment

of the requirements for the degree of

Master of Science in Materials Science and Engineering

University of Pittsburgh

2004

UNIVERSITY OF PITTSBURGH

SCHOOL OF ENGINEERING

This thesis was presented

by

Arturo Ruiz-Aparicio

It was defended on

May 14, 2004

and approved by

Dr. C. I. Garcia, Research Professor, Department of Materials Science and Engineering

Dr. P. Phule, Associate Professor, Department of Materials Science and Engineering

Thesis Advisor: Dr. A. J. DeArdo, William Kepler Whiteford Professor, Department of Materials Science and Engineering

EVOLUTION OF MICROSTRUCTURE IN Nb-BEARING MICROALLOYED STEELS PRODUCED BY THE COMPACT STRIP PRODUCTION PROCESS

Arturo Ruiz-Aparicio, MS

University of Pittsburgh, 2004

New steel processing technologies require an in-depth understanding of the processing-microstructure-property synergism of current and future steels. The need for this basic understanding is to improve the properties of the steels and to make them commercially more competitive. This study systematically examines the microstructure evolution in the as-cast and as-equilibrated conditions of two low-carbon Nb-bearing microalloyed HSLA steels commercially produced by the Compact Strip Production (CSP) process. Particular attention is paid to the precipitation that takes place through the processing conditions studied in this work. The formation of complex (Nb, Ti)(C, N) precipitates with a "star-like" shape was the primary type of precipitates found. The kinetics of formation and dissolution of the star-like precipitates at different re-heating temperatures is examined. A comparison between the as-cast, as-equilibrated and hot band conditions is also presented.

TABLE OF CONTENTS

LIST OF TABLES

LIST OF FIGURES

LIST OF SCHEMATIC DIAGRAMS

ACKNOWLEDGEMENTS

I want to dedicate this thesis work to my wonderful parents, sisters, brothers, niece and nephews, and the entire Ruiz-Aparicio family. Thank God I have you all and thank you all for the love and support I have always received from you. I would like to extend my appreciation and respect to my advisors Dr. C I Garcia and Dr. A J DeArdo for sharing their knowledge and guiding me throughout my graduate studies. Special thanks to Dr. K Goldman for his always wise advice and Dr. Hua for his patience and help with TEM and STEM. I express my gratitude to Dr. P Phule for being part of my defense committee. Thanks to the CSP-BAMPRI group for their contributions to this work, Dr. K Cho, Mrs. Wang, Mr. Ma, and W. Gao.

I want to thank Kasey for her unconditional support and all her love. Thanks to Suzanne for all her help and my brother, Luis, for his always intelligent advice, for sharing his knowledge with me during all my studies, and for making us, his family, the happiest in the world. Also, I would like to thank my friends Enrique, Andreas, Fabio, Margarita, Eric C, Augusto, Adrian, Octavio, Julio, Mario, Nacho, Khaled, Diego, Ritesh, Wu, Ani, Igor, Eric K, the MSE department., the fellows in Mexico and an endless list of people for their excellent friendship.

1.0 INTRODUCTION

One of the most important aspects in obtaining higher strength levels and ductility in microalloyed steels has been to control their microstructure.

The precipitation of micro alloying elements such as niobium (Nb), titanium (Ti), and vanadium (V) play a major role in controlling the microstructure and, hence, the mechanical properties, for instance, of high strength low alloy (HSLA) steel products acting as a hardenability enhancer and as a grain refiner.

The development of HSLA steels has been one of the most significant achievements in the past twenty years and their use has increased in the recent years, especially with the reduction of interstitial elements such as carbon for higher formability and better welding properties. They are used in the automotive industry for reducing weight to increase the mileage and in pipeline construction. Two commercial HSLA steels with different Nb and Ti contents were analyzed in this project.

The introduction of new technologies and improvements in the processing lines has led the steelmakers to great scientific and economical achievements. For instance, the reduction in plate thickness, 250 mm in conventional continuous casting (CCC) in the 60's, to the 50 mm slab thickness in thin slab casting (TSC) in the early 90's. TSC technology sprung as a promising process to open the flat rolled market to the minimills as it noticeably reduces the capital costs involved, decreases the size of the continuous casting machine required and at the same time eliminates the roughing mill.

The industry continues developing higher strength steel grades which are obtained by rapid cooling to achieve a finer ferrite grain size and dispersion hardening by carbides and carbo-nitrides. These steels contain nitrogen, phosphorous, silicon, manganese for solid solution strengthening and niobium, vanadium and titanium for precipitation hardening[1]. However, there is a great dependence of precipitation hardening on the size, volume fraction, interparticle spacing and solubility product of the precipitates.

TSC steel plants are shifting to the production of superior quality, value-added steels for other demanding applications such as appliances, automotive industry depending on the potential of their minimills. Examples of these steels are interstitial free steels [IF], with interstitial levels as low as 20 ppm, dual phase steels [DP], transformation induced plasticity steels [TRIP] and continue to develop new grades of HSLA steels while improving the properties of the already existing ones with the purpose of making them commercially more competitive.

The purpose of this research is to conduct a systematic microstructural characterization of two low-carbon commercial microalloyed HSLA steels with different levels of Nb, Ti and C, produced by the CSP (compact strip production) process. Particular attention is paid to the precipitation behavior in the as-cast and as-equilibrated conditions (prior to and after the equilibrating furnace respectively). Also, the kinetics of dissolution of the primary type of precipitates found is studied.

2.0 BACKGROUND

2.1 CONVENTIONAL CONTINUOUS CASTING OF STEEL (CCC)

The continuous production of ingots from the molten metal goes back to Bessemer's patent[2, 3, 4]. In this process, the metal was supposed to be fed into the water-cooled rolls of a sheet mill. Such method was not successful at that time due to technological difficulties.

At the beginning of the 20th century, several casting processes were patented all over the world, but it was not until after the Second World War that work on continuous casting was resumed; at that point, the basic principles of the casting machines were finalized.

During the 40's and 50's several experimental semi-continuous and continuous steel casting plants[5, 6, 7, 4] were built around the world.

Two main types of continuous caster may be distinguished: vertical and horizontal. The vertical is further divided into straight vertical, vertical with bending, and curved mold with straightening - Figure 1 a, b, and c respectively.

The continuous casting process consisted in feeding molten metal from the ladle into a water-cooled vertical mold in which the ingot would solidify. The ingot, with solid surface but still a liquid core, was forced out of the mould continuously into a zone of secondary cooling where the final solidification occurred[3].

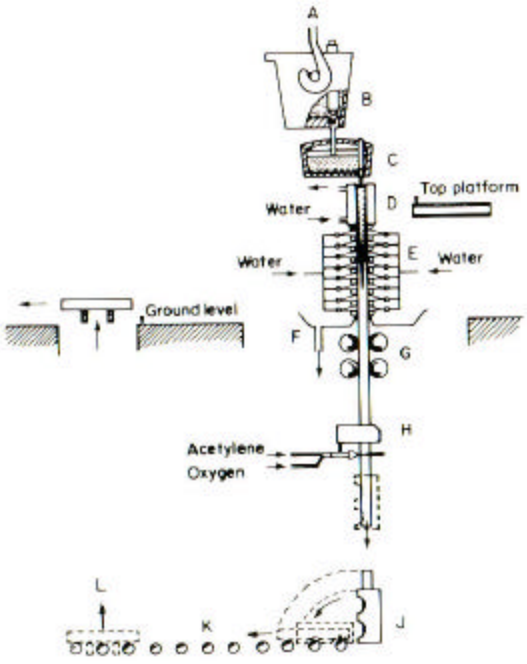
A
B
C
Top platform
Water
D
Water
E
Water
Ground level
F
G
H
Acetylene
Oxygen
L
K
J

(a)

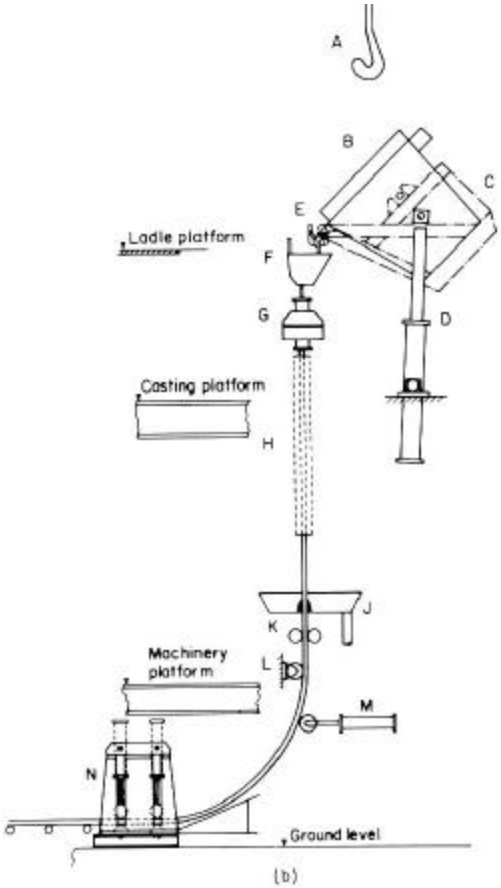
A
B
C
E
Ladle platform
F
G
D
Casting platform
H
J
K
Machinery platform
L
M
N
Ground level

(b)

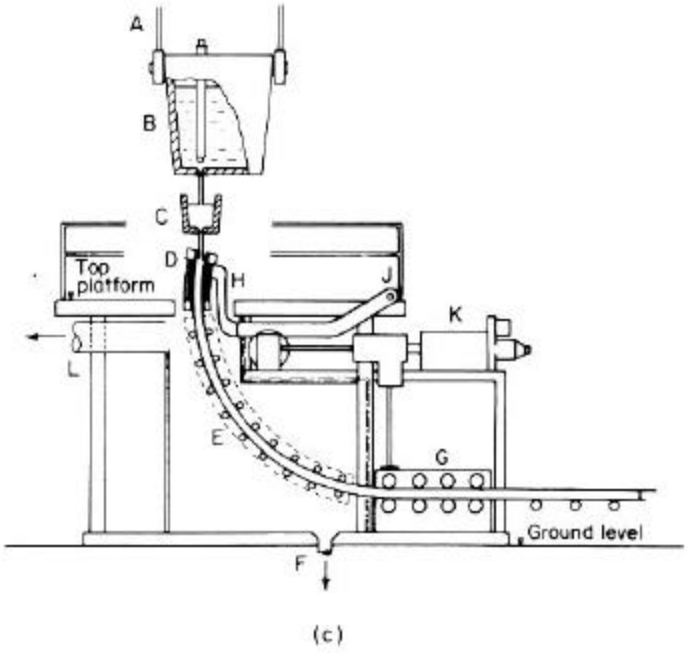

Figure 1 (a) Vertical continuous casting. (b) Vertical continuous casting with bending. (c) Curved mold continuous casting with straightening[8]

Several aspects[9] such as the properties of the liquid metal, the pouring of ingots, the molds, fluidity of steel[10, 11, 12], mechanism of solidification, melting process, the homogenization of the solidified metal, etc. have been of great importance since then in order to obtain the specific microstructural characteristics and the desired mechanical properties of the final product.

2.2 MINIMILLS

An innovative manufacturing process arose in the 60's, the Minimill Operation (MMO). The name minimill, according to M. M. Wolf[13], was applied to "…small electric furnace operators producing a limited assortment of unsophisticated long products like reinforcing bars, light structurals, and wire rods."

Minimills are associated with high productivity, with operations based on energy, materials, capital and labor savings. They have made great contributions to continuous casting, especially concerning a low cost production by directly charging the cast slabs to the rolling mill in a single heat to finished product size by different casting processes: billet casting, beam blank casting, and thin slab casting. Many minimills use electric arc furnace (EAF) for their melting process, scrap is used mostly, the refining process occurs in a separate ladle–furnace operation, and fast cooling is involved in the casting process followed by an equilibrating furnace where the thin slab enters and is taken to temperatures of up to 1150 ºC. At this temperature, the 50 mm slab is charged into a 5-6 stand finishing mill.

It is clear that the steel produced by means of the EAF makes a great difference compared to the conventional blast furnace and the Basic Oxygen Furnace (BOF).

2.2.1 Billet Casting

The production of low carbon steel rod, rebar and small shapes by billet casting as a near net shape casting process (NNSC) were successfully introduced after the

World War II. Billet casters were of vertical type or vertical/bending type[14]. In a time when the steel production was mainly from open hearth furnace (OHF) 80 % and the rest split between EAF and the Bessemer process, the EAF technology became the most adequate in terms of temperature control which would bring about production cost savings. In addition, the construction of tall buildings for vertical type casters was also a complication. This led to the design and creation of the curved mold in the mid 60's[15] - Figure 2, or alternatively the concept of strand bending with liquid core below the mold[16, 17, 18].

By developing a better billet casting mold, casting speed would be increased[19] ;however, in the late 80's, the industry found it hard to connect hot direct charging-rolling mostly due to the difficulty in matching between the casting and rolling schedule.

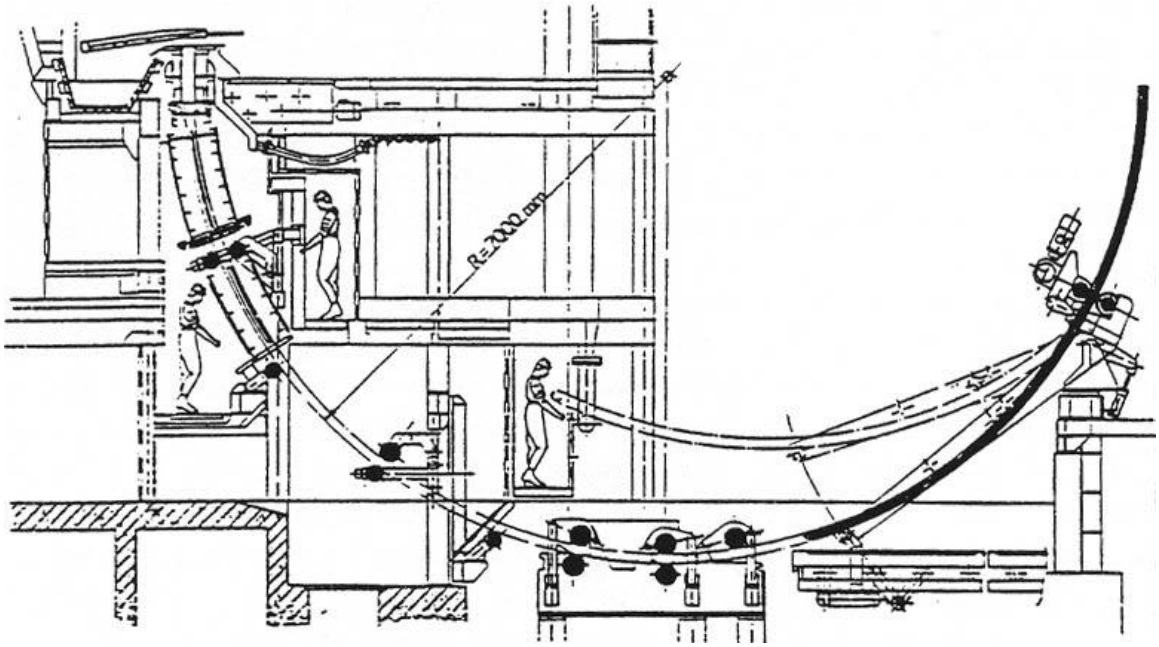

Figure 2 Curved mold billet caster with rigid dummy-bar[15]

2.2.2 Beam Blank Casting (BBC)

H-Beams are conventionally rolled out of large blooms, a powerful casting machine is required to achieve this as well as considerable rolling reduction on a blooming mill prior to section rolling requirements which do not fit well into a minimill structure.

The introduction of the beam blank casting (BBC) in the 60's and in the 70's made everything more simple, even though it was uncertain if the process would be cost effective[20].

Production of wide flange beams used to be made by the process route steel making-ingots-blooming-finish rolling. The introduction of the continuous casting technology made possible the production of rectangular blooms with the proper gauges. Continuous bloom casting technology offered some advantages such as improved quality properties of the continuous cast blooms, higher yields as it changed from ingots to continuously cast material, and savings by avoiding the reheating of ingots and blooming.

The near net shape beam blank sections with a very thin web of 50 mm thickness is a major contribution to minimill operations, which then led to Compact Beam Production (CBP).

In all cases of new installations, caster and rolling mill are closely connected to allow direct hot charging whenever it is possible, for instance BBC , which shows a significant impact on the cost-effectiveness of structural steel production.

2.2.3 Thin Slab Casting (TSC)

Through the years, solid foundations for a new promising technology were being built. The conventional slab casting (developed by the Integrated Steelmakers) was adopted and implemented by the minimills in the form of a Compact Strip Mill (CSM) or a full-fledged Hot Strip Mill (HSM).

In the search of economy, steel quality, superior properties, and very importantly, considering the environmental issues, modifications were made in the steelmaking industry; for instance, growth of scrap melting in the EAF and the rise of minimills, iron and steel refining in ladles, and continuous casting into semi-finished shapes.

The way was being traced for a viable, cost-effective and reproducible technology: The Thin Slab Casting (TSC) technology based on belt casters by the Hazlett-type primarily[21].

With the goal of increasing casting speeds for a thin slab section by conventional mold technology, SMS (Schloemann Mannesmann Siemag) built a pilot plant in Germany. The breakthrough was achieved with the implementation of the funnel-shaped mold – Figure 3. This evolutionary concept consisted in reducing the slab thickness of conventional cast steel from 250 mm to 50 mm.

Based on the pilot plant test promising results, Nucor Steel Corporation decided to commercialize the TSC process[13, 22, 18, 23, 17, 24] by building a plant in Crawfordsville, IN, USA in 1989, and later, another plant in Hickman, AR in 1992. TSC, as expected, resulted in a cost-effective, reproducible, and flexible process by reducing the size of the continuous casting machine and eliminating the roughing mill.

By the mid 90's only two processes had reached industrial application and had been commercially accepted: the Compact Strip Production (CSP) process of SMS and the In-Line Strip Production (ISP) process of Mannesmann Demag Huttentechnik (MDH), commercialized in Arvedi, Italy. Other caster builders did not remain inactive - Table 1. Processes such as the CONROLL process, the Danieli Thin Slab Conticaster, which rely on mold oscillation to provide the relative motion for lubrication between the mold and the strand; and the Belt Casters, whose functionality lies in reducing friction between the mold and the strand by continuously moving the cooling belts as fast as the slab [25, 26].

2.2.3.1 Compact Strip Production Process (CSP)

The CSP process, Figure 4, as well as other processes had to overcome certain problems regarding the feeding of the liquid into the mold, the geometry of the mold, its behavior and influence on steel quality[27], casting speeds, and the improvement of the as-cast structure, where segregation plays an important role for a superior quality of the final/rolled product[18].

The CSP – SMS casting machine is of the vertical type, 5.8 m tall, with in-line bending to a radius of 3.8 m. The mold, made of chromium-zirconium-copper with an immerse submerged entry nozzle (SEN), oscillates at 1 Hz per m/minute of casting speed with a stroke length of 6 mm. Alignment tolerances between the mold and the SEN are of critical importance to avoid breakouts. The SEN has to be ±3 mm aligned with the mold centerline and the mold must be aligned to within ±1 mm, while the roller apron alignment is set at ±0.2 mm below the mold. The length of the cast slabs in the

CSP process is 45 m. They are fed directly to an in-line roller hearth tunnel furnace (equalizing/soaking furnace). The temperature at which the slabs enter the furnace is about 1050 ºC, which is presumed to be a critical temperature for the formation of star-like precipitates[28, 29, 30]. The equalizing furnace, where the slab remains for 20 minutes for microstructure homogenization, raises and homogenizes the temperature of the slab to 1150 ºC prior to entering the rolling mill. The hot strip mill consists of 5-6 tandem finishing stands preceded by a high pressure descaler.

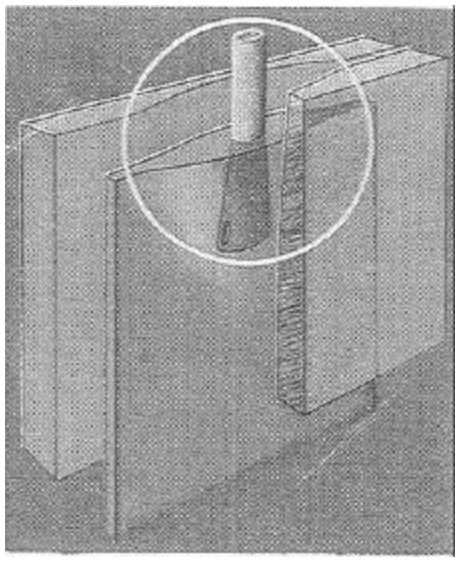

Figure 3 Schematic diagram of a funnel-shaped mold in the TSC-CSP process machine

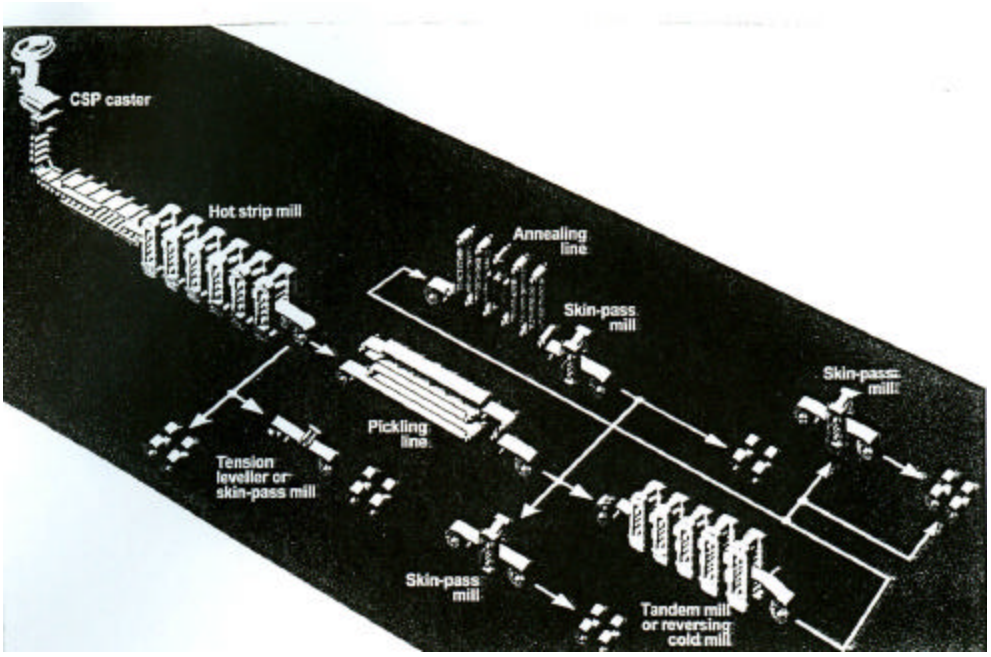

Figure 4 Overall material flow for strip production starting from a CSP caster

2.2.3.2 In-line Strip Production Process (ISP)

This process has the capability of casting 60 mm thick slabs. The type of mold is a vertical-bar type with flat parallel walls. Figure 5 shows the mold and SEN especially developed for the ISP process[31]. It has a vertical top section which falls into a curved lower part with a radius of 5 m. The SEN is about 40 mm thick by 160 mm wide. After the mold, it has in-line thickness reduction to 40 mm still containing a liquid slab core. The reduction is applied by a set of rolls located below the mold. After the mold, the strand passes through three pre-reduction stands, which in turn reduce the thickness to 15 mm.

In the Arvedi, Italy ISP line, the caster is connected to an induction furnace followed by a twin mandrel coil box (Cremona Furnace) and a four stand finishing mill.

Table 1 Commercial scale thin slab casting plants built as of 2000

COMPANY	LOCATION			Rated TS Capacity (MT/year)	Startup	Caster Machine
NORTH-AMERICA						
Nucor Steel	Crawfordsville	IN	USA	1.8	1989, 1994	CSP
Nucor Steel	Hickman	AR	USA	2	1992, 1994	CSP + ITSC
Nucor Steel	Berkley	SC	USA	1.5	1996	CSP
Steel Dynamics	Bulter	IN	USA	1.2	1996	CSP
Hylsa, SA	Monterrey		Mexico	0.9	1995	CSP
Gallatin Steel	Warsaw	KY	USA	1	1995	CSP
Acme Steel	Riverdale	IL	USA	1	1996	CSP
Algoma Steel	Sault Ste Marie	ONT	Canada	2	1997	ITSC
Armco	Mansfield	OH	USA	1.1	1993	Conroll
North Star/BHP Steel		OH	USA	1.35	1996	Sumitomo
Trico Steel		AL	USA	2.2	1996	Sumitomo
ASIA						
Hanbo Steel	Asan Bay		Korea	2	1995	CSP
Nippon Denro	Delvo		India	1.2	1996	CSP
NSM	Chonburi		Thailand	1.2	1997	CSP
ASM			Malaysia	2	1998	CSP
Zhujiang Steel			China	0.8	1998	CSP
Baotou Steel			China	2	2000	CSP
Handan Iron			China	1.2	2000	CSP
Mega Steel Sdn Bhd.			Malaysia	2	1998	CSP
Posco	Kwangyang		Korea	1.8	1996	CSP
Siam Strip Mill			Thailand	1.5	1998	Sumitomo
EUROPE						
AST	Terni		Italy	...	1992	CSP
Aceria Compacta Biz	Bilbao		Spain	0.9	1996	CSP
Arvedi	Cremona		Italy	0.5	1992	ISP
Avesta-Sheffield	AB		Sweden	0.6	1988	CONROLL
AFRICA						
Saldanha Steel	Rivoria		S. Africa	1.4	1998	ISP

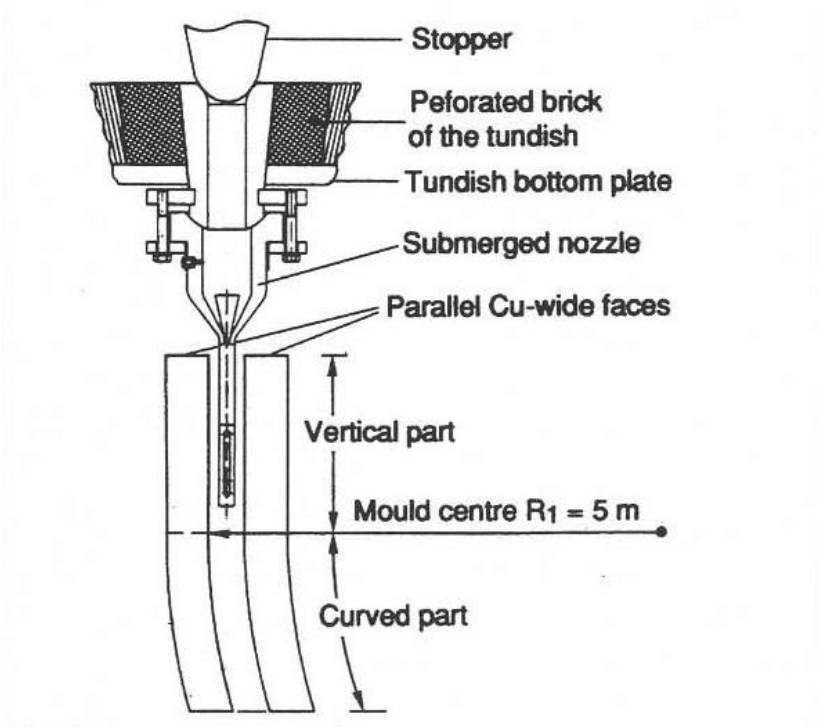

Figure 5 Mold and Submerged Entry Nozzle (SEN) developed for the ISP process

2.2.3.3 CONROLL Process

Slabs 70 mm to 80 mm thick are cast through a straight mold with parallel walls, followed by in-line bending to a radius of 3 m and straightening[32].

The CONROLL process was tested at Avesta Sheffield in Sweden to produce stainless steels at a rate of 2 to 4 m/minute and then tested for producing carbon steel grades[33]. Its maximum casting speed of 3.7 m/minute was run on a trial basis at Voest-Alpine Stahl Linz to make 80 x 1285 mm or 1030 mm carbon steel slabs.

2.2.3.4 The DANIELI Thin Slab Conticaster

This caster produces plate at the Saboliare plant in Italy[34]. It has a normal radius of 5.5 m and a lens-shaped curved mold equipped with 180 thermocouples. Slabs of 30-140 mm x 900 to 2200 mm can be cast at various speeds ranging from 0.5 to 6 m/ minute. The stroke length of the mold oscillation cycle is 3.5 mm with a frequency of 3 to 5 Hz depending on the slab size, casting speed and mold powder type. It has an equalizing/induction furnace where the slabs go after the casting machine, and a four high rolling stand preceded by a descaler.

2.2.3.5 Belt Casters

The movement of cooling belts to reduce friction between the slabs and mold requires the special maintenance of the belts such as their special cooling and coating to reduce belt distortion, and at the same time, slab surface defects.

The Kawasaki-Hitachi caster is of the vertical type, twin belt with a “V-bell” mouth shape for easy liquid metal feeding through a SEN. Thin slabs from 30 mm x 800 mm to 1000 mm are cast at speeds of 10 – 12.5 m/minute through a 3,700 mm long mold entering directly the rolling mill without any reheating in between.

2.3 CONVENTIONAL CONTINUOUS CASTING (CCC) VS. THIN SLAB CASTING (TSC)

Several important changes were made from the CCC process to the TSC process to make it more attractive for the steel industry relating to the metallurgical aspects, economy, and environmental issues. These include the almost absolute substitution of the blast furnace (BF) and basic oxygen furnaces (BOF) used in CCC by the electric arc furnace (EAF) for the steelmaking practice mostly from recycled scrap and DRI leaving the coke ovens and sinter plants far behind.

One of the most outstanding advantages of the TSC technology was the reduction in thickness from 200 – 250 mm (10 in) slabs produced by the CCC to the 50 mm (2 in) slabs produced by the TSC. But one disadvantage is the difficult feeding of molten metal into the narrow molds which is of great importance in the CSP and ISP processes. K. Wunnenberg[18] studied the phenomena related to the applications of narrow molds and to thickness reduction of a strand with a liquid (mushy) core. His conclusions were that the heat transfer in a funnel-shaped mold, designed to reduce fluctuation in the metal level by diminishing turbulence, is rather non-stationary and non-uniform, showing a strong variation in physical contact between the strand and the mold, but in molds with parallel, broad walls with a narrow space between them, the heat transfer was similar to that of the CCC. It is known that a higher casting speed increases the mold temperature, thus, it is reasonable to expect higher heat fluxes to the mold of thin slab casters since the casting speeds are much higher. Other studies

were made regarding the heat flux differences between CCC molds and a twin belt caster mold[27, 35].

The thickness reduction of a strand with a liquid core is observed by the outward bulging of the narrow sides. Longitudinal strains in the broad sides are small. Compared to CCC, where the reduction is too large, strains are negligible. Segregation may be present in some steel grades produced by both CCC and TSC as a result of the in-line reduction when the casting speed is low, the reduction segment is too long and the reduction is too large.

It was expected that the as-cast microstructure in steels produced by TSC would be finer than that of CCC, leading to a more homogeneous distribution of microsegregation as a result of the faster cooling rates after solidification. Experience has shown that the austenite grain size remains large, from 800 ?m to 1000 ?m on average, compared to the 200 - 300 ?m in conventional cold charge, Figure 6. The austenite grain size of TSC is much larger than that of CCC (cold charging) after the reheating of the slab from room temperature, Figure 7, since it does not go through any *?* to *a* transformation during cooling and is then reheated from *a* to *?* to provide grain refinement as it occurs in conventional slab-reheating. The homogenization of the original dendritic/solidification structure and the austenite grain refinement has to be taken care of during the equilibrating furnace and the rolling process.

Other studies on TSC but with different compositions, for instance, the simulations of a V-Nb and a V-Nb-Ti TSC microalloyed steels show the D? = ~1000 ?m [29]; and a vanadium microalloyed steel, reported a D? of ~ 1000 ?m [36].

C M Sellars et al.[23] reported that the austenite grain size (D?) in a thin slab is 550 - 600 ?m as compared to a thick slab where it is 1000 ?m. The unavailability of the transformations that take place during the cooling and reheating cycle and the roughing mill before the finishing stands, are a signal of a coarse-grained as-cast structure. They also showed other austenite grain sizes ranging from 540 ?m in the center of the slab up to an average length in the columnar (longitudinal) zone of 2820 ?m. These data come from a simulation test based on replacing the steel by a similar material with a characteristically stable austenite structure over the range of temperatures from freezing to room temperature. In addition to this, the secondary dendrite arm spacing (SDAS) reported from this material is ~ 24 – 32 ?m. The values reported here are nowhere close to the typical values of a commercial HSLA steel produced by the CSP process, where the D? ranges from 600 to 1000 ?m, and a SDAS that goes from 50 to 150 ?m, as mentioned above and in agreement with other publications elsewhere [37, 56].

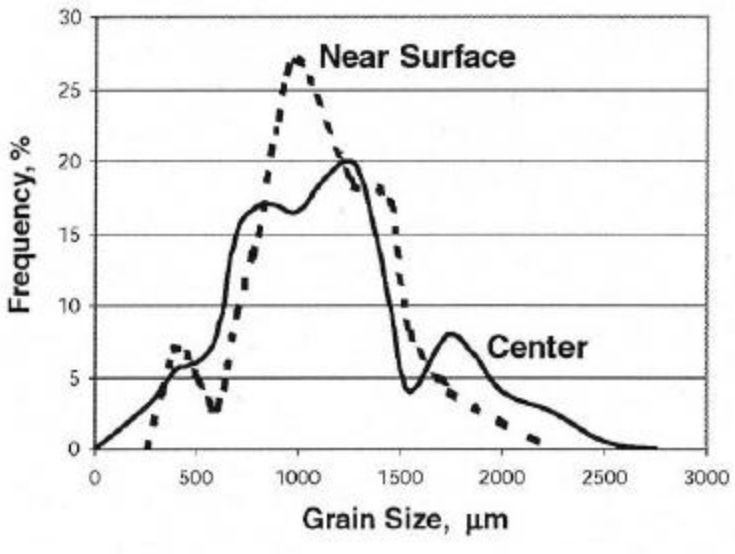

Figure 6 As-cast austenite grain size distribution in an industrial thin slab sample[38]

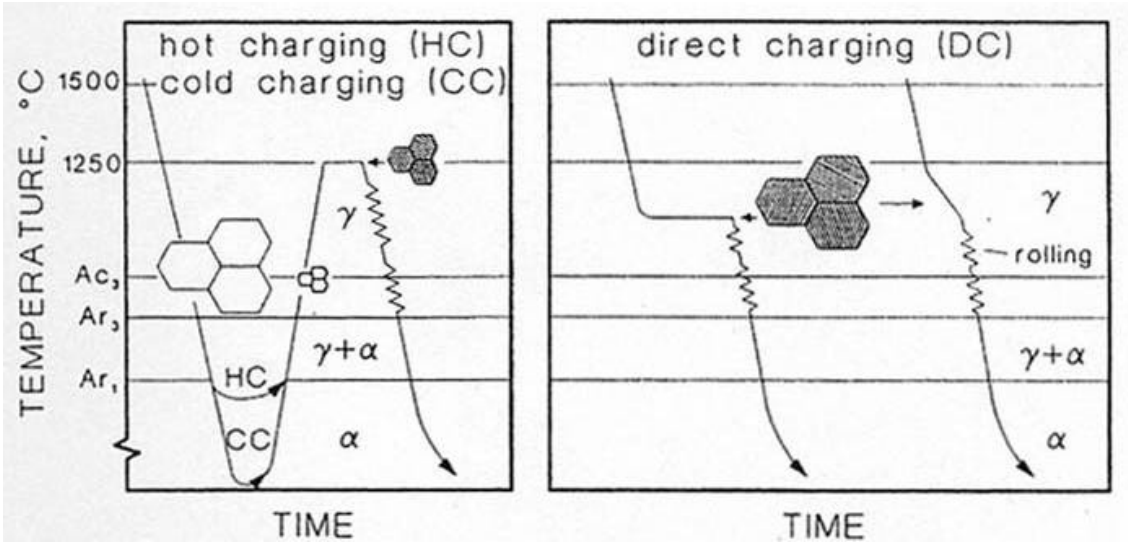

Figure 7 Temperature evolution during Hot Charging (HC) and Direct Charging (DC) in comparison with conventional Cold Charging (CC)[39]

2.4 AS-CAST/SOLIDIFICATION STRUCTURE

In most casting and ingot making processes, heat flow is not at steady state. During the process of pouring liquid metal into a mold, at different locations of the mold, for example, the metal-mold wall interface, the specific heat and the heat of fusion of the solidifying metal go through a series of thermal resistances. As the solidification rate depends on the thermal properties of the mold, some casting processes employ insulating molds. For example, sand casting and investment casting[40, 41, 42, 43].

The formation of a crystal from a liquid is a homogeneous nucleation and growth process, Figure 8. Both nucleation (N) and growth (G) rates involve atom motion which is proportional to exp(-Q/RT), where Q is the activation energy for the atom to move, R is the ideal gas constant and T is the absolute temperature. Both N and G are central for controlling the rate of crystallization[44] . For small undercooling, the thermodynamic driving force is small; hence, the rate of crystallization is low. As the temperature decreases, this driving force increases by becoming more negative, hence, the rates of nucleation and of growth increases. Eventually this is overcome by the atom mobility. The rates of nucleation and growth are a maximum at an intermediate temperature, as will the rate of crystallization, Figure 9. If the cooling conditions fell below the maximum of the crystallization curve, a metastable liquid would be obtained.

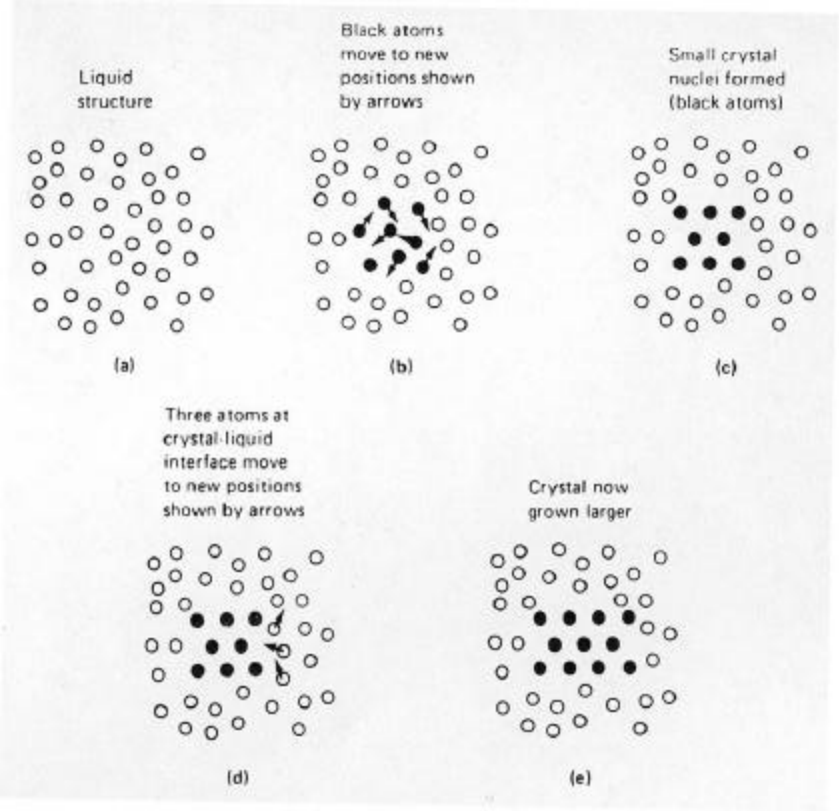

Figure 8 Schematic illustration depicting the homogeneous nucleation of a crystal and its growth in a liquid[44]

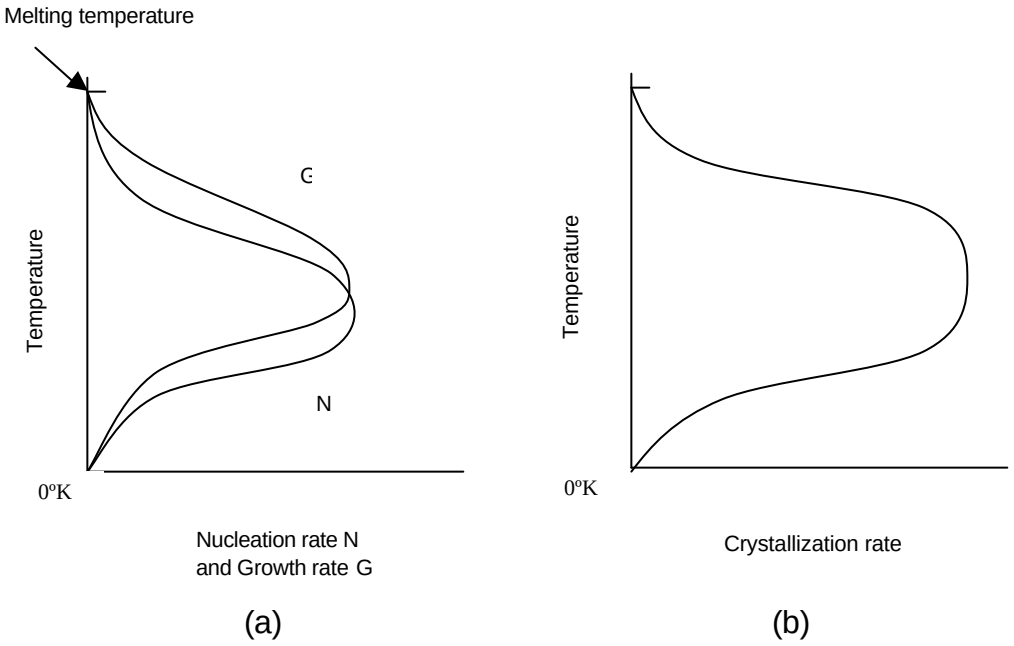

Figure 9 Schematic illustration of the temperature dependence of (a) the nucleation rate, N, and the growth rate, G, during solidification, (b) crystallization rate, which depends on both N and G.[44]

In commercial alloy casting in molds, where heterogeneous nucleation occurs, the rise of the nucleation rate with temperature below the freezing temperature increases at such a rate that even rapid cooling is not sufficient to prevent nucleation.

2.4.1 As-Cast Grain Morphology and Size

Atoms attach onto the crystal surface at different rates depending on the crystallographic directions. In many cases, the crystal will develop a certain geometric shape; for example, a dendrite where the crystal develops side arms or branches Figure 10[41, 42, 43, 45]. As the nucleation rate, (N), increases and the growth rate, (G), decreases, a small grain size is obtained upon cooling. It is desired to have a high nucleation to get a smaller grain size If the conditions are contrary, then few nuclei form before complete crystallization is achieved. Hence a large grain size is obtained. The ratio of the N and G controls the final grain size. If the temperature gradient is high, a crystal growing from a cold mold wall tends to form an elongated shape called columnar grains. If what is desired is a nicely formed equiaxed and fine-grained structure, the liquid can be inoculated with fine crystalline particles of high melting point materials to act as heterogeneous crystallization nuclei in the material upon casting.

(a)

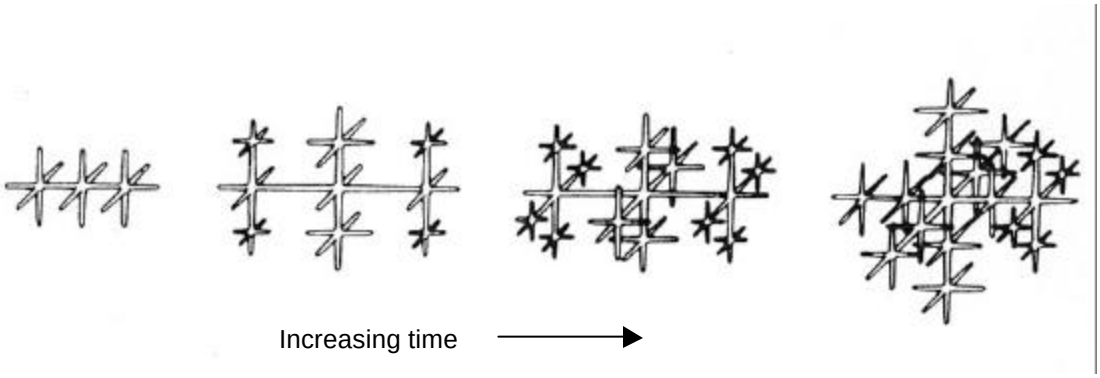

(b)

Figure 10 (a) Photograph of a large, 9 in. long dendrite formed in a steel [46] and (b) schematic illustration of a dendritic crystal[47].

2.4.2 Macrosegregation

Many of the solidification phenomena, structural features and macrosegregation patterns in continuous casting of steel are similar to ingot casting if one measures time with respect to a reference frame that moves with the strand. Axial segregation and V

segregates may be seen in longitudinal sections of continuously cast steel, whose typical segregation occurs in the centerline of a slab.

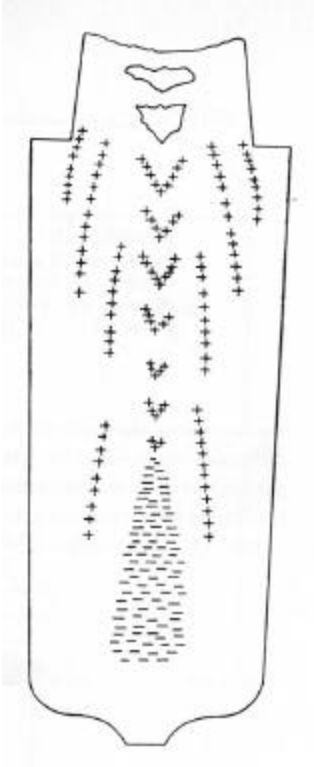

Figure 11 Macrosegregation in a killed steel ingot. + denotes regions of positive segregation; - denotes regions of negative segregation[40]

Macrosegregation refers to variations in concentration that take place in alloy castings or ingots and range in scale from several millimeters to centimeters. The scale of chemical inhomogeneity is much greater than the dendrite arm spacing compared to microsegregation, where the scale is smaller, usually the size of the dendrite arm spacing. Such variations can have a detrimental impact on the subsequent processing behavior and properties can lead to rejection of cast components or processed products.

The amount of solute and location of macrosegregation in ingot casting depend on the material's phase diagram and the solidification process applied. Figure 11 shows a schematic diagram of the macrosegregation in a steel ingot. During the solidification of alloys, there is macrosegregation of solutes leading to concentration gradients from the surface of the cast material to the center. Figure 12 shows this phenomenon for a binary alloy containing X0 solute content, where the first solidified material will have a composition X1. As the material solidifies through the thickness, the composition increases until the solute content varies across the crystal and into the liquid.

When two growing crystals from opposite walls approach one another at the centerline of the ingot, the final liquid between these two crystals is rich in solute. This is true for conventional continuous casting (CCC), where the sections to be solidified are relatively thick (250mm). In CCC, it has been observed that the segregation at the core of the solidifying material is higher than that at the surface or sides.

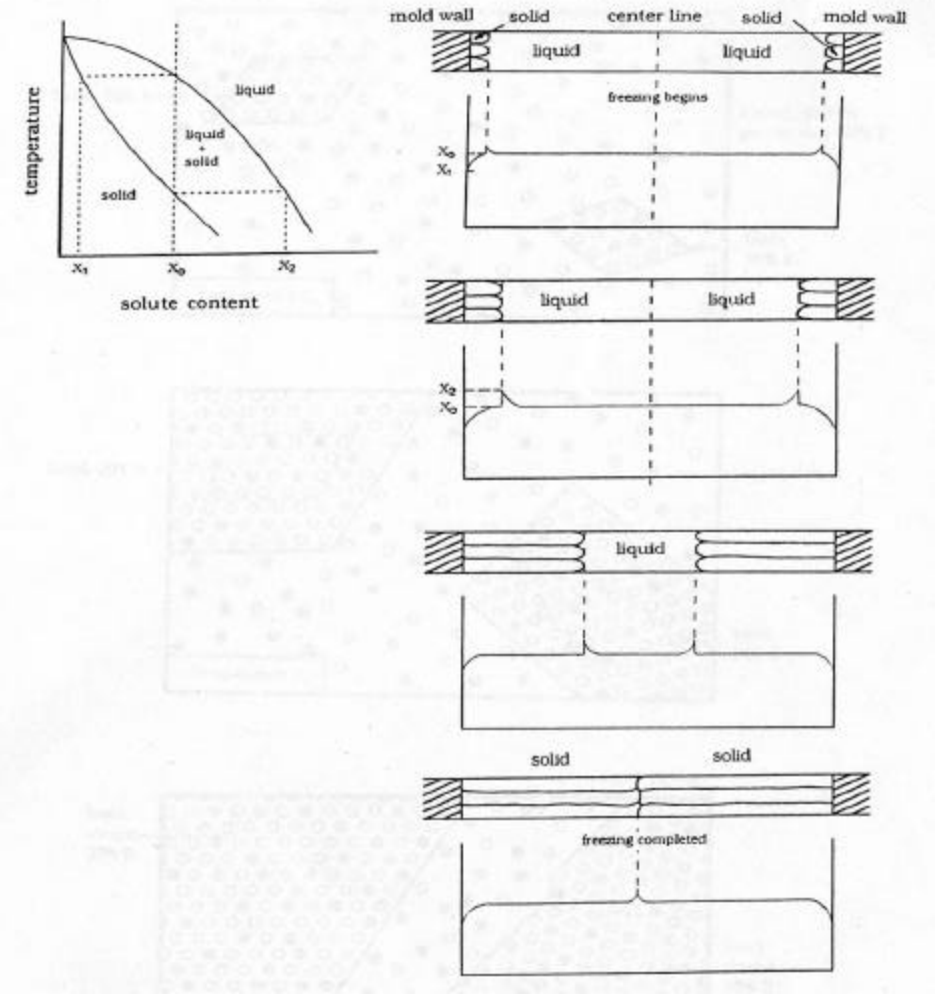

Figure 12 Schematic illustration of the origin of gross ingot segregation[48]

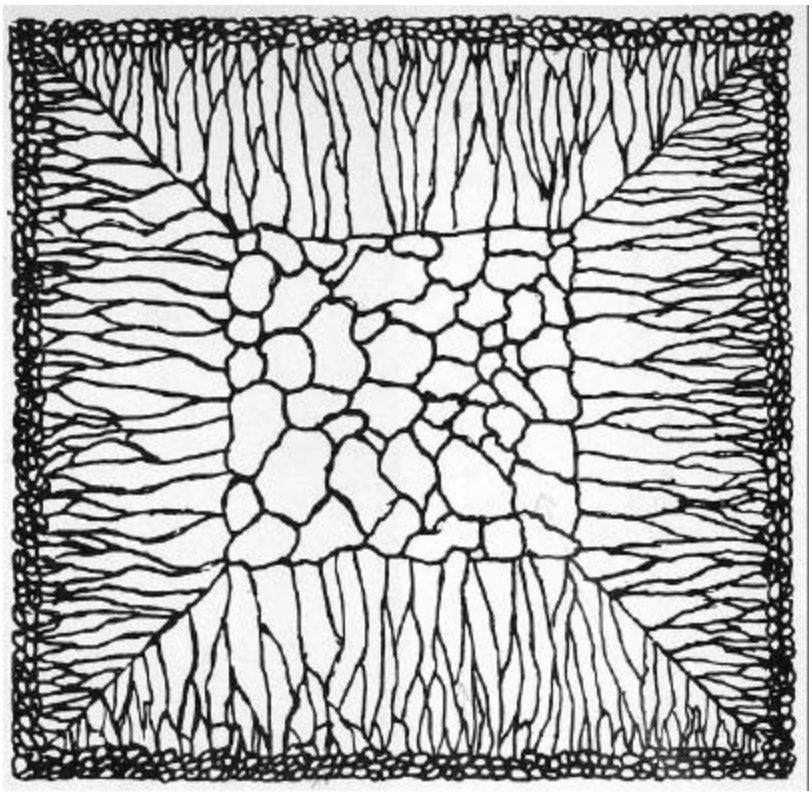

Figure 13 Sketch of typical grain morphology in cast steel showing characteristic macrostructure: outer chill zone, columnar zone and an equiaxed zone at the center of the ingot[49]

2.4.3 Dendritic Segregation

The process of dendritic segregation is known as “coring”. During the equilibrium solidification process of a pure material, the melt freezes to a single crystalline phase which will have the same composition as the parent liquid phase. However, when referring to alloys, solidification takes place over a range of temperatures. The composition of the first solidified crystals is different from that of the parent liquid phase composition, although it will be the same after further cooling until the freezing is complete. In equilibrium cooling, the cooling rate has to be sufficiently low and the

motion of atoms fast enough for the composition to be that of the parent liquid everywhere in the solid.

Coring or dendritic segregation appears due to fast cooling rates where atom diffusion is not fast enough to reach equilibrium, giving rise to a concentration gradient between crystals, hence, the formation of the cored structure is not an equilibrium process. Figure 14 shows a schematic illustration of the formation of a dendrite. The material was cut along the main dendritic axis. In order to clearly see the segregation between the dendrite arms, the microstructure has to be properly etched[50 51].

The etchant has to be such that it brings up both the solute rich-regions (dendrite pools or zones of depression) and the solute-poor regions (zones of elevation) with a different texture or relief.

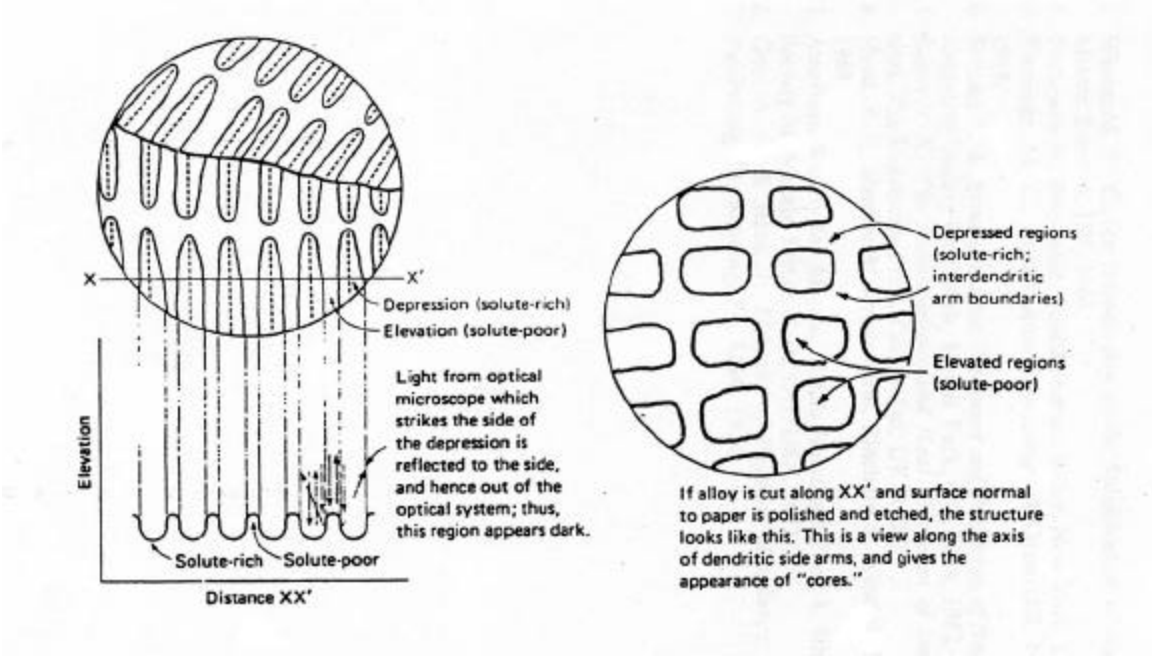

Figure 14 (a) Schematic illustration of the surface topography developed upon etching in which dendritic segregation exists. Solute rich and poor regions are seen. (b) The appearance if the plane of cut is such that the ends of a dendrite arms are viewed[44]

Figure 13 shows a typical as-cast grain structure, a chill zone at the metal-mold interface, a columnar-grain structure and an equiaxed zone in the center. These three zones can be seen in castings and ingots of real materials, especially in plain carbon or low-alloy steel. In stainless steels, the equiaxed zone does not appear, it is all columnar with a little chill zone.

In steels, nuclei form on the walls of molds and start growing dendrites normal to the heat flow direction in the walls. The dendrite is dependent on the degree of undercooling as is the dendrite arm spacing, which is smaller closer to the chill zone where the dendrite crystals nucleated. Hence as the dendrites grow, their spacing will

change depending on the undercooling - Figure 15. The center of the dendrite arms form first during freezing. These regions will be relatively low in carbon and alloying elements. The interdendritic regions will be the last regions to freeze and hence, will be solute-rich regions. In low carbon steels, the center of the dendrite may be all ferrite and the interdendritic regions are almost all pearlite. The firstly formed dendrites are delta-ferrite, which then transform to austenite and still later to ferrite and pearlite.

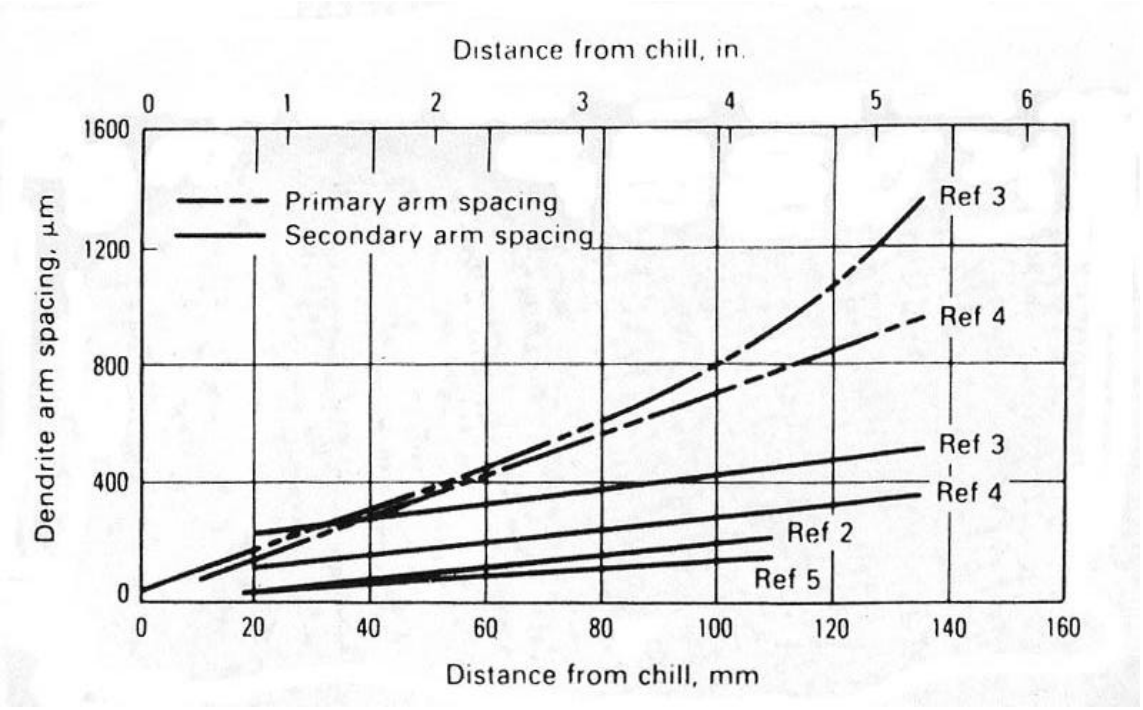

Figure 15 Data showing the increase in dendrite arm spacing as the distance from the cold mold wall increases[52]

A measure of the effects of solidification conditions in dendrite structures is the Dendrite Arm Spacing (DAS) i.e., the spacing between primary, secondary or higher order branches. Generally, the spacing measured represents the perpendicular distances between branches. The primary dendrite arm spacing is expected to depend

on the product of temperature gradient and growth rate GR, by analogy with the cellular solidification spacing[53]. Figure 16(a) shows one example of a ferrous alloy and 16(b) for commercial steels with different carbon contents.

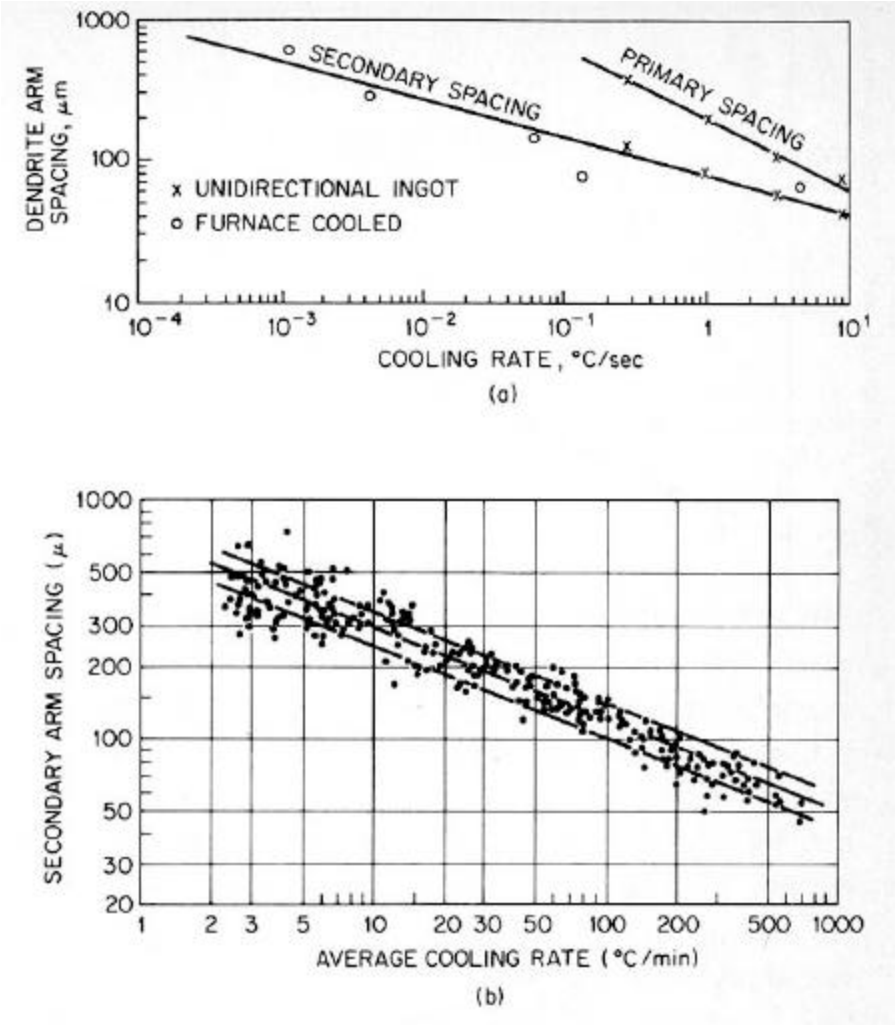

Figure 16 Experimental data on dendrite arm spacings in ferrous alloys. (a) Fe-25%Ni alloy; (b) commercial steels containing from 0.1 to 0.9% C[49]

Secondary dendrite arm spacings (SDAS) also depend directly on cooling rate for a wide variety of alloys[54, 53]. The SDAS reported in the literature[55] for conventionally

cast plain carbon steels of 230 mm in thickness goes from 90 ?m at the edge to about 300 ?m at the center of the slab. Some studies related to SDAS measurements carried out in Buschutten, involving a laboratory/ pilot plant simulation of TSC material with a thickness of 50 mm, reveals a SDAS of 45 ?m at the surface and 95 ?m at the center. Engl et al.[56], based on a simulation of TSC, found an average SDAS of 50 ?m to 160?m from surface to center, respectively. Other TSC SDAS were reported by Sellars et al.[57]. His results are not only based on a simulation of the TSC process but also on the variation of the original chemical composition of the steel. The SDAS ranges from 24 ?m to 32 ?m.

In general, the measurements of SDAS in TSC-HSLA steels reported in the literature range from 40 ?m at the edge to 250 ?m at the center of the slab[55, 56, 57], depending on the steel compositions and simulation conditions. These appear to be different from those of commercially produced steels. The reduction in SDAS is attributed to the higher cooling rates near the meniscus of the thin slab caster mold. Also, the additions of microalloying elements such as Nb and Ti in the steel seem to have an effect on SDA spacing. For instance, N. Pottore [51] studied the effect of Nb on reducing the width and size of SDAS during unidirectional solidification and its effect on the austenite grain size. He found that there is a direct correlation between the solidification boundary and the austenite grain boundary in low carbon Nb-bearing steels.

2.4.4 Homogenization

The application of heat treatments is of essential importance to chemical homogenization of as-cast steel in order to get rid of the chemical segregation associated with the cast material and for redistributing the solute by putting it back in solution for grain size control and solid solution strengthening during subsequent processing. The heat treatment is usually applied in the austenite region. The primary concern in heating up to an austenite region is to maintain a constant austenite grain size without coarsening with the purpose of achieving a uniform structure[58] prior to hot deformation, for instance, hot rolling, hot forging, etc.

To remove the chemical segregation or cored structure caused by the rapid cooling rate, and due to the composition gradients along the crystal structure, the solute atoms would have to diffuse to equilibrate or homogenize the structure, where very high temperatures are required.

2.5 MICROALLOYED STEELS

Typical microalloyed steels are known as ferrite-pearlite low carbon-manganese steels. They usually contain low amounts of carbon (0.1% or less) and small amounts of carbide or nitride forming elements such as Nb, Ti or V. The combination of the alloying elements with controlled rolling and coiling practices leads to the production of alloys with fine grains and subgrains as a result of the formation of fine strain induced

precipitates in the form of carbides or nitrides, which form on the grain or subgrain boundaries[59, 60, 61]. The addition of each one of these contributions mixed with the fine grained-microstructure lead to a great increase in strength and ductility in steels. Coarse precipitates, low volume fraction and large interparticle spacings may be detrimental to the properties of the material.

2.5.1 High Strength Steels

The automobile market has forced the steel industry to change from low to higher strength steels produced by cold rolling, being an effective way of strengthening when the limit of formability is low enough for these steels to be accepted. Other high strength steels were cold-rolled and annealed, produced initially as microalloyed hot rolled steels with a modified chemistry to meet specific strength requirements after annealing. The yield strength (YS) of these steels (up to 400 N/m^2) were strengthened mainly by grain refinement and were more formable than the steels with a higher degree of temper rolling, but with lower ***r*** values. The next step would be minimizing the loss of formability with increasing strength. As a consequence, substitutional solid solution strengthened steels were developed, mainly because the loss of elongation per unit strength increase is less for a solid solution strengthened steel than for a microalloyed steel, Figure 17. These relationships are similar to those for ***n*** (work hardening) value, Figure 19.

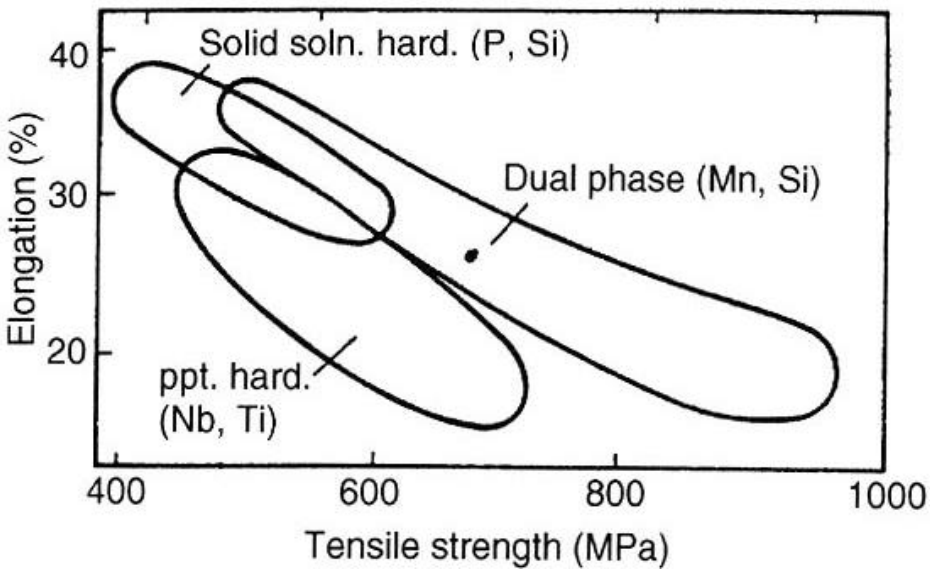

Figure 17 Variation of tensile elongation with tensile strength for various types of steel [1]

The equivalent relationships between ***r*** value and strength are given in Figure 18.

The strength increase that could be obtained with a rephosphorized addition was limited by the detrimental effect of phosphorus on welding. These steels were highly formable but restricted to moderate strength increases with minimum yield stresses of up to 300 N/m^2.

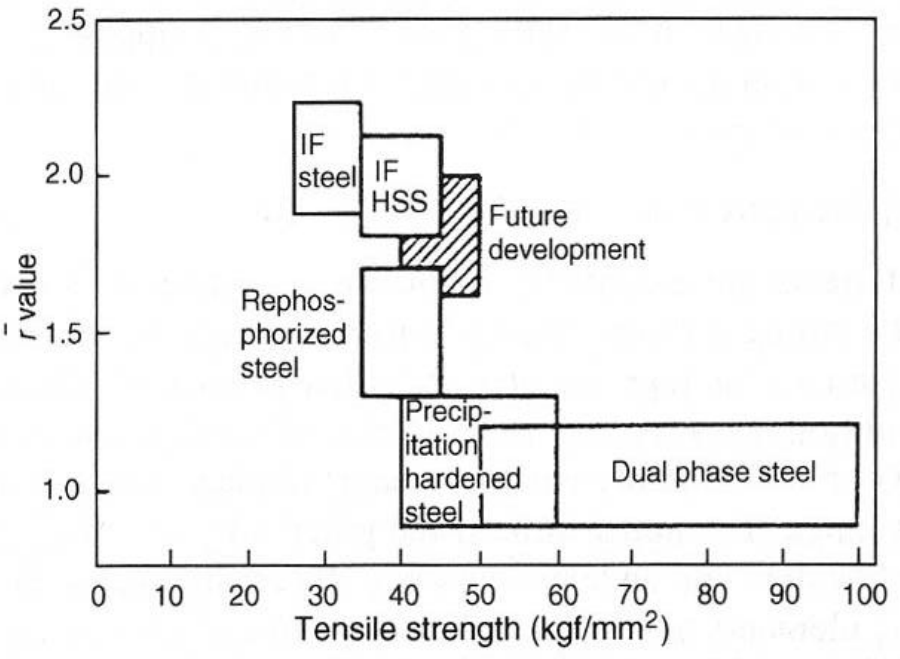

Figure 18 Relationship between r value and tensile strength[1]

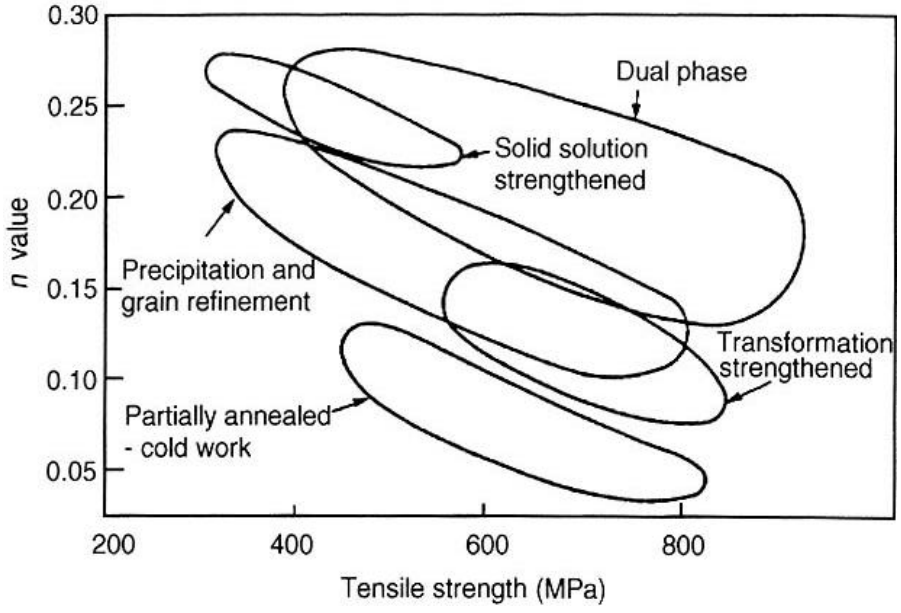

Figure 19 Relationship between n value and tensile strength[62]

2.5.2 Dual Phase Steels (DP)

Dual phase steels are low carbon HSLA steels (0.05 – 0.02% wt) that contain Mn, Si, and microalloying additions. They have tensile strengths of up to 600 N/m^2 and show high ***n*** values but low ***r*** values as a result of their dispersed martensite islands in a soft ferrite matrix. This occurs because of the severe cooling and intercritical annealing, but they often still contain small amounts of retained austenite[63]. The intercritical anneal can follow either finish rolling for hot strip product or cold rolling for cold rolled and annealed (CR&A) or hot dip galvanized (HDG) product.

2.5.3 Bake Hardenable Steels

Carbon in solution in these steels increases their yield strength up to 300 N/m^2 during the baking treatment after painting and have the formability of a low-strength, solid solution strengthened steel, but the performance of a much higher strength steel. They are often ULC (ultra-low carbon) grades, resistant to aging at room temperature but not at slightly elevated temperatures, especially after deformation.

2.5.4 Interstitial Free Steels (IF)

Interstitial free steels require additions of Nb, Ti, and V as carbide forming elements in order to stabilize the interstitial elements. Vacuum degassing is used to reduce the interstitial levels to ~20 ppm. IF steels are affected by secondary cold work embrittlement. Phosphorus is added to give the material higher levels of strength, and to reduce the harmful effects of phosphorus, boron additions are required[64]. The typical tensile strength of IF steels is 440 N/m^2, which is considered low-moderate, but still with excellent formability[59].

2.5.5 Transformation Induced Plasticity Steels (TRIP)

Transformation induced plasticity or TRIP assisted multiphase steels contain small volume fractions of retained austenite in a ferrite-bainite matrix. The retained austenite improves ductility by transforming or "tripping" to martensite under the action of a forming strain giving rise to great crash resistance, dent resistance and weight reduction. They reach strengths of up to 800 N/m^2. TRIP steels have a high ***n*** (work hardening) value, providing high elongation (stretch formability to the steel, and have the potential for other forming applications such as deep drawing, where high ***r*** values are required.

2.5.6 High Strength Low Alloy Steels (HSLA)

HSLA steels have been developed and produced for the last 50 years as a result of the economic use of MA elements, which are combined in different amounts to optimize the HSLA steels properties. HSLA steels have yield stress values from 300 to 600 N/m^2 [65]. The upper limit of such a potential yield stress range is usually lower for a CR&A product depending on the processing.

The MA elements, depending on the kinetics of formation of the carbides or nitrides as precipitates and their solubility in austenite and ferrite, will have different effects[58]. Cuddy et al.[66] reported that alloying elements such as Al, Nb, Ti, and V initially dissolved in austenite increase the recrystallization temperature, below which, the application of deformation will result in fully-pancaked austenite grains, whereas deformation above this temperature will show the presence of partially or fully recrystallized grains. DeArdo et al.[67] studied the effect of Nb supersaturation in austenite, as it applies to the precipitation potential of Nb (CN) on the suppression of austenite.

Figure 20 shows some of the effects that MA elements can have on austenitic grain growth during reheating. The left side of the hatched region of the curves represents the suppression of the primary grains. The hatched region is the temperature at which grain coarsening (Tgc) takes place. During this transition, there is a mixture of primary and secondary grains, and to the right side of the hatched region, recrystallization will be present. As we can see, NbC or TiN formed at high temperatures suppress the austenite grain growth. Nb has proven to be more effective

than vanadium due to its affinity for nitrogen, but TiN has a much higher effect on austenite grain size control.

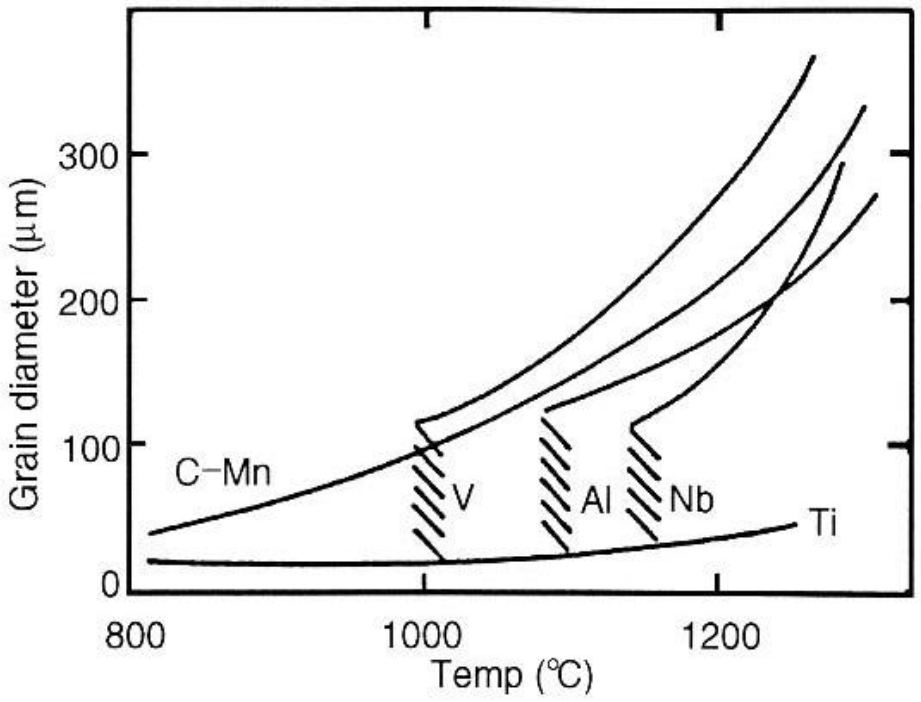

Figure 20 Austenite grain growth characteristics in steels containing various microalloy additions[68]

The addition of Ti to HSLA steels leads to the formation of relatively coarse complex carbo-nitrides which may be able to reduce austenite grain growth at high temperatures due to its solubility properties, but not the recrystallization[69]. Some of the solute held as precipitate is dissolved back into solid solution during the reheating process and may lead to further strain-induced precipitation on cooling during hot rolling, retarding austenite recrystallization. When the final rolling is at a sufficiently low temperature, T_{stop}, the recrystallization has been completely inhibited. The non-recrystallized austenite transforms to a very fine-grained ferrite. The final ferrite grain

size depends on the cooling rate after the steel leaves the last finishing stand. Figure 21 illustrates how the recrystallization stop temperature differs as we increase the amounts of MA elements. A significant variation can be seen from the great effect that Nb has compared to Ti, Al and V which have a smaller effect respectively.

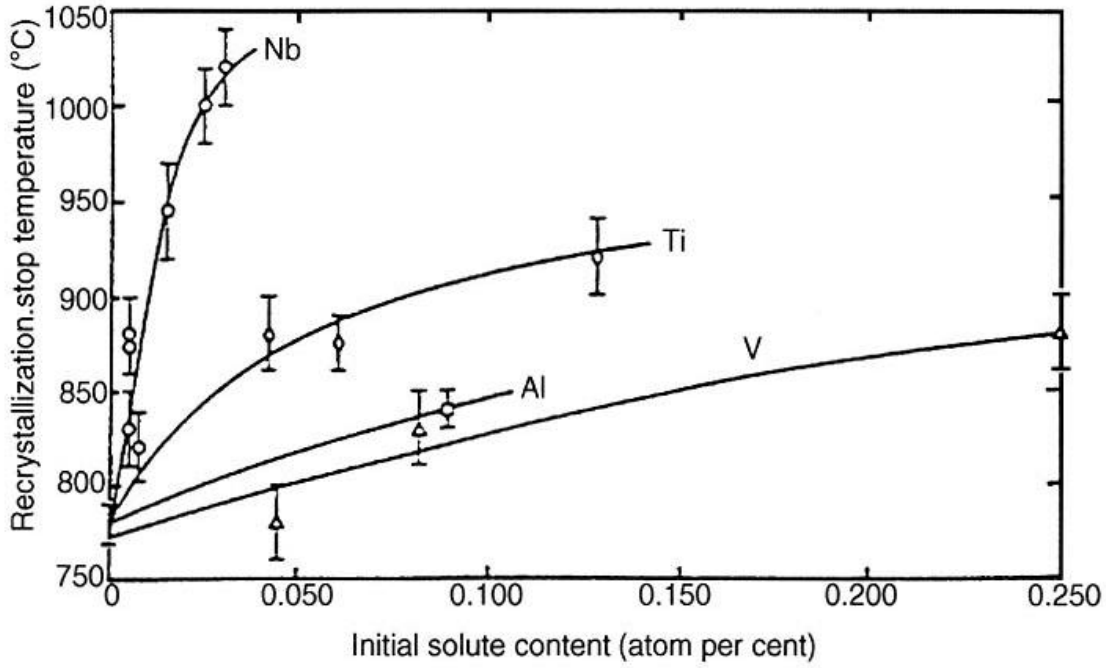

Figure 21 Effect of microalloy solute content on the recrystallization stop temperature (T_{stop}) in a 0.07C, 1.40 Mn and 0.25 Si steel[70]

During or after the ? to a transformation, fine precipitates contribute to higher strength levels. However, precipitates that formed in austenite do not contribute to the strengthening of the final hot rolled structure. CR&A may be used to give the steels improved properties by applying the proper cold reduction to the material and heat treating it either in continuous or batch annealing[71, 72].

HSLA steels have, in general, a beneficial combination of high yield strength and low temperature toughness mainly from the extremely fine-grained microstructure coming from the phase transformation, which underwent a high degree of deformation below T_{stop}.

2.5.6.1 Compact Strip Production for HSLA Hot Strip

In the last decade, The CSP technology has shown some diversification in the product mix. One example is the production of HSLA hot strip steels, which show high strength accompanied by excellent ductility even at low temperatures. It is considered a value-added product in spite of the strict specifications it has to meet to be produced by CSP. Some properties required from HSLA hot strip are high strength at static and dynamic loads, high resistance to brittle fracture, especially at low temperatures, and good weldability[73]. Several process specific characteristics have to be observed for CSP plants which require further consideration of the following topics: a) influence of microalloying in the microstructural evolution, b) utilization of the hot deformation to condition the austenite and c) peculiarities of the ? to a transformation reactions[74, 75].

The conventional HSLA hot strip production is based on conventional processing that solidifies as d-ferrite and undergoes the following phase transformations in the path of cooling and subsequent reheating (prior to hot rolling):

Liquid –> d-Ferrite –> Austenite-?1 –> a-Ferrite –> Austenite-?2

In the CSP process, only the following phase transformations take place:

Liquid –> d-Ferrite –> Austenite-?1

This is due to the direct entry of the cast slab to the tunnel furnace, which is preheated at 1150 ºC. Zajac et al. [76] and Bleck et al. [77] determined that the CSP product from direct charging shows a higher efficiency regarding the solubility of carbonitrides in the austenite compared to conventional cold or hot charging.

2.6 PRECIPITATION IN STEELS

Microalloying elements (MAE) such as Nb, Ti and V play a very important role in the processing of steel. The combination of these MAE with interstitial elements such as C and N leads to the formation of carbides or nitrides; for instance, (VC), (VN), (NbC), (TiN), etc., or even complex carbonitrides like (Nb, Ti)(CN). These precipitates have a strong influence on the control of the microstructure and the final properties of the steel in different ways - Figure 22[78]. Depending on the temperature and processing stage at which they form during the process, or more specifically, the recrystallization temperature of austenite, the temperature at which the transformation occurs in addition to other features like their size, volume fraction, and inter-particle spacing, these precipitates will have a different effect on the properties of the material.

The strengthening of steel derived from microalloy additions may be produced by the dispersion of fine precipitated particles or by grain refinement, i.e. inhibition of grain growth by second phase particles or by a combination of both.

To obtain a fine ferrite grain size in the final product, the control of the austenite grain size is required prior to the transformation, although the final grain size may be greatly influenced by the control of grain growth during the ? to a transformation. Austenite grain size is controlled by particles with high dissolution temperatures or stable at high temperatures such as TiN and NbC.

To produce dispersion strengthening, fine particles (3-5 nm in diameter) should be present either as interphase precipitates or precipitated after the transformation, which is even more effective.

The understanding of the factors controlling the dissolution of the precipitates in the form of carbides, nitrides or carbo-nitrides, is fundamental to know the effect they will have.

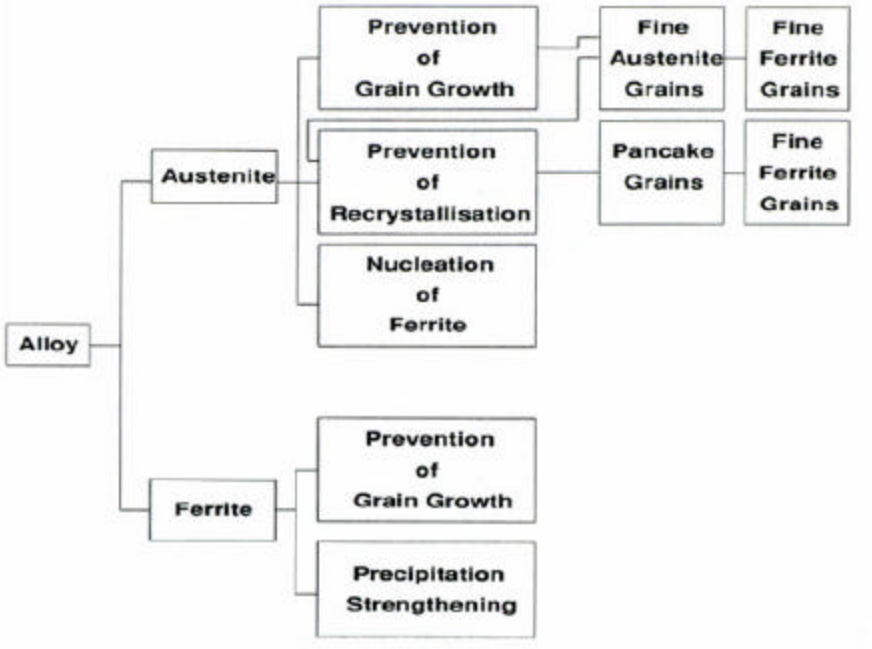

Figure 22 Effect of microalloy precipitates on the microstructure of steel[78]

2.6.1 Solubility Product

Considering the reaction between a microalloying element, M, with an interstitial, X, both being dissolved in austenite and forming a compound, MX, at a certain temperature T

$$[M] + [X] ? \quad (MX)\ldots\ldots\ldots\ldots\ldots\ldots (1)$$

Where [M] [X] are the concentrations of M and X dissolved in austenite respectively, and (MX) is the constituent. The equilibrium constant, referred to as the solubility product, is obtained in terms of the activities:

$$Ks = a[M] * a[X] / a(MX)\ldots\ldots\ldots\ldots\ldots\ldots\ldots (2)$$

It can also be expressed in terms of the elemental concentrations and activity coefficients (?) through

$$a_{[M]} = ?_{[M]} [M] \ldots\ldots\ldots\ldots\ldots\ldots\ldots\ldots(3)$$

This gives

$$Ks = ?[M] [M] * ?[X] [X] / a(MX)\ldots\ldots\ldots\ldots..(4)$$

assuming that the activity coefficients and the activity of the MX are equal to unity, provided that the activities are directly proportional to the weight percentages, as they usually are at the very low concentrations in microalloyed steels, Ks is of the form:

$$Ks = [M] [X]\ldots\ldots\ldots\ldots\ldots\ldots\ldots..(5)$$

The temperature dependence of the solubility product is expressed by an equation of the Arrhenius form:

$$\ln Ks = -(Q/RT) + c\ldots\ldots\ldots\ldots\ldots\ldots\ldots(6)$$

or

$$\text{Log10 } K_s = - (Q/2.303RT) + c/2.303\ldots\ldots(7)$$

Where Q is the heat of diffusion and R is the gas constant.

A more condensed way to express equation (7) is:

$$\text{Log } Ks = A – B/T\ldots\ldots\ldots\ldots\ldots\ldots\ (8)$$

where A and B are constants for a determined system, Log K_s is the logarithm to the base 10, K_s is defined by equation (5), [M] [X] are expressed in weight percentages (wt %) and T is the absolute temperature (K).

The dissolution of the precipitates formed in austenite (carbides, nitrides or carbo-nitrides) is determined by their solubility product[58, 79, 80, 81,] - Figure 23 shows the solubility products of the microalloy carbides and nitrides.

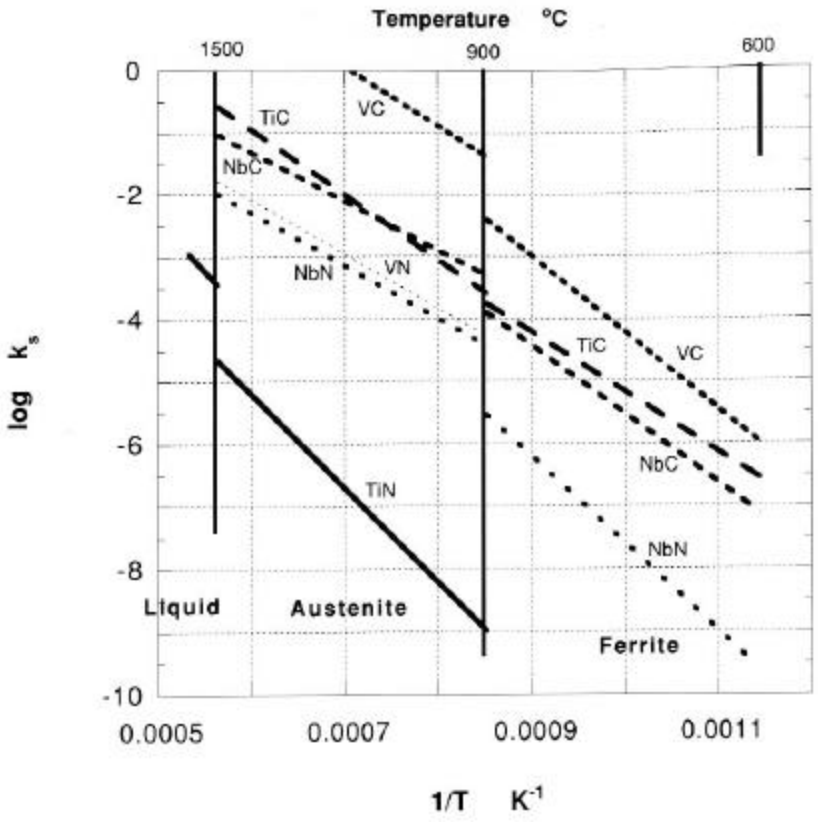

Figure 23 Comparison of the solubility products of the microalloy carbides and nitrides, showing the greater stabilities of the nitrides relative to those of the carbides[82]

Of particular attention is the very low solubility of TiN in austenite and the very high solubility of VC in austenite. The solubility for carbides and nitrides in ferrite are lower than in the austenite at low temperatures (ferrite region).

Table 2 Diffusion data for microalloy and interstitial solutes in austenite and ferrite. Also the diffusion coefficients at 1200ºC and 700ºC [83]

Element/Phase	D_0 ($m^2 s^{-1}$)	Q (kJ mol^{-1})	$D\alpha$ (700°C) ($m^2 s^{-1}$)	$D\gamma$ (1200°C) ($m^2 s^{-1}$)
C / α	0.62×10^{-6}	80.4	3.00×10^{-11}	–
C / γ	0.10×10^{-4}	135.7	–	1.59×10^{-10}
N / α	0.50×10^{-6}	77.0	3.66×10^{-11}	–
N / γ	0.91×10^{-4}	168.6	–	9.60×10^{-11}
Ti / α	3.15×10^{-4}	248.0	1.56×10^{-17}	–
Ti / γ	0.15×10^{-4}	251.2	–	1.86×10^{-14}
V / α	0.61×10^{-4}	267.1	2.80×10^{-19}	–
V / γ	0.25×10^{-4}	264.2	–	1.07×10^{-14}
Nb / α	–	–	–	–
Nb / γ	5.30×10^{-2}	344.6	–	1.56×10^{-17}
Al / α	0.30×10^{-2}	234.5	7.80×10^{-16}	–
Al / γ	–	–	–	–
Fe / α	1.67×10^{-4}	256.7	2.79×10^{-18}	–
Fe / γ	0.49×10^{-4}	284.1	–	4.13×10^{-15}

Table 3 Molar volumes of microalloy carbides and nitrides based on room temperature lattice parameters[84]

Compound (structure)	Molecular mass	Lattice parameter (nm)	Molecules per unit cell	Density (Mgm^{-3})	Molar volume (cm^3)
NbC (f.c.c.)	105	0.4462	4	7.84	13.39
NbN (f.c.c.)	107	0.4387	4	8.41	12.72
VC (f.c.c.)	63	0.4154	4	5.83	10.81
VN (f.c.c.)	65	0.4118	4	6.18	10.52
TiC (f.c.c.)	60	0.4313	4	4.89	12.27
TiN (f.c.c.)	62	0.4233	4	5.42	11.44
AlN (c.p.h.)	41	$c=0.4965$ $a=0.311$	6	3.27	12.54
γ-Fe (f.c.c.)	56	0.357	4	8.15	6.85
α-Fe (b.c.c.)	56	0.286	2	7.85	7.11

In addition to this, there are wide variations among the different carbides and nitrides that can be exploited. For example, in austenite, the most soluble carbide is VC, and, as a result, it can form a higher volume fraction of precipitates on cooling and result in more precipitate strengthening. NbC, however, is able to provide more effective boundary pinning because of its stability as a precipitate at more elevated temperatures than VC, where it would be in solution. However, TiN, which has the lowest solubility of all carbides and nitrides, is more likely to remain out of solution than NbC or TiC at high temperatures, hence, being a more effective agent (fine particles) in controlling grain growth at very high processing temperatures by pinning the austenite grain boundaries[85]. In general carbides dissolve at temperatures lower than the nitrides.

As the concentration of MA elements and C and N vary in HSLA steels, their degree of solubility varies, also. Carbides and nitrides have a high degree of mutual solubility, and, as a result, more than one metal (Nb, Ti, V) and both interstitials C and N can be present in the precipitates which form during processing[86, 87]. Complex mixtures of solute elements with carbo-nitrides have been found in HSLA steels[88, 89, 90].

The rate of particle dissolution under isothermal conditions, when the dissolution process is controlled by diffusion, has been calculated by means of numerical methods[91, 92].

Solubility helps to determine the rate of coarsening, which affects the force with which these precipitates can pin the grain boundaries and dislocations. Nitrides forming at higher temperatures are more resistant to coarsening from the equivalent carbides. Honeycombe et al.[93], found that the coarsening rate is considerably reduced by replacing carbon with nitrogen in the precipitates or in the composition. A similar trend occurred when the alloys were modified to replace some of the vanadium with titanium in the precipitates[94].

By having the appropriate solubility information, sufficient MA element, carbon and nitrogen, to give the correct stoicheometric ratio, the goal would be to get the highest solubility possible at the highest temperature involved in the controlled rolling process.

2.6.2 Precipitation in HSLA Steels

Minor additions of MAE (Nb, Ti, V) and an efficient processing schedule have resulted in tougher and stronger steels in view of the major effect of grain refinement on both mechanical properties, yield strength and toughness.

Precipitation of carbides or nitrides of Nb, Ti or V, in austenite (f.c.c) occurs as the temperature is decreased during controlled rolling of microalloyed steels. These stable precipitates possess the f.c.c. structure, also. Precipitation occurs in several ways: on grain boundaries, on dislocation networks and inside the grains or dispersed in the matrix, and the purpose of their formation is to control recovery and recrystallization and to inhibit austenite grain growth.

During the ? to a transformation, the presence of alloying elements can substantially influence the phase transformation kinetics and, hence, the morphology of the ferritic product.

3.0 STATEMENT OF OBJECTIVES

The objective of this work is to conduct a systematic microstructure characterization of two different microalloyed HSLA steels (B and E, low and high Nb and Ti contents respectively) commercially produced by the Compact Strip Production (CSP) process in a Thin Slab Casting (TSC) plant.

Conduct a complete characterization of precipitates formed during the as-cast and as-equilibrated processing stages of the steel.

An in-depth study of the kinetics of dissolution/formation of star-like precipitates is made in order to understand the behavior of the precipitates in the CSP process prior to and after the tunnel furnace.

The aim is to gain fundamental understanding of the microstructure evolution and precipitation behavior during the as-cast and as-equilibrated process stages, in order to increase the process efficiency in terms of microalloying content in the steel.

4.0 EXPERIMENTAL PROCEDURE

4.1 MATERIALS SELECTION

Several commercially produced low-carbon HSLA steels were provided by Nucor Berkeley, USA, and HyLSA, Mexico. The as-received materials were cut from slabs produced by the CSP process. Some of them were air-cooled and the others were water-quenched. The water-quenched steels were selected since these samples would provide information regarding segregation, precipitation and austenite grain size prior to and after the tunnel furnace.

Nb-bearing microalloyed steels were received as slab blocks (20 in x 6 in x 2 in). They were cut from the heads of the cast slabs prior to and after the tunnel furnace (TF). The complete description of the compositions and as-received conditions of the two steels used in this study are given in Table 4, which shows the conditions at which they were subjected prior to and after being received.

Table 4 Steel compositions and as-received conditions

STEEL	*C wt%*	*Mn wt%*	*Nb wt %*	*Ti wt%*	*N ppm*	*CONDITIONS*
B	0.059%	1.150%	0.035%	0.004%	100	**B**? BEFORE TF/WQ
BT						**BT**? AFTER TF/WQ
E	0.069%	1.234%	0.063%	0.039%	90	**E**? BEFORE TF/WQ
ET						**ET**? AFTER TF/WQ

4.2 METALLOGRAPHY AND SAMPLE PREPARATION

Samples were cut from 2 inch thick slabs parallel to the casting direction – Schematic diagram 2. They were ground and polished for metallographic analysis, etched with 2% Nital for different times to reveal their microstructures. All microstructural observations were made under bright field conditions on a Leitz-Epivert conventional optical microscope.

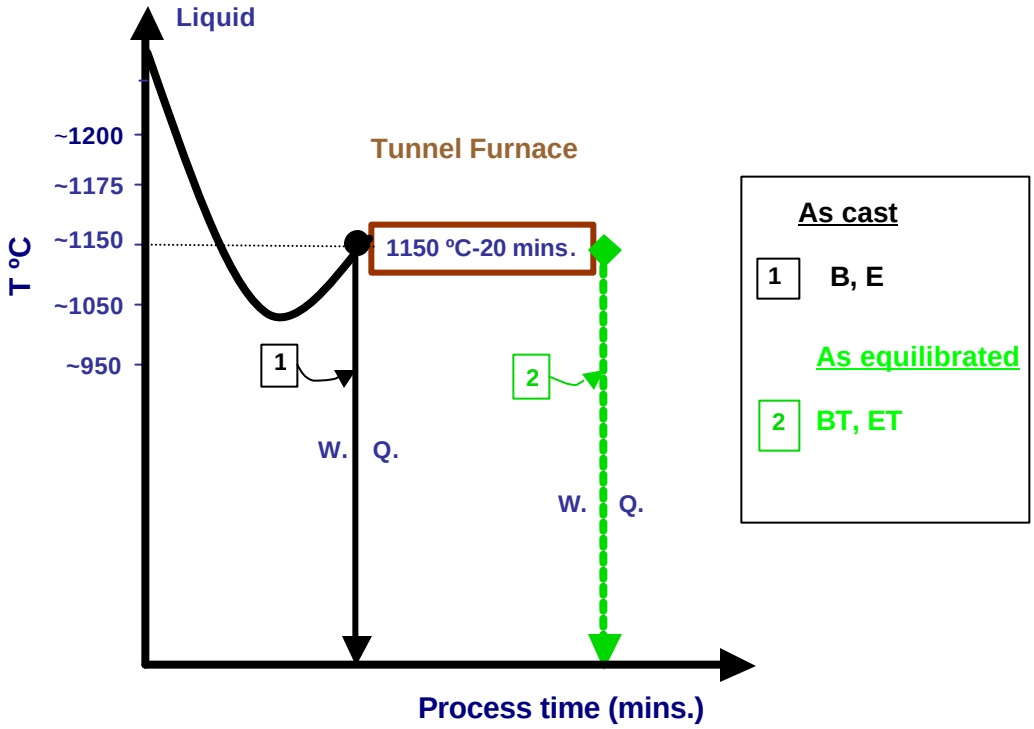

Schematic Diagram 1 Origin of the as-received material: As-cast condition: B and E, as-equilibrated condition, BT and ET.

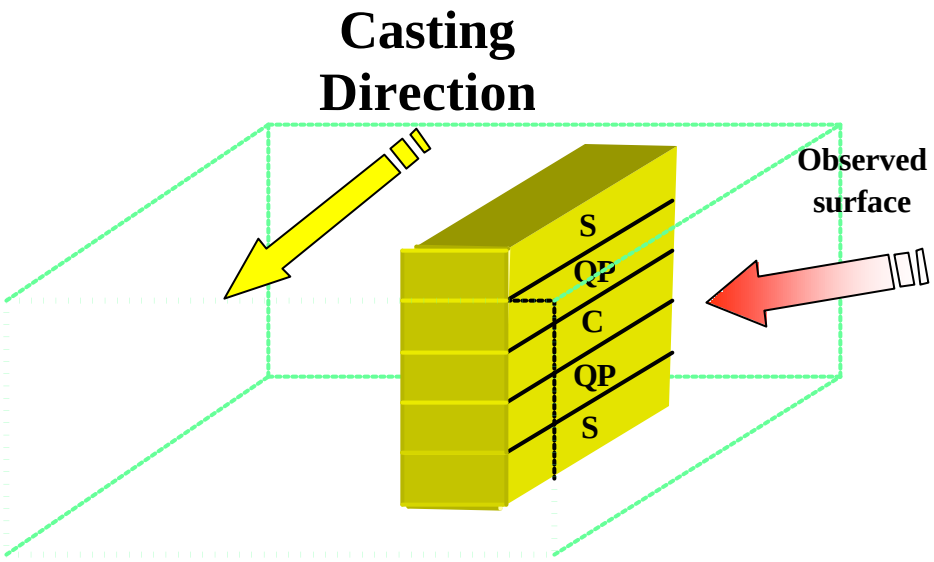

Schematic Diagram 2 Location through the thickness of the steel thin slab where the samples were cut from, and regions parallel to the casting direction that were analyzed through the thickness (S – surface, QP – quarter point and C - center).

4.2.1 Vickers Microhardness

Vickers Hardness Number (VHN-500 grams) measurements were made on all steels on locations through the slab thickness in a LECO (VHN) Vickers microhardness tester. An increase in hardness was observed at quarter points in both as-cast steels, B and E, where the microstructure consisted of large amounts of non-polygonal ferrite (especially at the quarter point), proeutectoid ferrite delineating the prior austenite grains and polygonal ferrite at the center region in lower amounts. This in turn, led us to do a chemical analysis at the different locations through the thickness in order to look for segregation. Slight segregation peaks were observed at quarter points but were not

outstanding enough as to be considered as the main reason of that hardness increase. - APPENDIX 1. Also, VHN microhardness was measured on the as-equilibrated steels conditions.

4.3 REHEATING EXPERIMENTS

This section includes the path followed for the reheating experiments performed on the as-cast steels B and E. These steels were heated from room temperature up to three different temperatures: BR and ER to1150 ºC; BR1 and ER1 to 1175 ºC and BR2 and ER2 to 1200 ºC. Steels were held at their respective temperature for 20 minutes to simulate the standard equalizing holding time applied to slabs directly in the industrial process. Also, the experimental conditions of an austenitized steel (EA), reheated to 1300 ºC, held at that temperature for 3 minutes and water quenched are included – Schematic diagram 3.

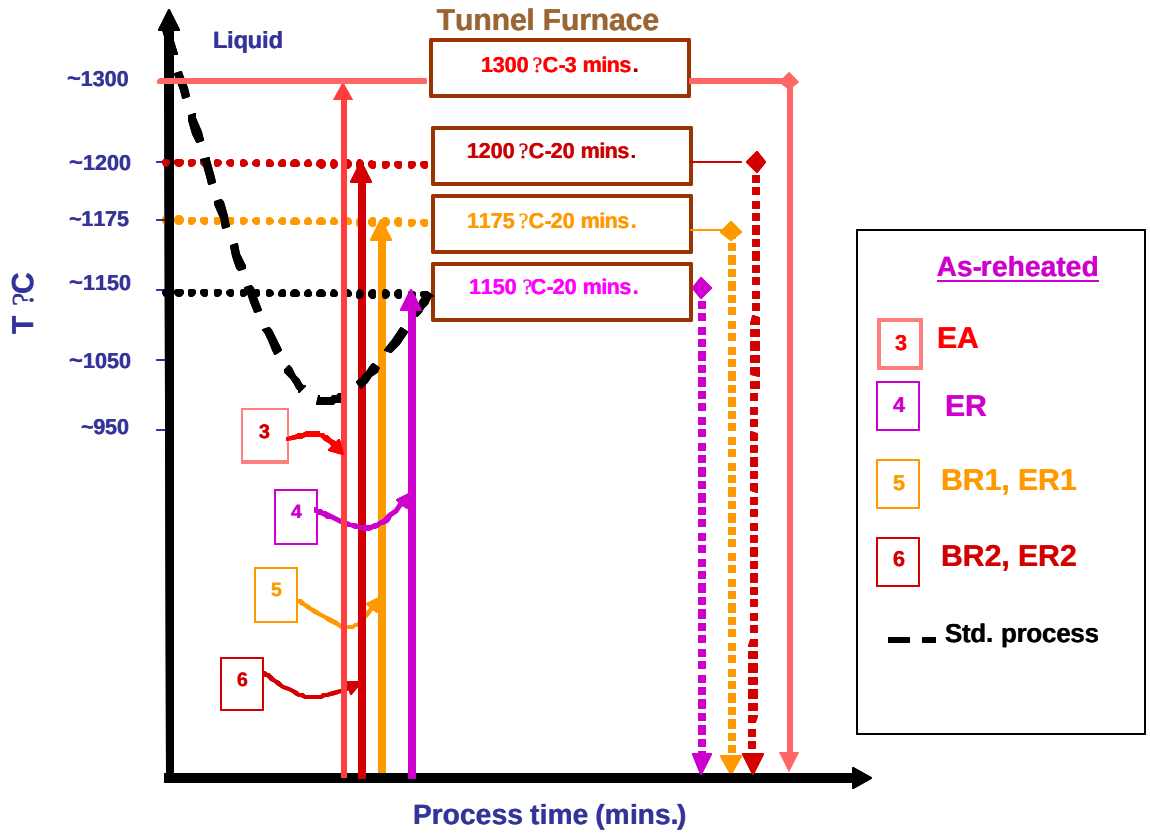

Schematic Diagram 3 Experimental paths followed for the reheating experiments of as-cast steels including EA (Austenitized to 1300 ºC-3mins + water quenched).

4.4 RE-MELTING EXPERIMENTS

Steel E, whose composition is shown in Table 4, was selected for the re-melting practice. It consisted in re-melting the material (~1540 ºC) and simulating the casting process by casting the liquid metal in a pre-designed copper-chill mold. The mold operated automatically. When the slab inside the mold (1 inch thick slab, representing

half of the slab thickness produced in the standard TSC process) reached a certain temperature, a compartment below the mold opened and dropped the slab to be water-quenched to room temperature.

Three melting practices were performed at Oakridge Research National Laboratories (ORNL) in order to examine the solidification structure and the formation of precipitates prior to entering the tunnel furnace. The steels conditions were named (1) EM, for the steel that was melted, cooled down to 1150 ºC and then water quenched, (2) EMT, for the steel that was melted, cooled down to 1150 ºC, held at that temperature for 20 minutes and water quenched, and the third one, (3) EN, which was cooled down to a lower temperature, 1050 ºC and then water quenched. Number (2) was not used.

The experimental paths followed for the re-melting and casting practices are shown in Schematic diagram 4. Microstructural analysis including precipitation behavior was made on the different materials at the surface and quarter point locations. OM, SEM and TEM techniques were used for these analyses.

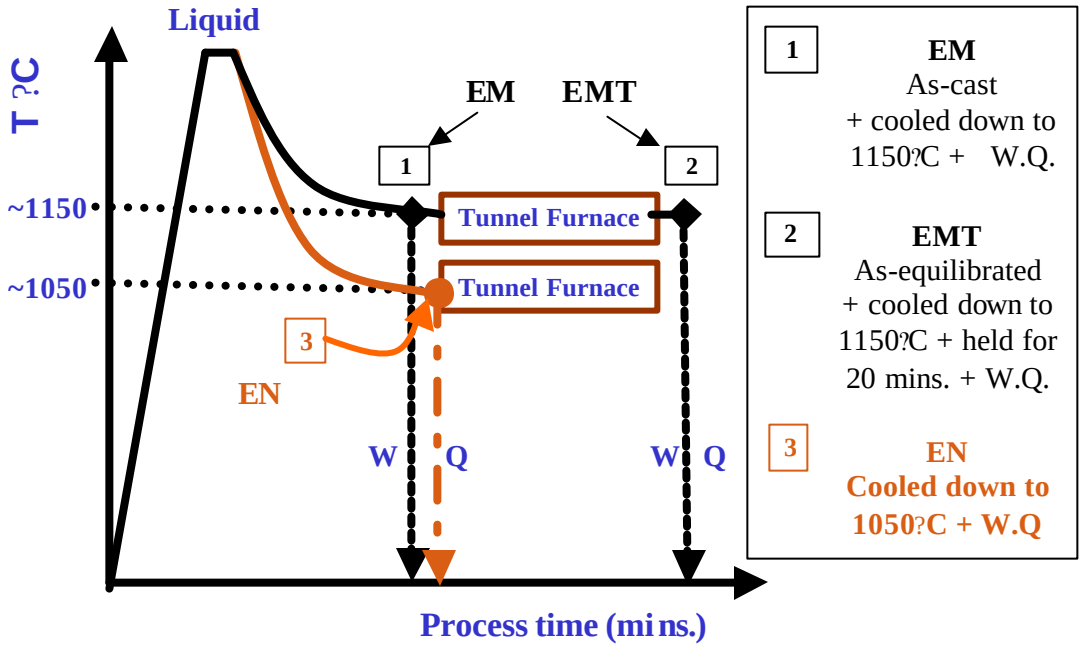

Schematic Diagram 4 Experimental paths followed for the different re-melting and casting practices of steel E.

4.4.1 Scanning Electron Microscopy (SEM)

4.4.1.1 Sample Preparation

Specimens from the different steels were cut from three locations through the thickness (surface, quarter point and center) so as to reveal the solidification structure after being ground and polished. The reagent used to develop the microstructure consisted of 200 ml of aqueous solution of picric acid, 2-4g of sodium dodecylbenzene sulfonate; 2-4ml of HCl and in some cases 0.5g of cupric chloride. For some steels (as-

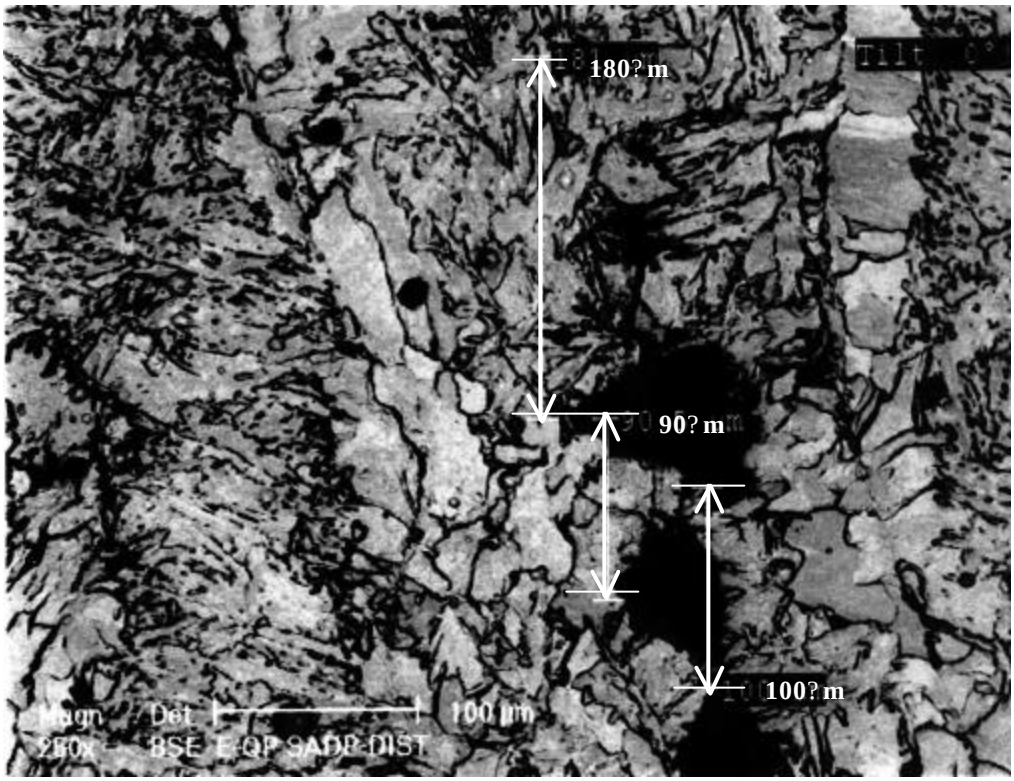

Figure 24 SEM-BSE micrograph showing dendrite pools observed for segregation, the SDAS and the approximate dendrite pool spacing at the quarter point region of steel E.

4.4.2 Transmission Electron Microscopy (TEM & STEM)

Precipitation analysis was made on selected locations of different steels. Several types of precipitates were found. The observations were made on a JEM-200CX transmission electron microscope and a JEOL 2000 scanning transmission electron microscope both operated at 200 kV.

4.4.2.1 Sample Preparation

Thin foils were prepared by cutting 1mm thick specimens from the selected locations with a Buehler diamond disk cut off machine. These samples were ground to ~250?m, and reduced in thickness to ~50?m by severe chemical thinning. This solution consisted of 50 ml distilled water, 50 ml hydrogen peroxide (30%) and 7ml hydrofluoric acid.

In the final stage of chemical polishing and etching, foils were immersed in a solution consisting of 50 ml distilled water, 30 ml nitric acid, 15 ml hydrochloric acid and 7 ml hydrofluoric acid.

Discs of 3 mm in diameter were punched and electrochemically polished at room temperature on a Struers-Tunepol Jet polisher at room temperature and the final thickness of the disc at the center was of ~50-100 nm. Two solutions were used. The first solution was made up of 90% ethanol and 10% perchloric acid and the polishing was run at 40 V and 70-90 mA. The second solution consisted of 400 ml of acetic acid and 80 grams of Sodium Chromate. This solution was carefully prepared by dissolving

the sodium chromate in the acid at room temperature. Magnetic stirring was required for 1 hr. The voltage was 20 - 25 V and a current of 60 - 80 mA. The second solution proved to be more effective for precipitate analysis. The discs were thoroughly cleaned in ethyl alcohol before being taken to the TEM examination.

4.4.2.2 Precipitate Characterization

TEM diffraction and magnification modes were used to identify the different kinds of precipitates present in all steels conditions. Bright field (BF) and dark field (DF) micrographs were taken and developed. Precipitates location, type, size, morphology and volume fraction information were obtained by this TEM technique, whereas quantitative analysis information was obtained by means of the STEM-EDX technique. Precipitates compositions were measured in terms of their average Nb/ (Nb + Ti) measured ratios.

5.0 RESULTS

5.1 MICROSTRUCTURAL OBSERVATIONS

The microstructure observed in water quenched steels B, BT, E and ET are shown in Figure 26 and Figure 26. These are optical micrographs showing the typical microstructure through the thickness of a thin slab (50 mm). Pro-eutectoid ferrite can be seen to delineate the prior austenitic grains and inside the grains there is non-polygonal ferrite. Higher levels of non-polygonal ferrite are observed on the as-cast samples (B and E) than in the as-equilibrated ones (BT and ET). The non-polygonal microstructure seems to have been homogenized by the equalizing treatment. In the industrial practice, the slab is usually held in the tunnel/equalizing furnace for 20 minutes at a temperature of 1150 º C.

5.1.1 Austenite Grain Size

The average austenite grain size values (D_γ in µm) of the two as-cast steels, B and E and as-equilibrated, BT and ET, are shown in Table 6. The D_γ prior to and after the tunnel furnace seemed to be similar. The Nb content does not seem to have a very

strong effect. However, the $D_?$ standard deviation of steel with the higher Nb content both before and after the tunnel furnace is lower than the lower Nb content steel.

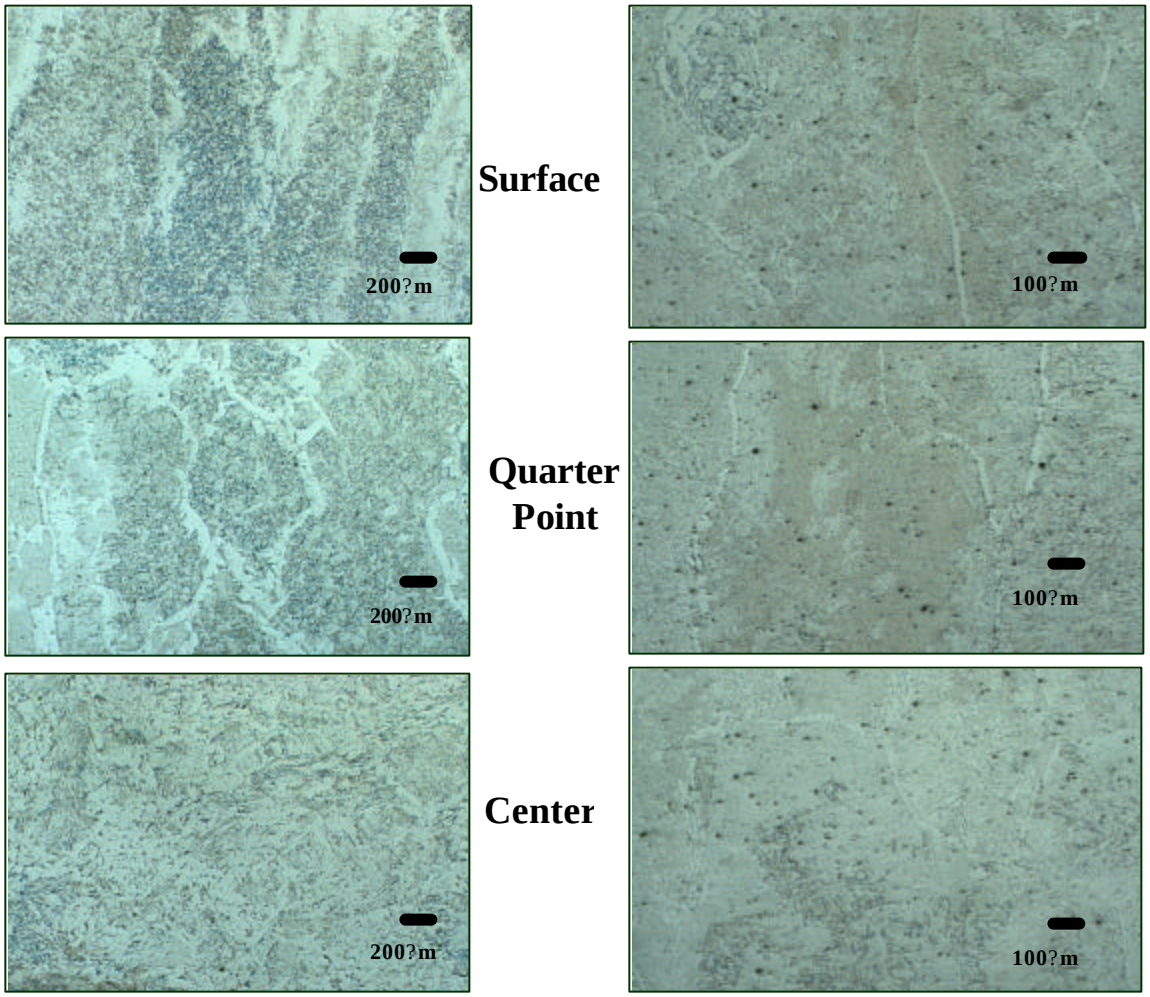

Figure 25 Optical microstructure through the slab thickness of steel B, conditions: a) As-cast and b) as-equilibrated

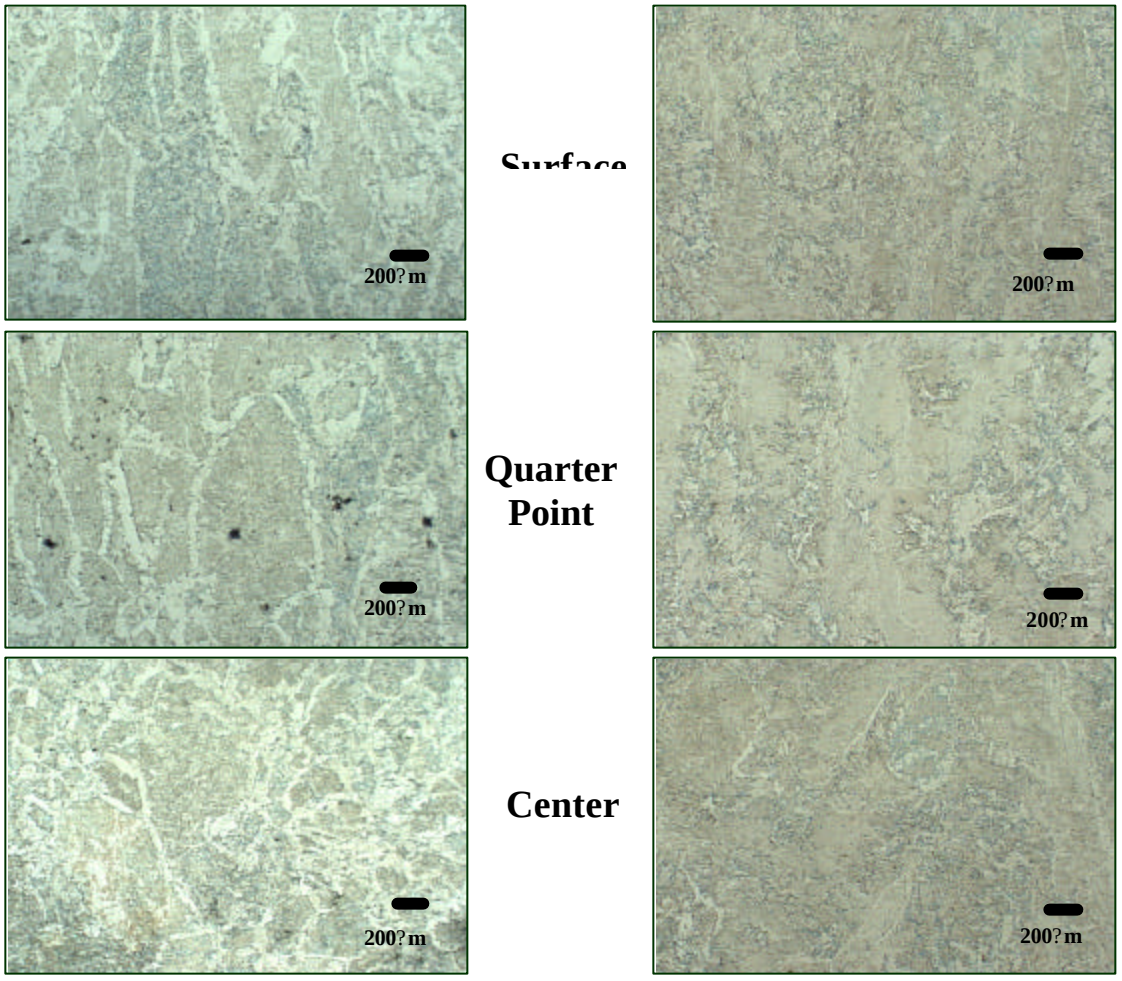

a) Prior to the tunnel furnace-E **b) After the tunnel furnace-ET**

Figure 26 Optical microstructure through the slab thickness of steel E, conditions: a) as-cast and b) as-equilibrated.

Table 5 Average prior austenite grain size as a function of CSP processing stage

Steel - Condition	D_{γ} (μm)	Std. Dev.
B (as-cast)	750	458
E (as-cast)	635	255
BT (as-equilibrated)	682	516
ET (as-equilibrated)	623	339

5.1.2 Microhardness Results

The VHN-500g microhardness measurements through the thickness of as-cast steels B (0.035 %Nb, 0.059 %C, 0.004 %Ti) and E (0.063 %Nb, 0.069 %C, 0.04 %Ti) showed an interesting increase in hardness at the quarter points - Figure 27. The steel with the higher Nb content shows higher hardness values than the low Nb steel. These hardness values, which are higher at the quarter point than at the surface or center locations, are more evident in steel B than E. In order to statistically determine the validity of this variation, a non-parametric statistical test (SPSS statistical analysis software) was performed – Appendix 1. The test resulted in no significant variation among the quarter point peaks and the surface and center locations. This means that

even if the power were increased (power=number of statistical samples), the increase in hardness would not vary much more. Analysis of variance software, ANOVA, could not be used to perform this test since this kind of statistical test requires a normal distribution or Gauss shape curve (bell shape) tendency of the data, i.e. the hardness values at every measured point through the width of the sample and at the different locations through the slab thickness.

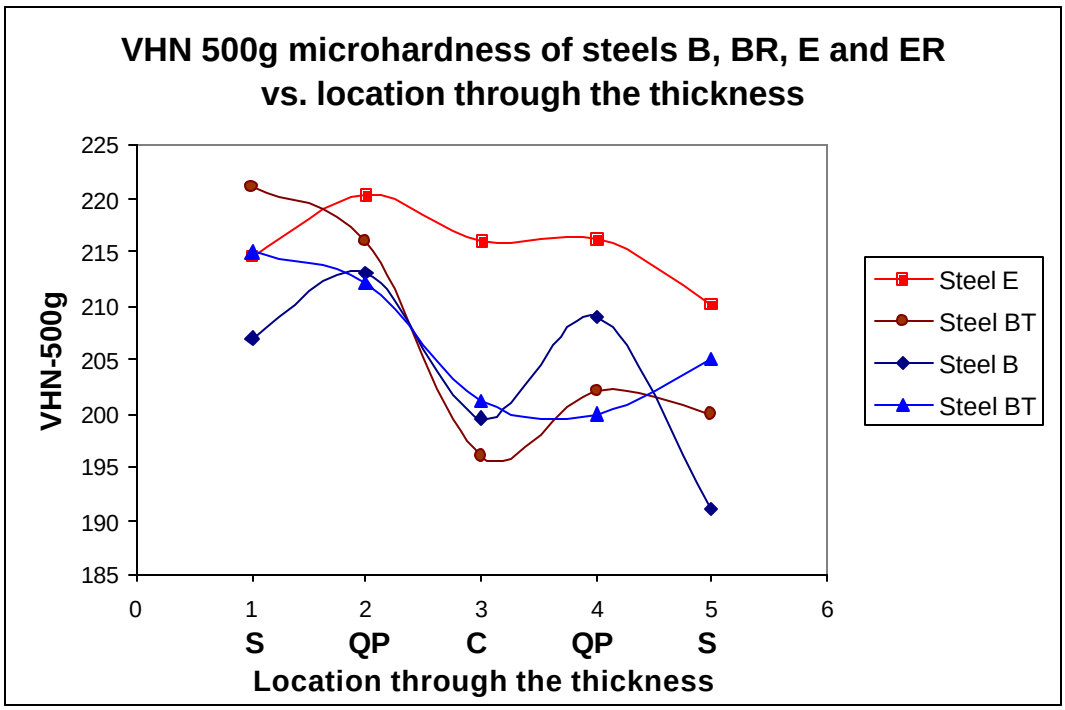

Figure 27 Microhardness of steels (B, BT, E, ET) as a function of location through the slab thickness.

The VHN-500g measurements values in the as-equilibrated samples (after the tunnel furnace) were higher at one of the surfaces of the slab and decreased through the thickness direction.

5.2 THE SOLIDIFICATION STRUCTURE

The characteristic solidification structures observed through the thickness of the thin slabs of steel B and E are presented in Figure 28.

From both dendritic structures, it can be observed that the width and size of the dendrites is smaller at the surface and increases towards the center of the slab. The average secondary dendrite arm spacing (SDAS) was quantitatively measured and showed an increase from surface to center on both steels. Steel B has a SDAS of 100 ?m, 250 ?m, and 280 ?m, surface-quarter point-center. These sizes are larger than the SDAS of steel E, which go from 50 ?m, 125 ?m and 240 ?m, respectively – Figure 29. In order to compare, the plot also shows the results of SDAS measured from a conventionally produced slab reported in the literature[55].

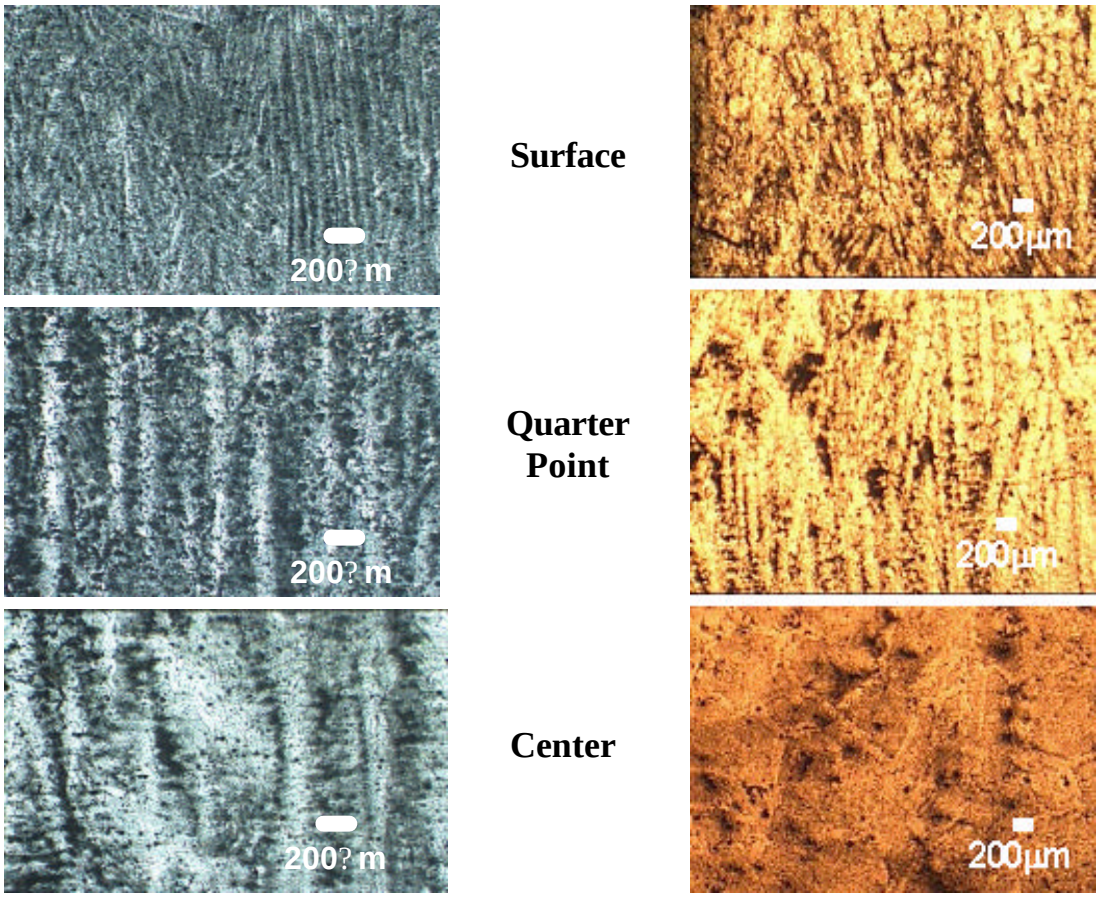

B (0.035%Nb, 0.059%C, 0.004%Ti) **E (0.063%Nb, 0.069%C, 0.04%Ti)**

Figure 28 Dendritic structures of steels B and E through the slab thickness (surface, quarter point and center)

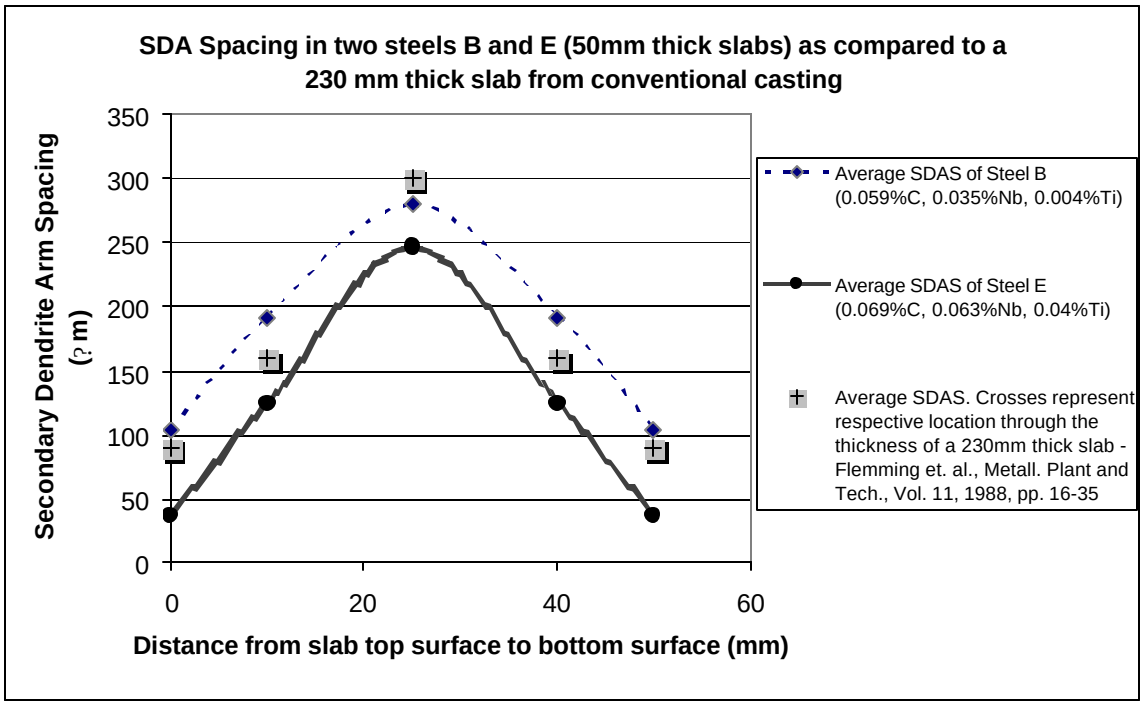

Figure 29 Secondary dendrite arm spacing (SDAS) of steels B and E as a function of the slab thickness

5.2.1 Segregation Analysis Results

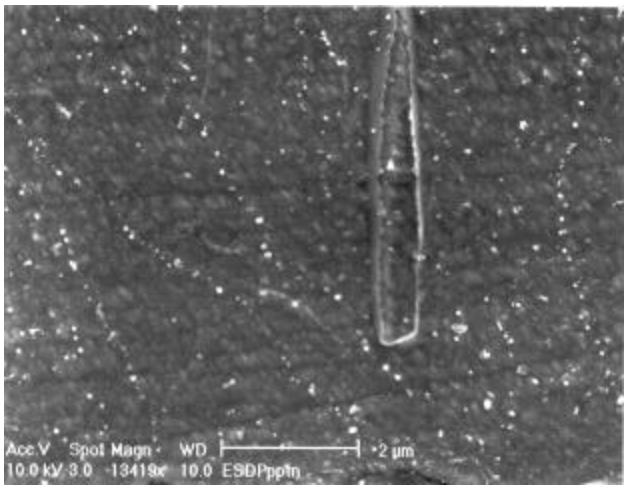

Figure 30 Interdendritic precipitates. “Rows” distribution from the surface region of sample E (as-cast condition)

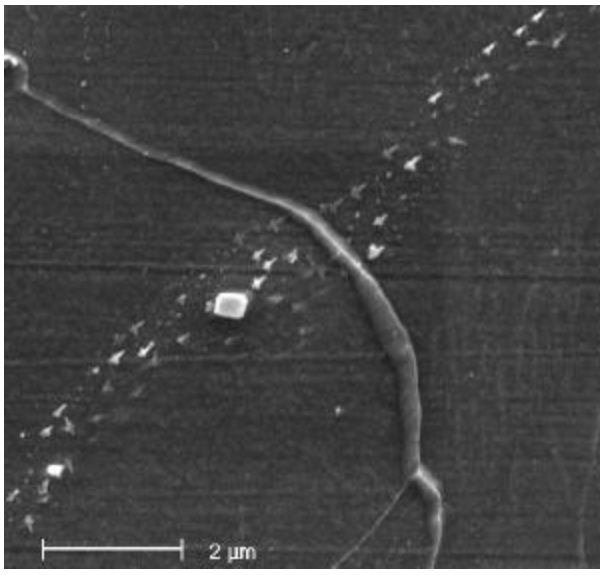

Figure 31 Interdendritic precipitates “band” distribution from the quarter point region of steel B. (Interdendritic pool)

SEM revealed the existence of precipitation on both steels, as-cast and as-equilibrated conditions. Analysis of this precipitation showed the formation of three major types of precipitates: Star-like precipitates, cuboidal, and in a lower amount and smaller size, spherical precipitates. The presence of all these types of precipitates appeared mostly in interdendritic regions (i.e. interdendritic pools). They mainly formed in rows – Figure 30 - which is a typical interdendritic precipitation distribution, formed as the liquid melt front advances towards the solidification of the melt. Solute is rejected as the liquid solidifies forming regions of elevation and depression, the latter being the last to solidify and the richest in solute resulting in segregation enrichment from Nb and Ti in the Fe matrix. They also showed another type of distribution in "bands" of precipitates, most of them star-like - Figure 31.

Mathematical modeling software, JMAT-PRO®, was used to calculate the distribution coefficient, K, of Nb and Ti in d-Fe.

Also, the segregation enrichment factors were calculated, for both Nb and Ti. They are in agreement with the reported in the literature[95, 96].

A series of line scans was performed on as-cast steels (B and E) in order to look for microsegregation; first, across the precipitate rows where an increase in solute (Nb, Ti) intensity is observed as the line scan crosses the precipitates row. A solute depleted zone is observed by the decrease in intensity at the measured spots near the precipitate rows - Figure 32 and Figure 33.

Second, for comparison purposes between the segregation observed in steel E and a more homogenized dendritic structure, line scan was performed on a reheated sample of steel E (as-cast). This sample was reheated to 1300 ºC, held there for three

minutes and water quenched in ice-brine. This austenitized sample (EA), as expected showed a more homogeneous intensity detection shown by the line scan across an interdendritic pool. Figure 34, Figure 35 and Figure 36.

Third, line scans were also performed across the entire dendrite pool (from a primary dendrite core to an adjacent dendrite core) of the two steels B and E to look for segregation. The measured distance ranged from 120 ?m 250 ?m depending on the pool approximate size. Steel B showed larger dendrite pools than steel E. Figure 37 and Figure 38.

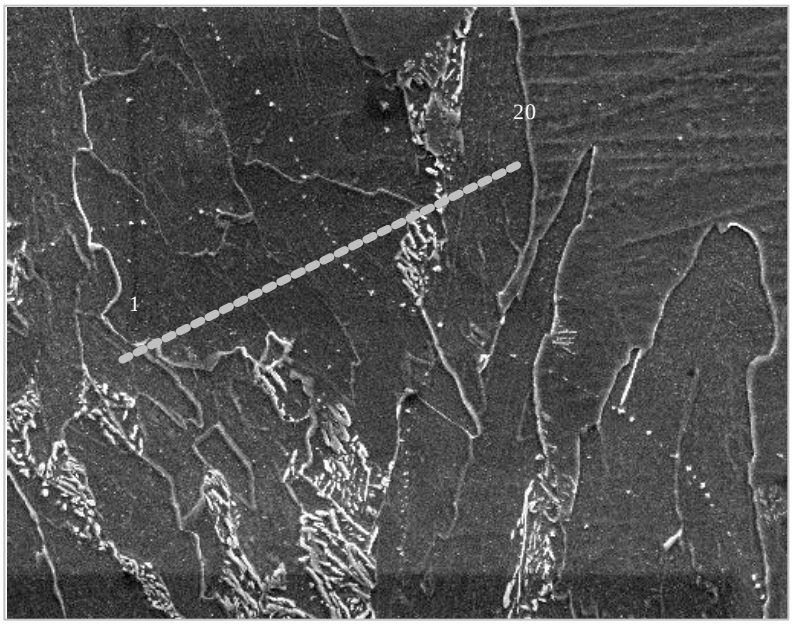

(a)

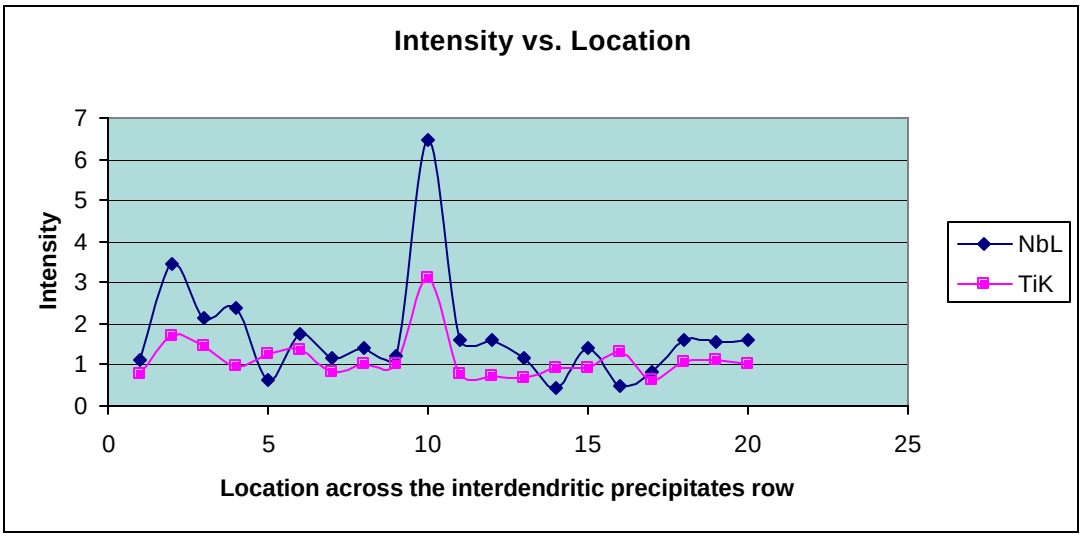

(b)

Figure 32 (a) SEM micrograph showing segregation of Nb and Ti across the interdendritic precipitate row. (b) EDX line scan showing the increase in intensity at the row and a decrease before and after the row (steel E)

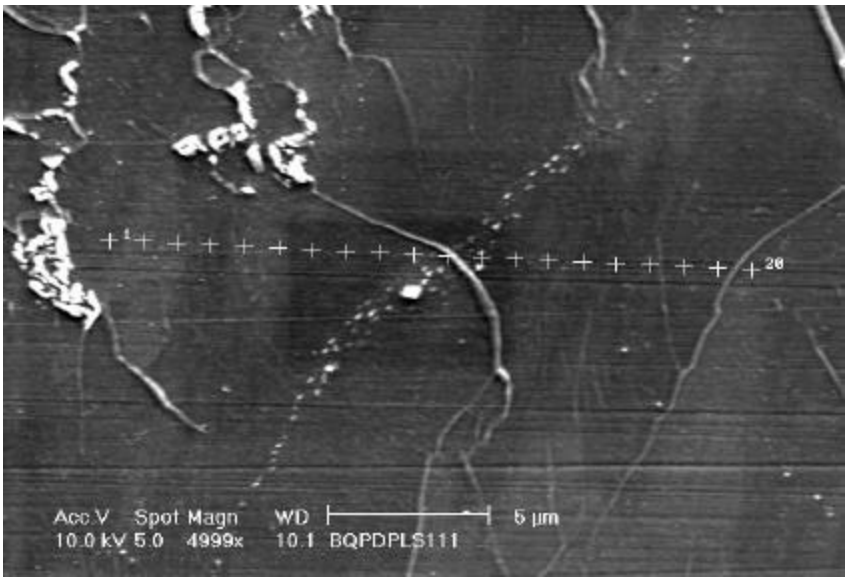

(a)

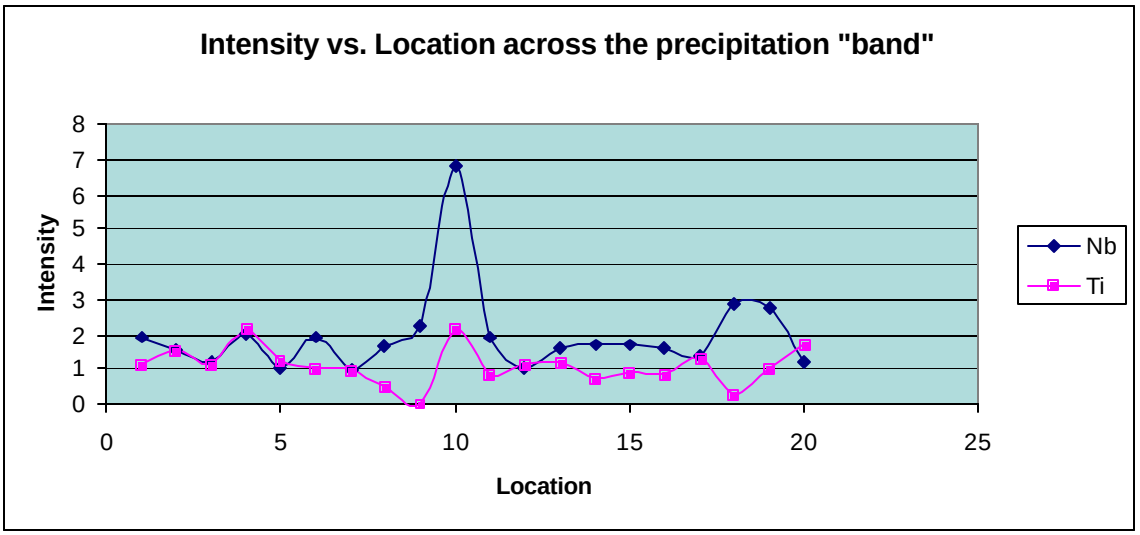

(b)

Figure 33 (a) SEM micrograph showing segregation of Nb and Ti across the dendritic pool precipitation “band”. (b) EDX line scan showing the increase in intensity at the band and a decrease before and after the band (steel B)

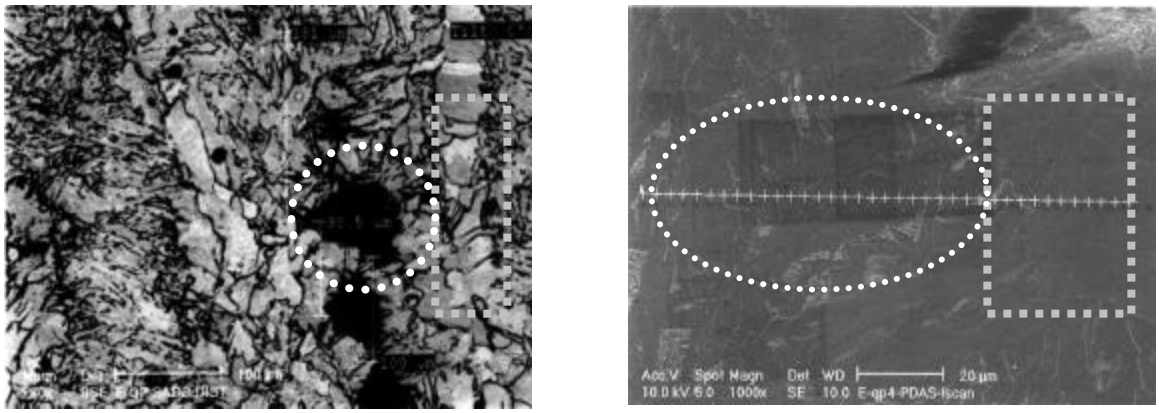

(a) **(b)**

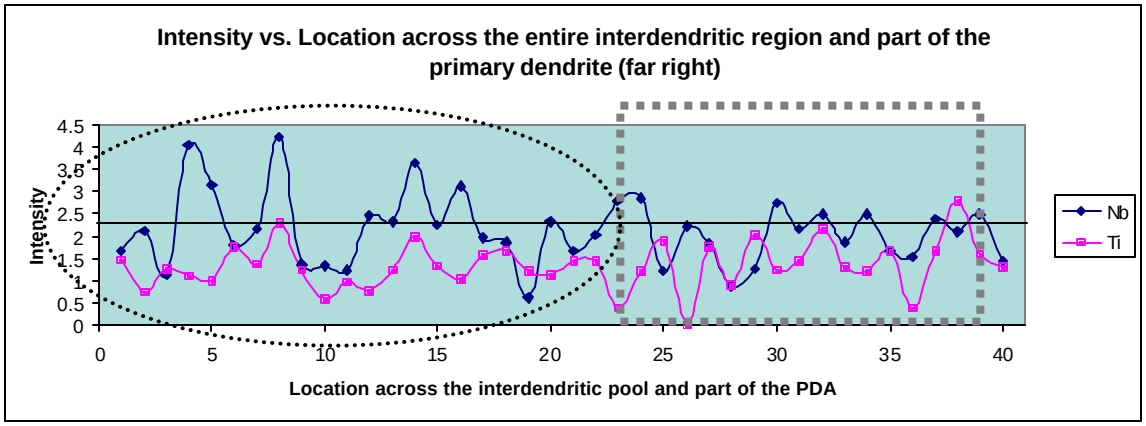

(c)

Figure 34 SEM micrographs showing (a) etched interdendritic region (pool), and (b) the selected interdendritic pool (dotted oval) and primary dendrite (dotted square) across which line scan was performed to look for segregation of Nb and Ti. (c) EDX line scan showing the increase in intensity at some points of the dendritic pool and a decrease at the primary dendrite region (steel E). The line across the chart represents the average intensity.

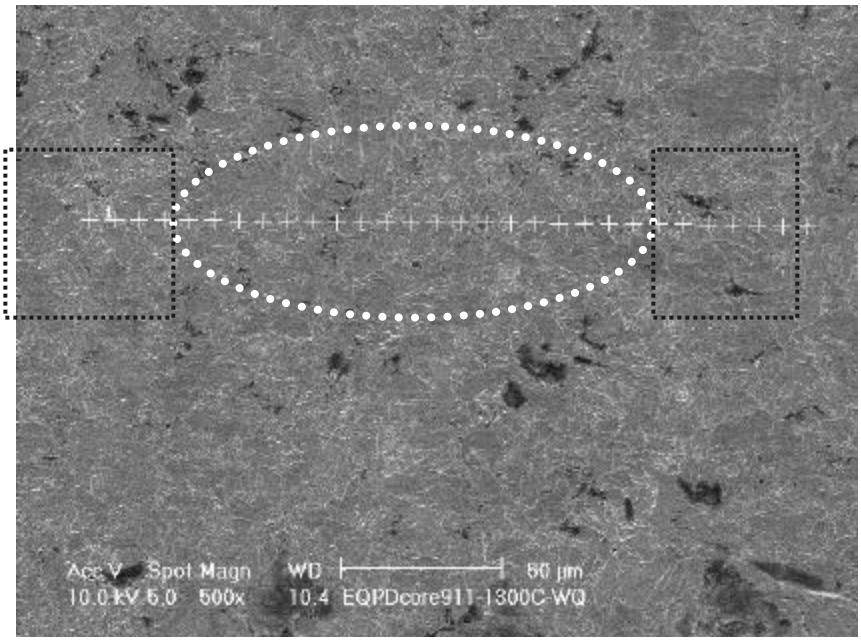

(a)

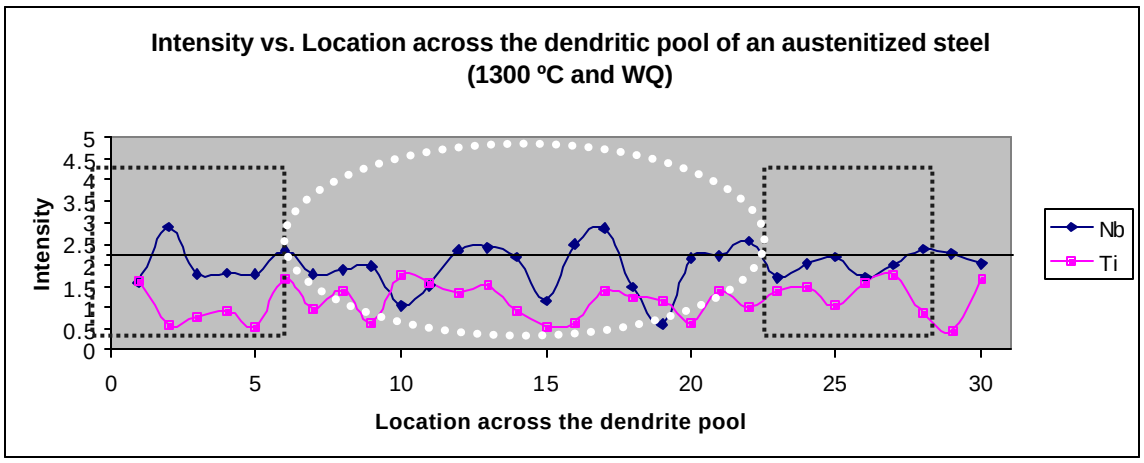

(b)

Figure 35 (a) Selected interdendritic pool (dotted oval) and primary dendrite (dotted square) across which line scan was performed to look for segregation of Nb and Ti. (b) EDX line scan showing constancy in intensity through the entire interdendritic pool and parts of the primary dendrite arm - steel EA. The line across the chart represents the average intensity of steel E.

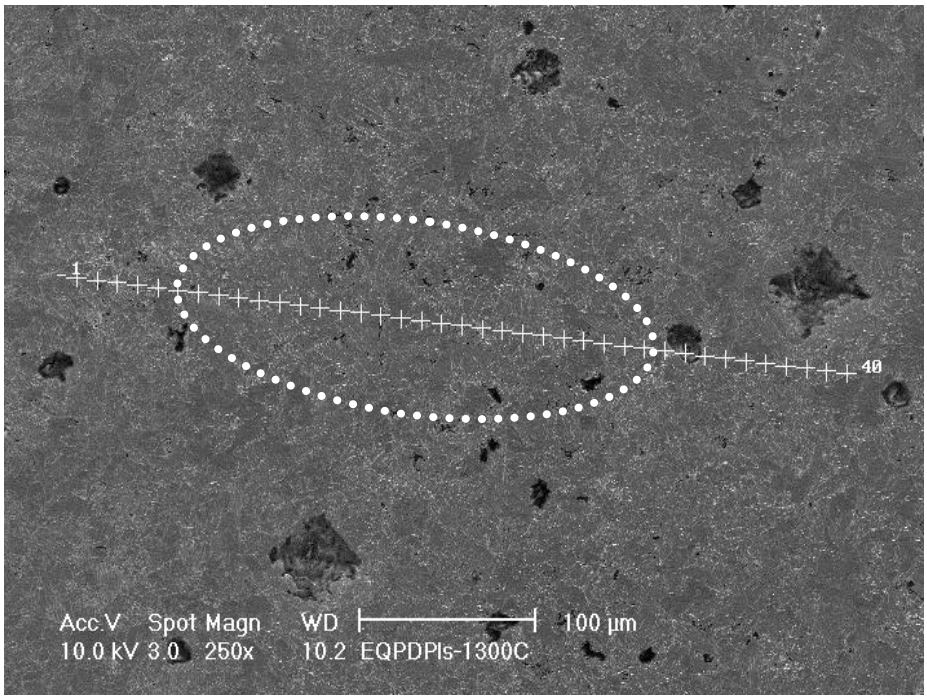

(a)

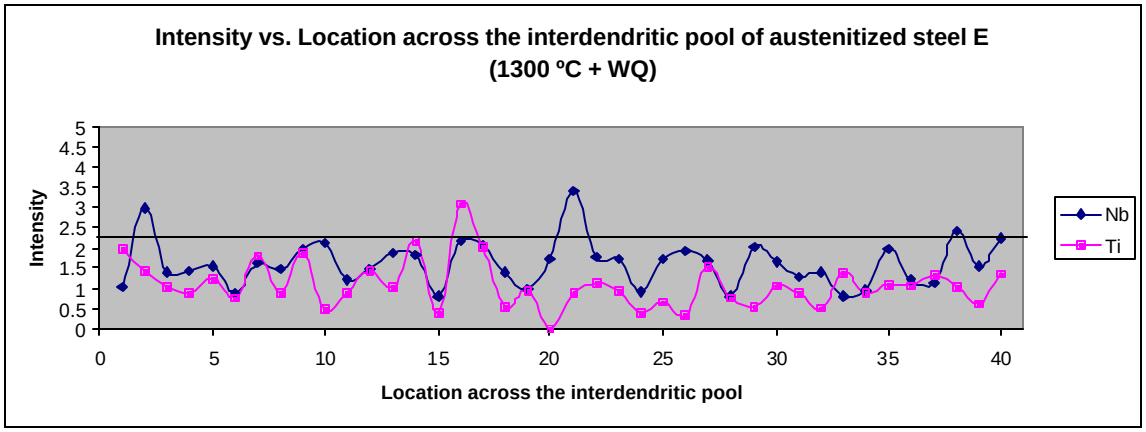

(b)

Figure 36 (a) Selected interdendritic pool and primary dendrite) across which line scan was performed to look for segregation of Nb and Ti. (b) EDX line scan showing constancy in intensity through the entire interdendritic pool and parts of the primary dendrite arm. steel EA. The line across the chart represents the average intensity from steel E.

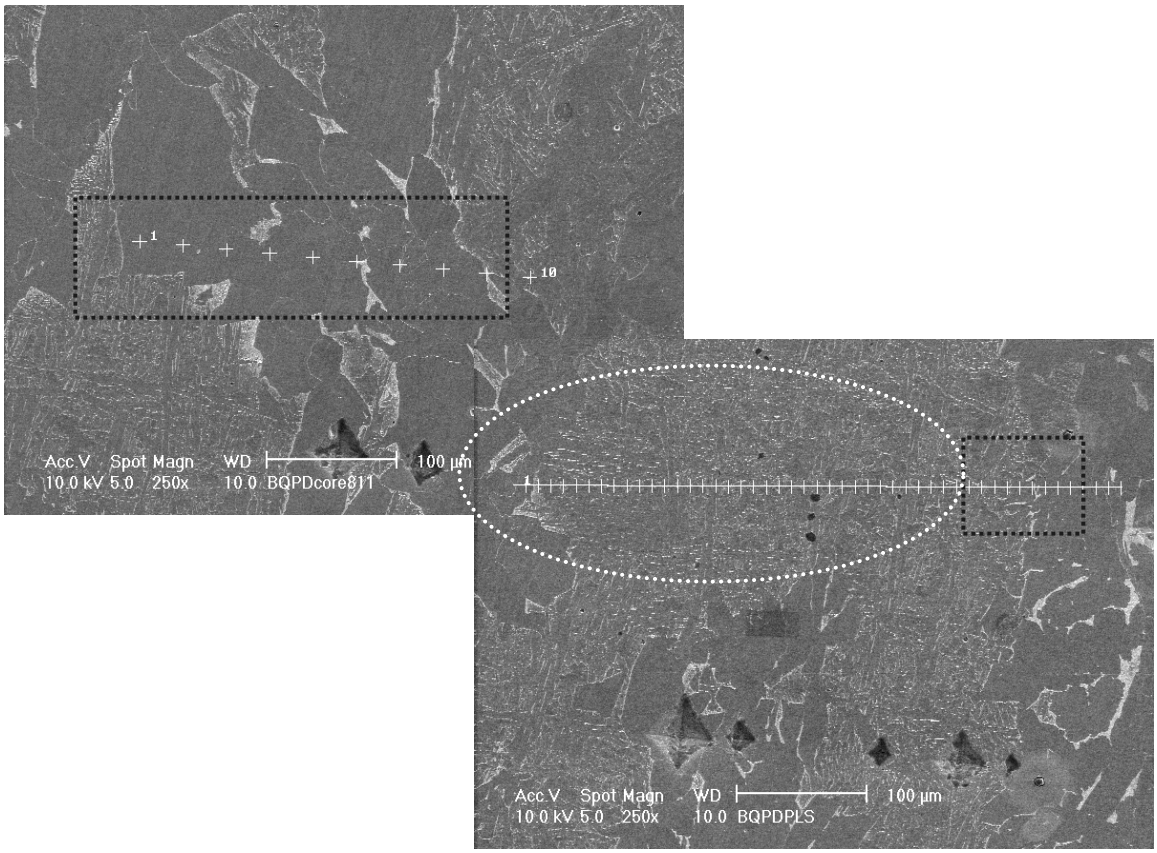

(a)

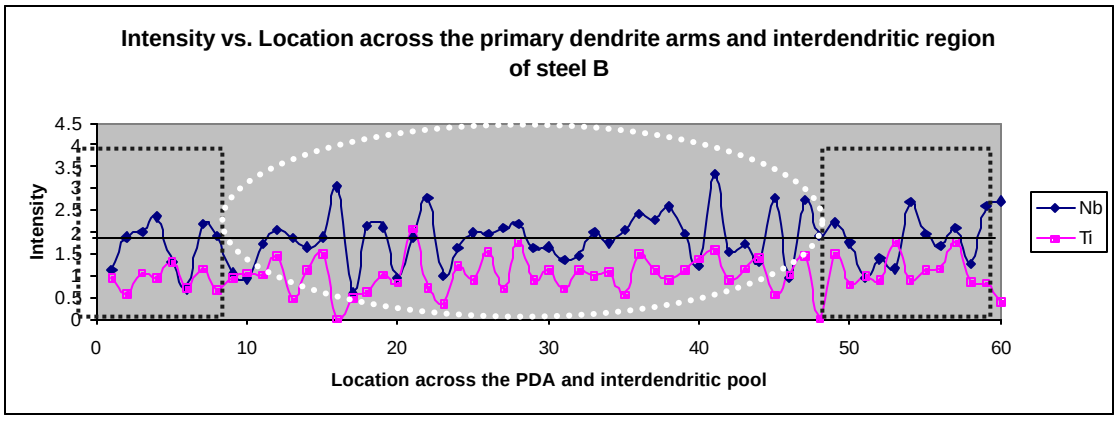

(b)

Figure 37 SEM micrographs showing (a) etched interdendritic region (pool), and (b) the selected interdendritic pool (dotted oval) and primary dendrite arms (left and right dotted squares) across which line scan was performed to look for segregation of Nb and Ti. (c) EDX line scan showing the increase in intensity at some points of the dendritic pool and lower intensity at the primary dendrite region (steel B).

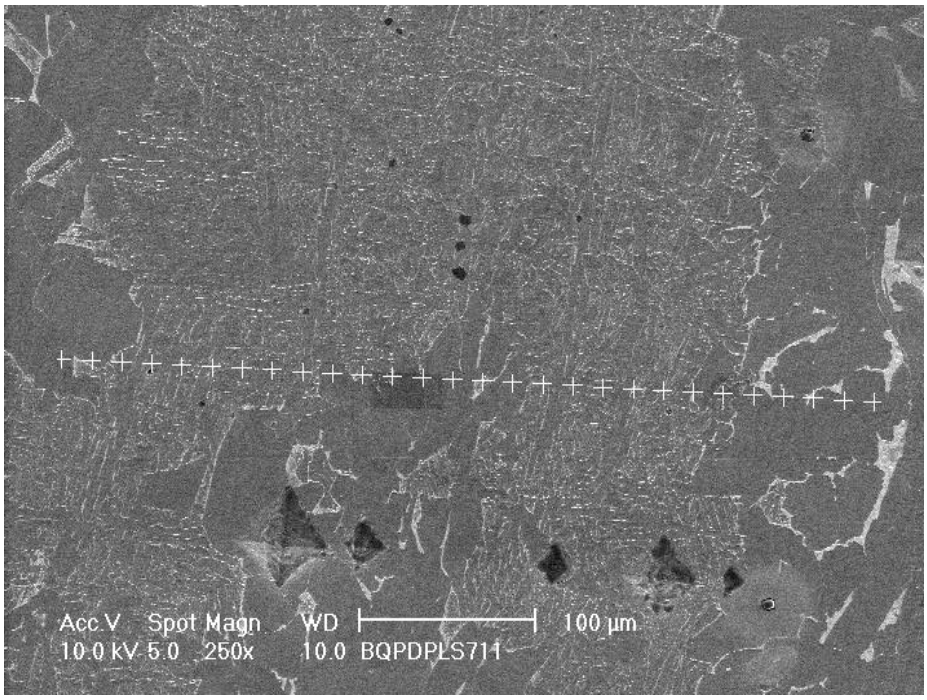

(a)

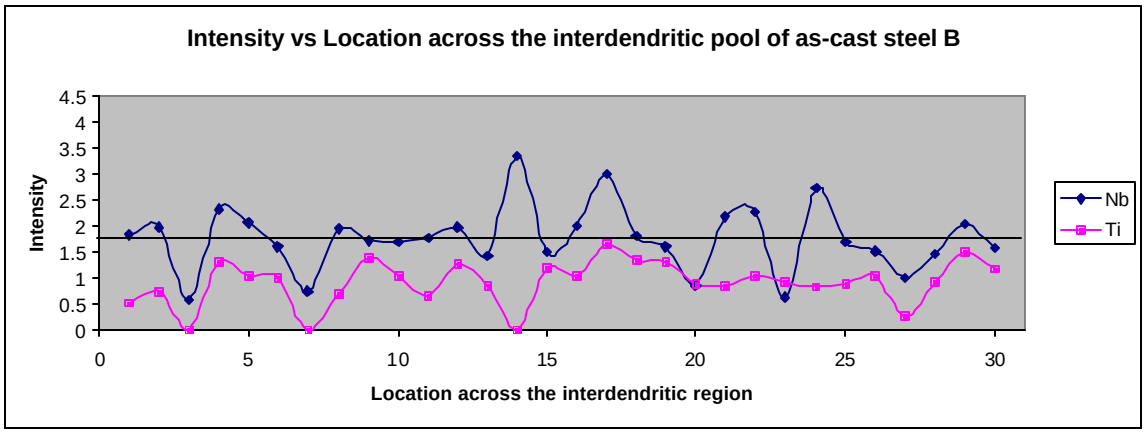

(b)

Figure 38 (a) SEM micrograph showing the interdendritic zone across which line scan was performed to look for segregation of Nb and Ti. (b) EDX line scan showing segregation based on the increase in intensity at some points through the interdendritic region and a decrease before and after the pool (steel B).

The EDX linescan analysis was performed on both steels in order to look for solute segregation in the interdendritic regions. High amounts of precipitates were found in the interdendritic regions compared to the dendritic regions due to segregation. EDX line scans across the interdendritic precipitate rows and across selected interdendritic regions (pools) were performed. The line scans show segregation in terms of the intensity of Nb and Ti. It is observed that as the line scan crosses the row of precipitates, an increase in Nb intensity is detected. Also in the cases where the line scan crosses the entire interdendritic region, a higher intensity is observed than it detects when the dendritic region is scanned. This explains the enrichment of solute in those regions during solidification.

5.3 PRECIPITATE CHARACTERIZATION

The analysis of precipitates in terms of their size, type (morphology), location and volume fraction was conducted using STEM, TEM, SEM, Image Analysis, and OM for simpler microstructural observations.

5.3.1 As-Cast Condition

The study of precipitation for both steels B and E was conducted at the surface and quarter point regions of the commercially produced thin slabs.

The types of precipitates observed in steel E appear in rows or randomly in the matrix - Figure 30. They comprise three types: cuboidal TiN, star-like (Ti, Nb)(C, N), and spherical NbC, all of which are associated with the primary solidification structure and are a result of microsegregation.

TiN precipitates, with a typical cuboidal shape, were arranged mostly in rows. They were found in interdendritic regions only which means they formed at high temperatures during the solidification of the slab Figure 39. The TiN precipitates size in steel E ranged from 50 to 80 nm with a calculated volume fraction of 1.43×10^{-5}. Steel B did not show the precipitation of TiN as much as steel E, but the sizes were much larger. They ranged from 100-400 nm with a volume fraction of 1×10^{-6} – Figure 40. The rest of the titanium may be distributed between the precipitates and the matrix.

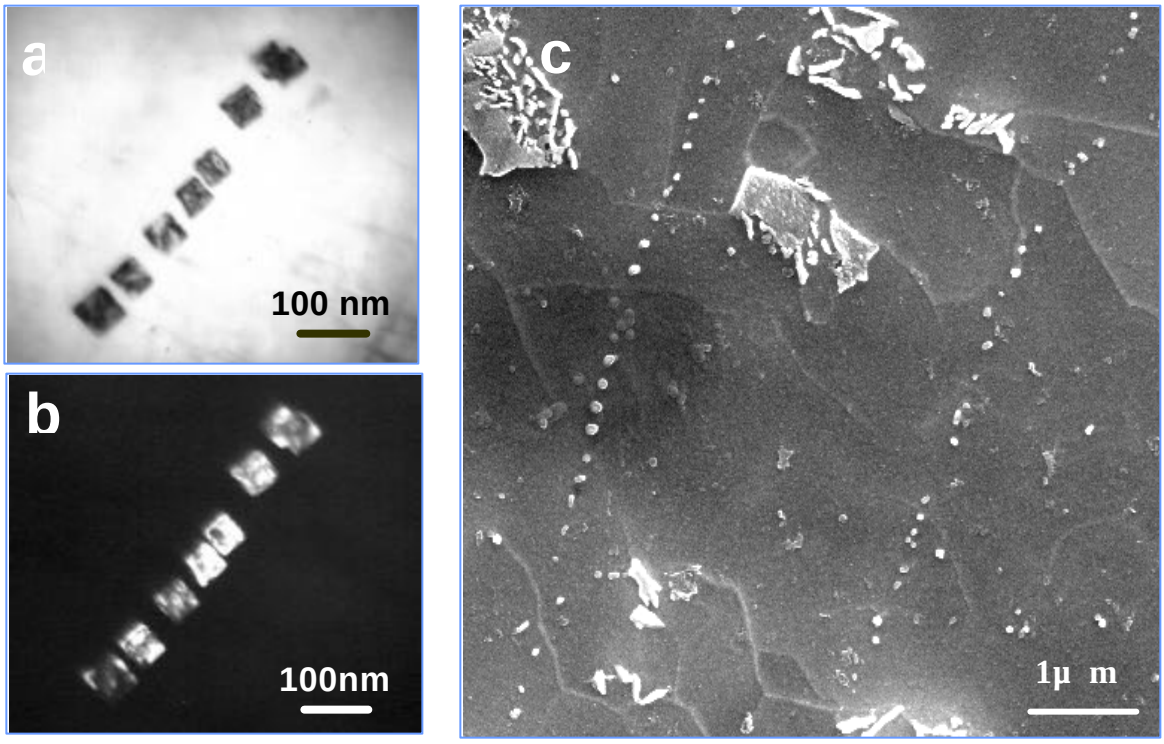

Figure 39 (a) Bright field and (b) dark field TEM micrographs showing typical TiN precipitates (c) SEM micrograph showing general interdendritic distribution of precipitates for steel E.

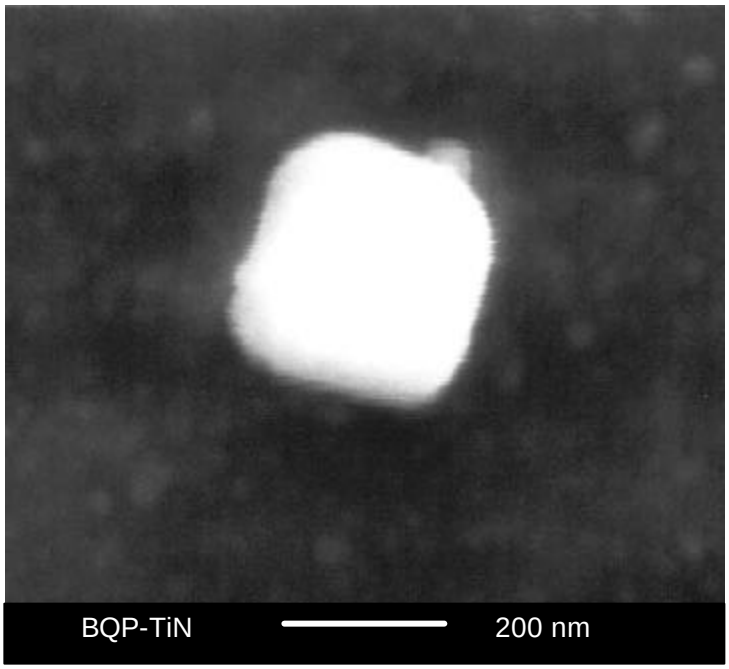

Figure 40 TiN precipitate found in an interdendritic zone from the quarter point region of steel B – SEM micrograph.

Complex (Nb, Ti)(C, N), which precipitate mostly in interdendritic regions, contain a TiN core and a large content of NbC. NbC precipitated epitaxially over the TiN cubes and formed precipitates with a star-like morphology – Figure 41 and Figure 42 (a) and (b). These star-like precipitates have a Kurdjumov-Sachs (K-S) orientation relationship with the final ferrite which means they have precipitated in austenite[97, 98, 99]. The KS orientation relationship is obtained by the precipitates as austenite transforms to ferrite or martensite - Figure 43. In steel E, star-like precipitates size (equivalent diameter), measured in a BioQuant IV Image Analysis system, ranged from 80 to 160 nm and had an estimated volume fraction of 6.2 x 10-4. The complex star-like precipitates observed in steel B had a more symmetric shape than those observed in steel E. It showed mostly star-like precipitation in rows or dispersed randomly in the matrix - Figure 31 and

Figure 42 (c) and (d). In some cases, precipitates formed in “bands” and had a cruciform shape more than a star-like shape, with one arm more elongated than the others – Figure 44. The cruciform shape may be an early stage in the formation of star-like precipitates, which develop six arms instead of four. The arms are similar in composition in both cruciform and star-like being rich in Nb at the arms. Both of these precipitates ranged in sizes from 40 to 100 nm and a calculated volume fraction of 0.9 x 10^{-4}.

In addition to the star-like precipitates size and morphology differences between the two steels, their composition was also different. The average atomic ratios of complex (Nb, Ti)(C, N) star-like precipitates in steel B (0.035%Nb, 0.004%Ti) were 0.659 in the core, and 0.735 in the arm, while in steel E the ratios ranged from 0.563 to 0.672 respectively – Table 6.

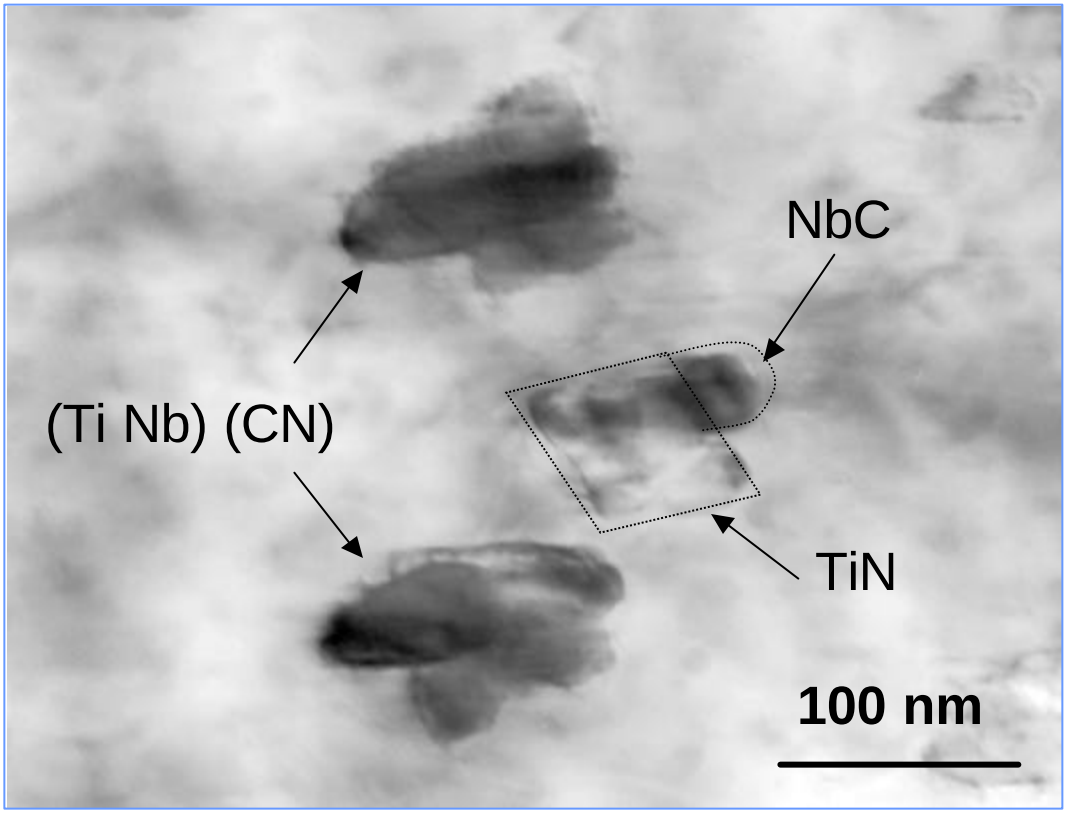

Figure 41 TEM micrograph of as-cast steel E (prior to tunnel furnace) showing the TiN core with the epitaxial precipitation of NbC. Also, complex (Ti, Nb)(C, N) star-like precipitates are observed.

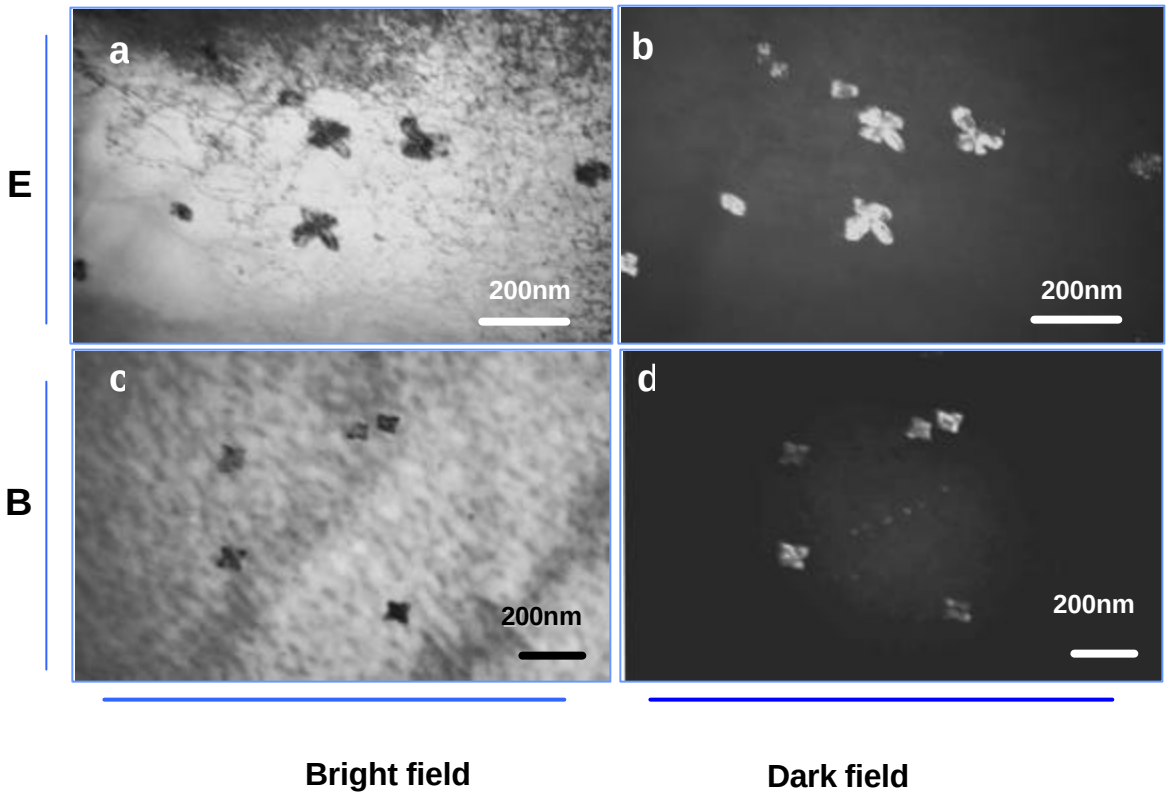

Figure 42 TEM micrographs (left: bright field, right: dark field) showing star-like precipitates from the surface region of as-cast steels. (a), (b) Steel E and (c), (d) steel B.

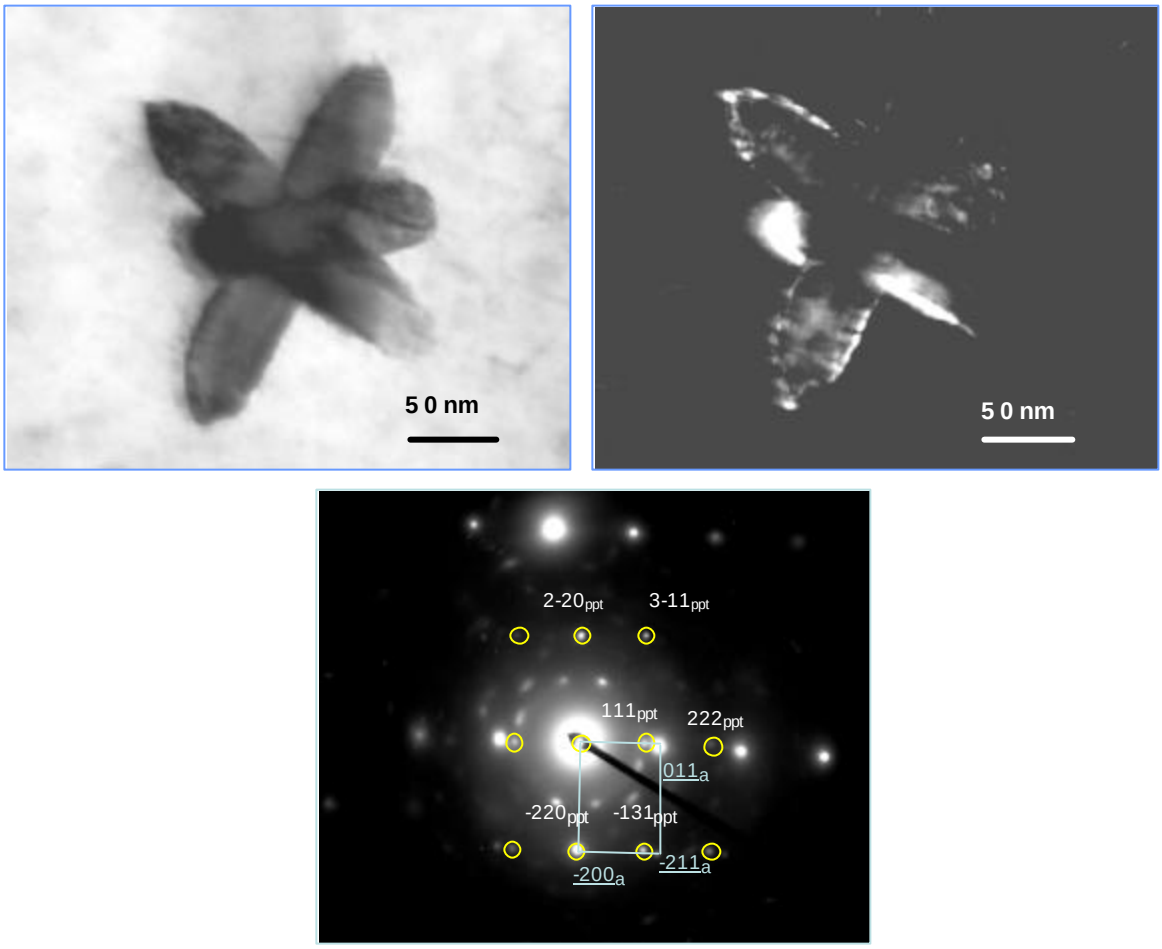

Figure 43 Top: Star-like precipitate from the surface region of steel E (left: bright field, right: dark field). Bottom: Diffraction pattern showing the Kurdjumov- Sachs relationship between the precipitate and the matrix.

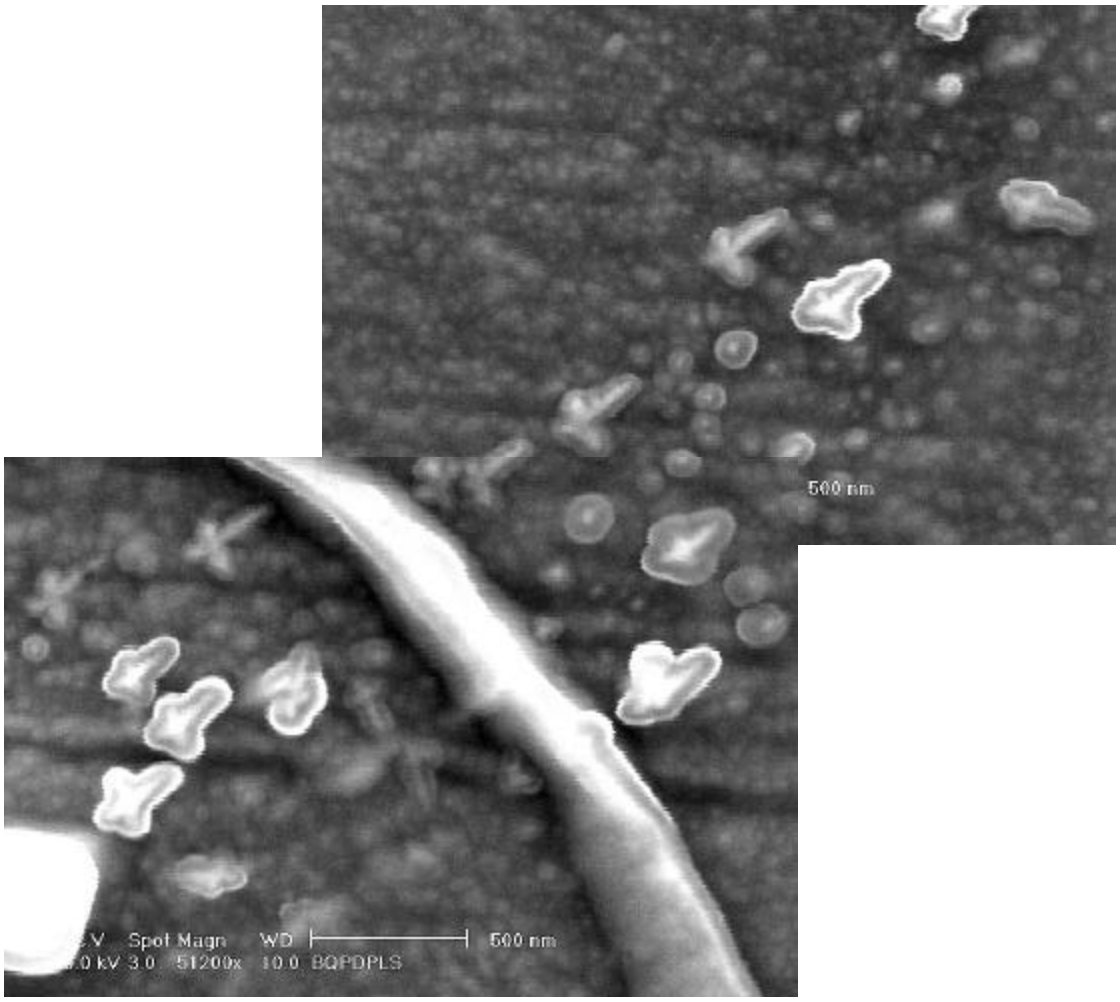

Figure 44 High magnification SEM micrograph showing star-like or cruciform precipitates formed in "bands", inside a selected interdendritic pool from the quarter point region of as-cast steel B.

Other types of precipitates were the spherical NbC in a much lower amount; and, not very frequently found, needle-like precipitates. The volume fraction they occupied was not significantly comparable to the first two types – Figure 45.

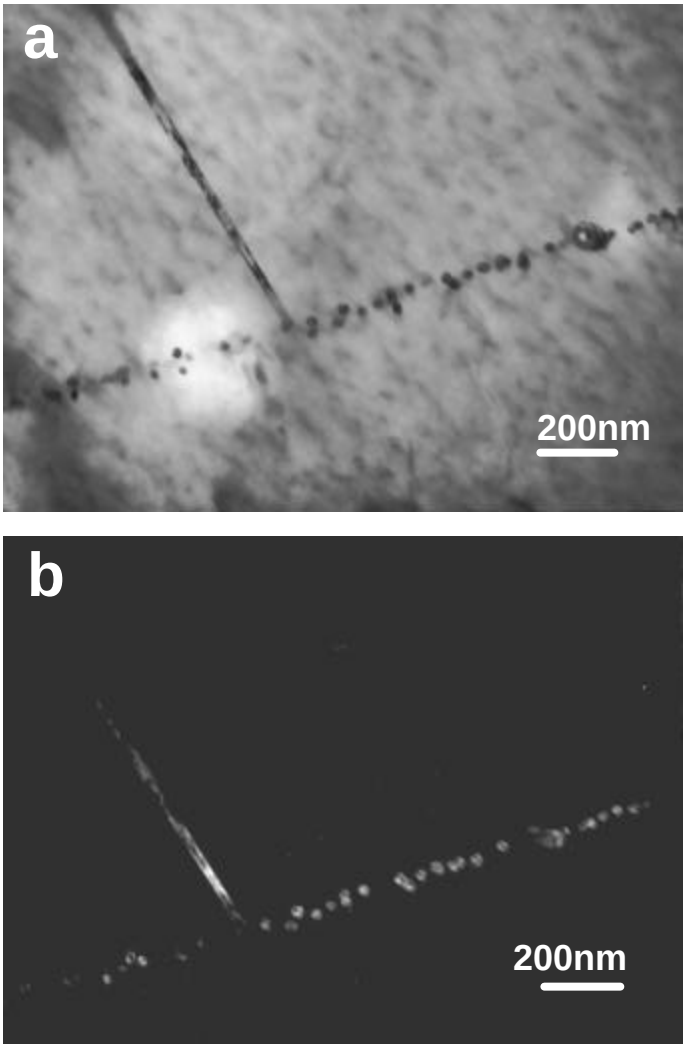

Figure 45 TEM bright field (a) and dark field (b) micrographs showing spherical NbC precipitated in a row, and a needle-like precipitate (not frequently found) from the surface region of steel B

5.3.2 As-Equilibrated Condition

The equilibrating heat treatment applied to the thin slabs in the tunnel furnace, BT and ET, at 1150 ºC for 20 minutes, did not seem to affect the TiN particles observed

previously in as-cast material. The size of these precipitates mostly remains the same, although there is some dissolution of the epitaxially precipitated NbC - Figure 46. On the other hand, the star-like precipitates are affected by the temperature homogenizing treatment by losing their initial symmetry or morphology, and, hence, decreasing in size. The star-like precipitates observed in steel BT ranged from 25 to 50 nm in size (equivalent diameter), whereas in steel ET their size ranged from 30 to 80 nm - Figure 47 and Figure 48 as a result of the equilibrating temperature, 1150 ºC, and the holding time, 20 minutes.

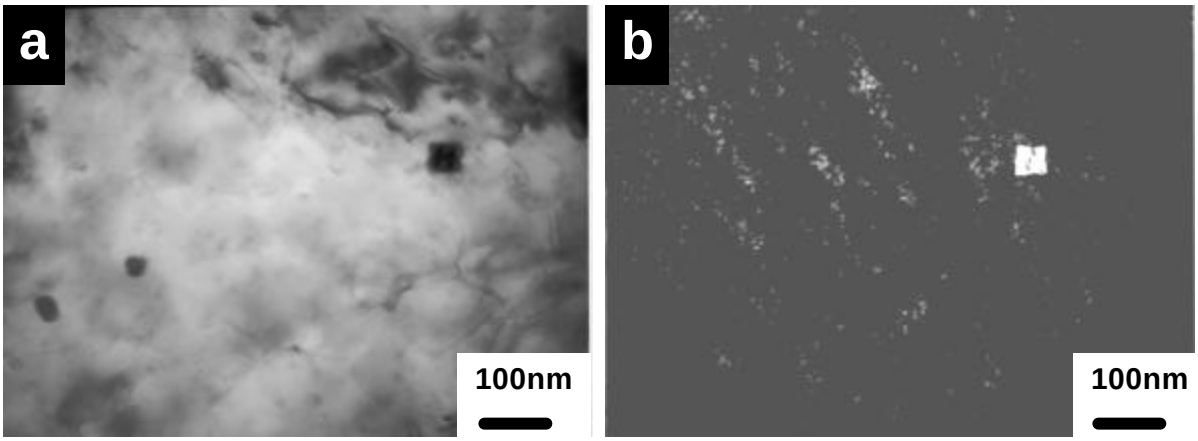

Figure 46 TEM micrographs showing a TiN precipitate in steel BT, (a) bright field and (b) dark field images.

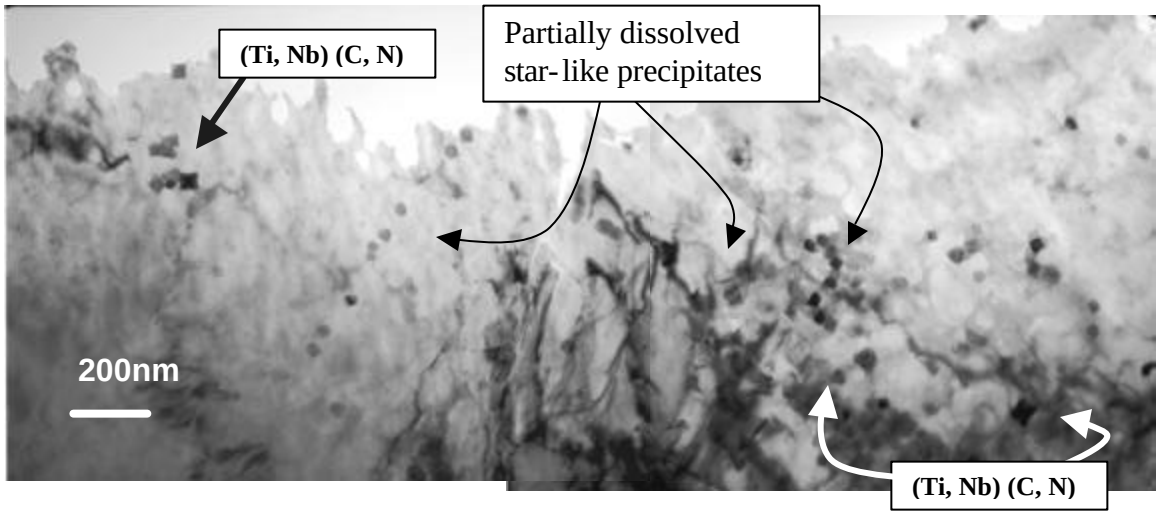

Figure 47 Partially dissolved star-like precipitates from the quarter point region of steel BT (after tunnel furnace). Also showing, rows of precipitates with a general interdendritic distribution type of precipitation as seen in the as-cast condition, steel B.

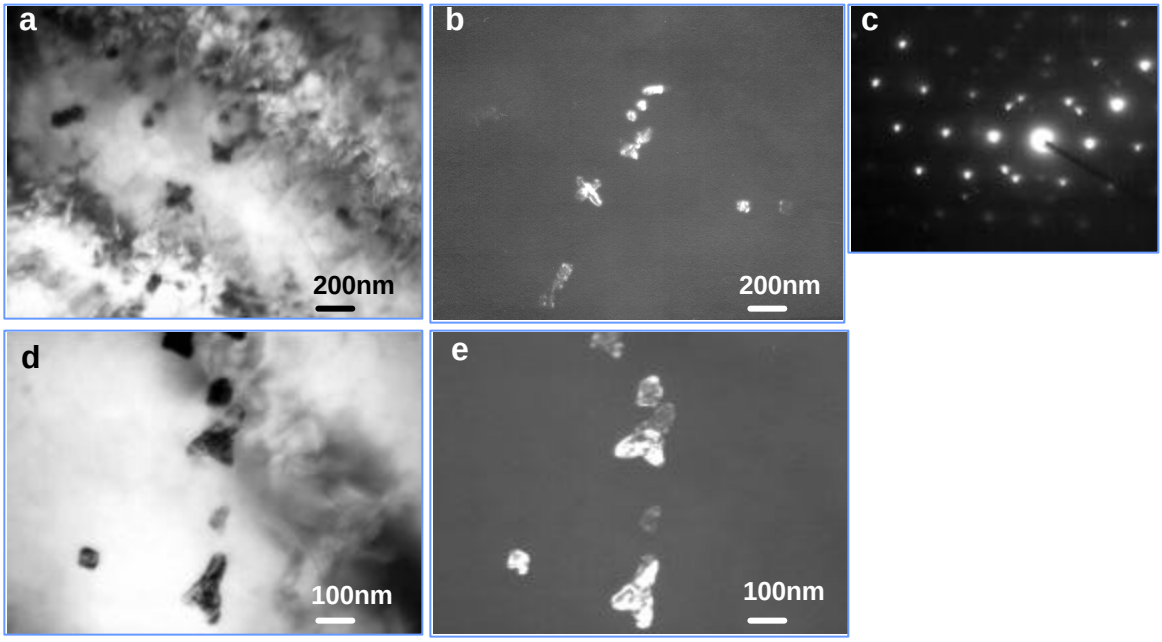

Figure 48 TEM micrographs showing some partially dissolved star-like precipitates; (a) bright field, (b) darkfield and (c) diffraction pattern, the last one showing the precipitates relationship to an f.c.c. matrix (Kurdjumov-Sachs). (d) and (e) show irregular shape star-like precipitates. All from the surface region of as-equilibrated steel ET.

The volume fraction calculated for steel BT was of the order 0.2×10^{-4} and their average atomic ratios ranged from 0.68 in the center to 0.78 in the arms, while for steel ET, the volume fraction calculated was of 8.3×10^{-5}, and their average atomic ratios were 0.575 in the core of the precipitate and 0.61 in the arms – Table 6.

Table 6 Quantitative and chemical analysis of star-like precipitates prior to and after the tunnel furnace

Steels	Average precipitate size (nm)	Volume Fraction (%)	Precipitate composition		Location
			Precipitate type	Nb/(Nb+Ti) (mol/mol) Core - Arm	
E	113	0.062	(Ti, Nb) (C, N)	0.56 – 0.67	Interdendritic regions and random in matrix
ET	55	0.0083	(Ti, Nb) (C, N) Arms Partially dissolved	0.575 - 0.61	random in matrix
B	66	0.009	(Ti, Nb) (C, N)	0.66 - 0.74	Interdendritic regions and random in matrix
BT	39	0.0018	(Ti, Nb) (C, N) Arms Partially dissolved	0.68 – 0.78	random in matrix

5.3.3 Kinetics of Dissolution and Formation of Precipitates

The dissolution study of precipitates included the reheating of the as-cast steel to higher temperatures than those of the industrial practice which is 1150 ºC for 20 minutes. The equilibrating time in the tunnel furnace remains unchanged so as to control the number of variables.

The kinetics of formation involves the re-melting of one of the steels, its casting, and water-quenching from two different solidification temperatures prior to the tunnel furnace. This was in order to determine if the importance of the temperature control before the slab enters the tunnel furnace, and how this can prevent the formation of star-like precipitates at an early stage in the process. Steel E, with the higher Nb and Ti content, is used for this practice.

5.3.3.1 Reheating Experiments - As-Reheated Condition

The first of the reheating experiments to 1150 ºC was performed to verify that the conditions of the original as-cast steel were reproducible in terms of precipitation. The results showed that the characteristics were fairly similar so the following reheating experiments to higher temperatures were performed.

The reheating treatments to 1175 ºC showed the existence of TiN even after reheating the steels to such temperatures – Figure 49. The dissolution of star-like precipitates is observed to a higher extent than it showed in as-equilibrated conditions, as expected. The average star-like precipitate size for steel BR1 was 13 nm and for steel ER1, the average size was 50 nm. The evaluated volume fraction of these precipitates in BR1 was of 2.3×10^{-6}, and their measured atomic ratios ranged from 0.6 in the core to 0.7 in the arms. Regarding steel ER1, the calculated volume fraction of dissolved star-like precipitates was of 3.16×10^{-5} and the measured atomic ratios ranged from 0.54 in the core to 0.61 in the arms. The reheating treatments to 1200 ºC showed, in the case of steel BR2, that all star-like or cruciform precipitates previously

seen in as-cast material B, had been completely dissolved, hence, the size was not measured due to the absence of precipitates in the areas observed. In the case of steel ER2, the average precipitate size was 48 nm and a calculated volume fraction of 0.0018% – Table 7. Figure 50,Figure 51, Figure 52 and Figure 53.

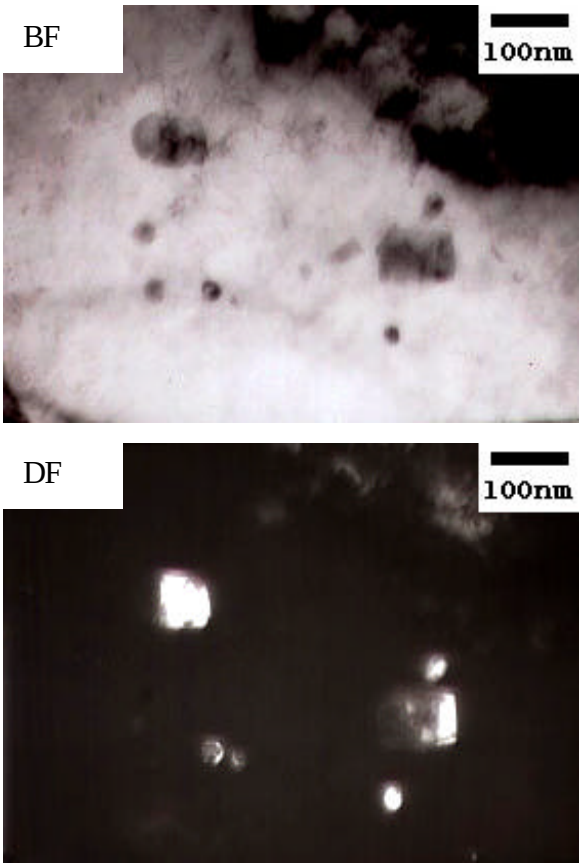

Figure 49 TEM micrographs showing TiN at the quarter point of steel BR1.

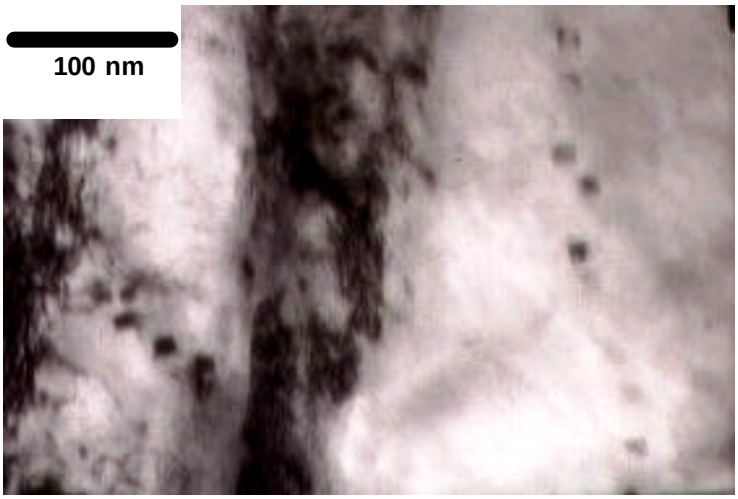

Figure 50 Dissolved star-like precipitates in rows from the quarter point region of steel BR1

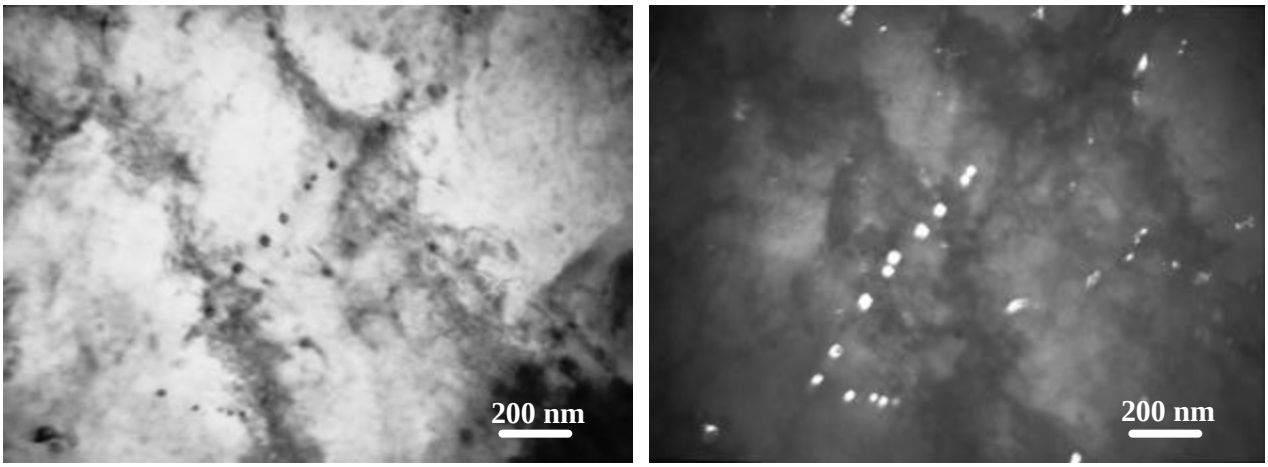

Figure 51 Remains of dissolved star-like precipitates (distributed in rows) observed in the surface region of steel ER1 (TEM, left: BF, right: DF).

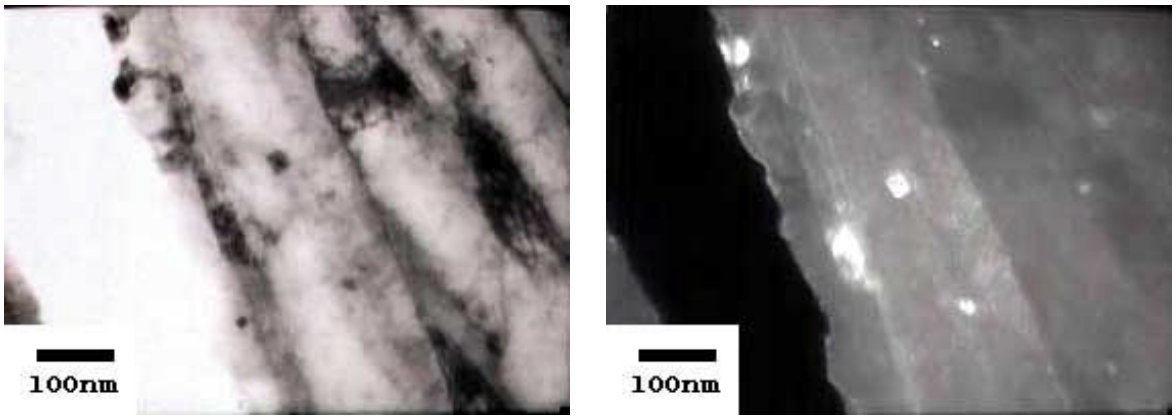

Figure 52 Completely dissolved star-like precipitates after being reheated to 1200 ºC for 20 minutes (quarter point region of steel BR2).

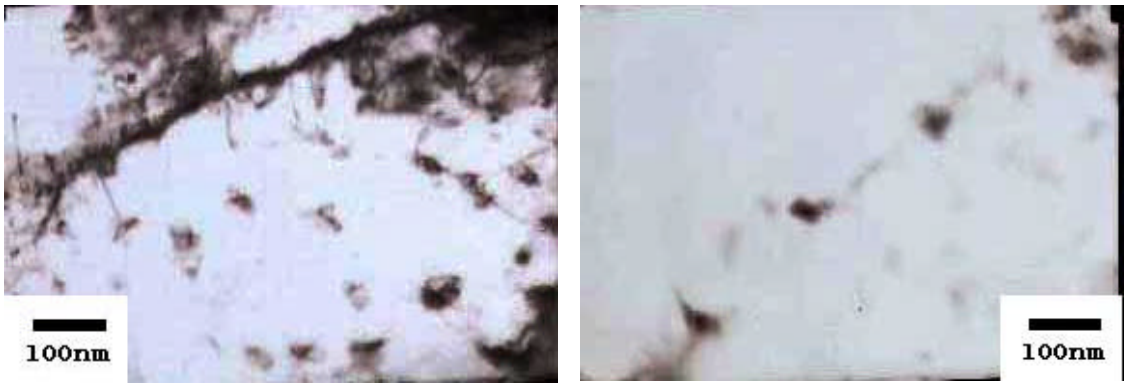

Figure 53 Remains of dissolved star-like precipitates after being reheated to 1200 ºC for 20 minutes (from the surface region of steel ER2)

Table 7 Quantitative and chemical analysis of star-like precipitates for the reheating experiments (1175 ºC and 1200 ºC)

Steels	**Average precipitate size (nm)**	**Volume Fraction (%)**	**Precipitate composition**		**Location**
			Precipitate type	**Nb/(Nb+Ti) (mol/mol) Core - Arm**	
ER1 1175 °C	50.5	0.0083	(Ti, Nb) (C, N) Arms Partially dissolved	0.54 – 0.61	random in matrix
ER2 1200 °C	48	0.0018	(Ti, Nb) (C, N) Arms completely dissolved	NA	random in matrix
BR1 1175 °C	13	0.00023	(Ti, Nb) (C, N) Arms Partially dissolved	0.60 - 0.70	random in matrix
BR2 1200 °C	NA	NA	(Ti, Nb) (C, N) Arms completely dissolved	NA	random in matrix

5.3.3.2 Quantitative Analysis of Star-like Precipitates

In this section, some examples on how the measurements were performed on the precipitates are shown.

The technique used to measure the compositions was the Scanning Transmission Electron Microscopy (STEM). The measurements were based on atomic and weight ratios, calculated in terms of number of counts of each element detected by the EDX, since no method of correction was used; there was not a standard material for reference regarding the steels accurate composition. In spite of this, the measurements were based on the Nb-Ti ratios and the results show the effect of all the heat treatments on both steels.

It is important to mention the following considerations for the STEM-EDX analysis:

- Precipitates analyzed by EDX analysis in STEM microscope were observed at very high magnifications (up to 500 K).
- After the analysis, most of the particles were destroyed due to the beam intensity.
- Several precipitates with similar features had to be found and analyzed, in order to get the representative measurements of Nb/(Nb+Ti) atomic ratios of both arms and center locations.

The results of the calculated ratios Nb/(Nb + Ti) are reported in Table 6 for as-cast and as-equilibrated conditions, and in Table 7 for as-reheated conditions.

5.3.3.2.1 Steel Conditions B and BT

The analysis of star-like precipitates, for instance, the one depicted in Figure 54 and Figure 56, was made on the arms and center. The corresponding spectra to the measured locations are shown in Figure 55 and Figure 57, respectively.

5.3.3.2.1.1 As-Cast Condition - B

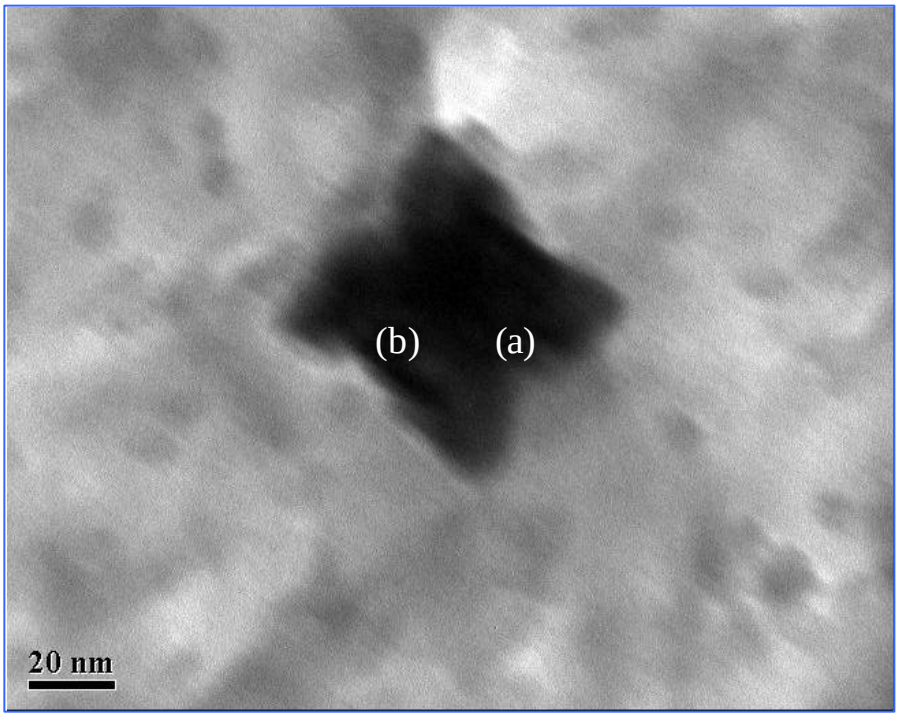

Figure 54 STEM micrograph showing the locations where EDX analysis was performed on a star-like precipitate, (a) right arm and (b) center.

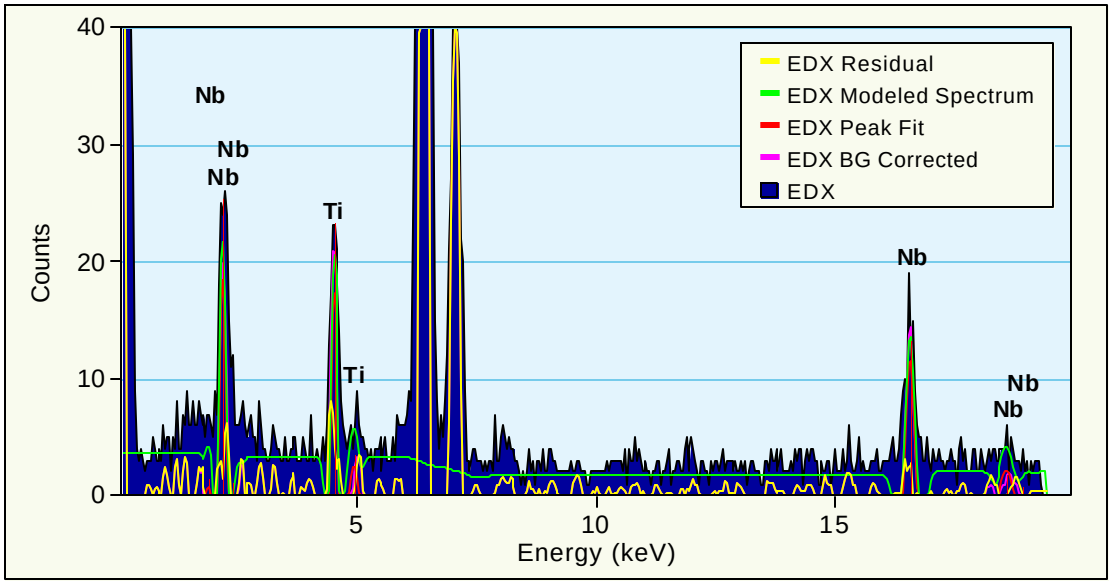

(a)

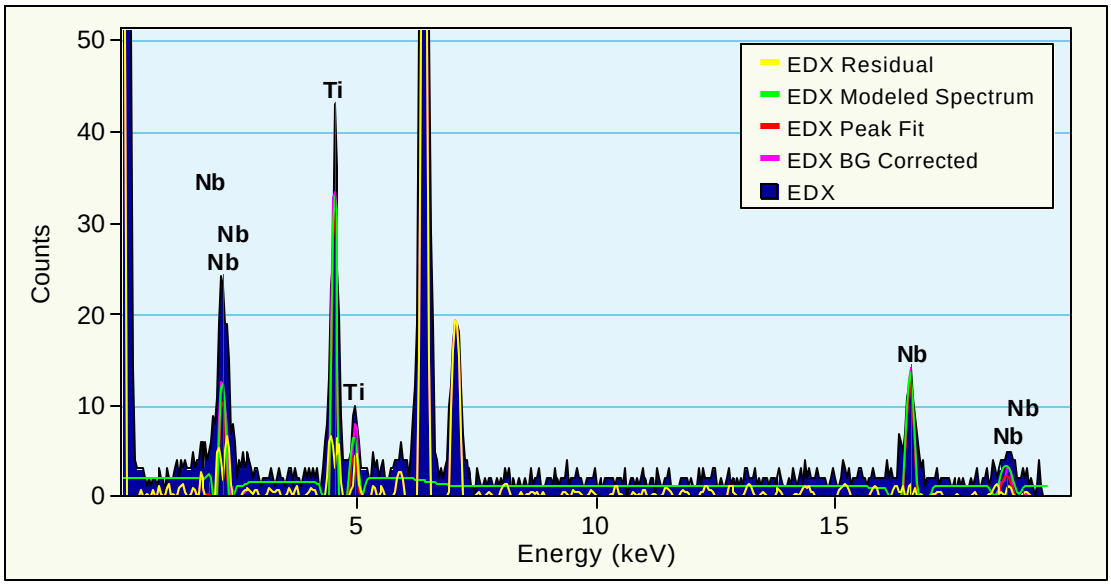

(b)

Figure 55 EDX spectra corresponding to (a) arm and (b) center locations of the star-like precipitate shown in Figure 54.

5.3.3.2.1.2 As-Equilibrated Condition – BT. STEM-EDX analysis was made on precipitates with partially dissolved arms like the one shown in Figure 56 . Analyses on the core and arms were performed as shown.

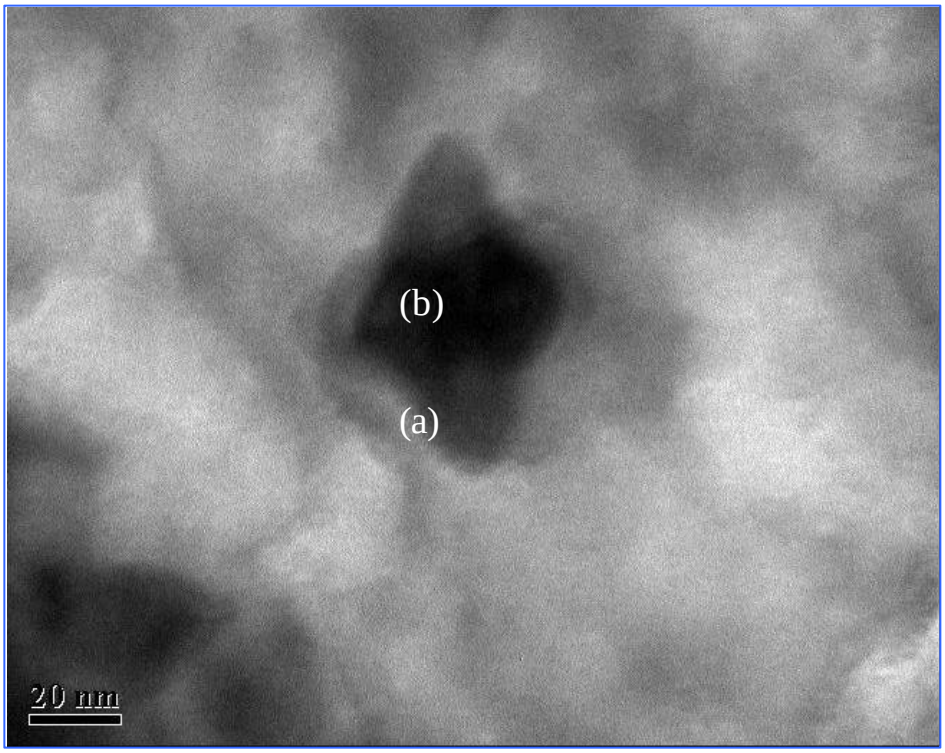

Figure 56 STEM micrograph showing the locations where EDX analysis was performed. (a) Lower arm from quarter point region of as-equilibrated steel BT.

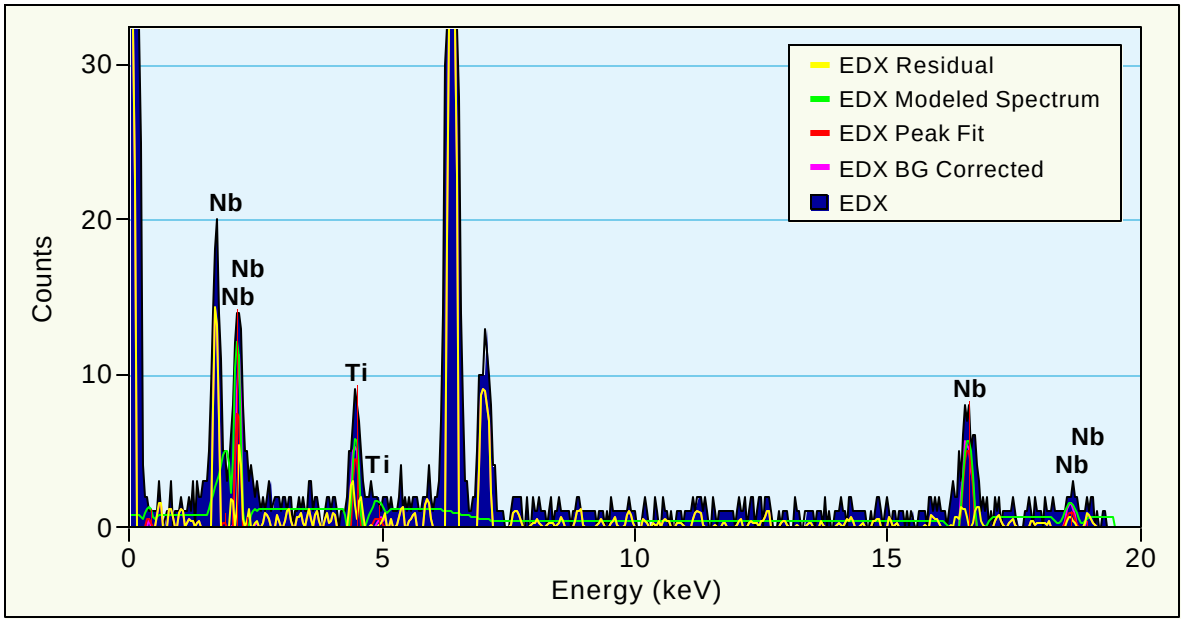

(a)

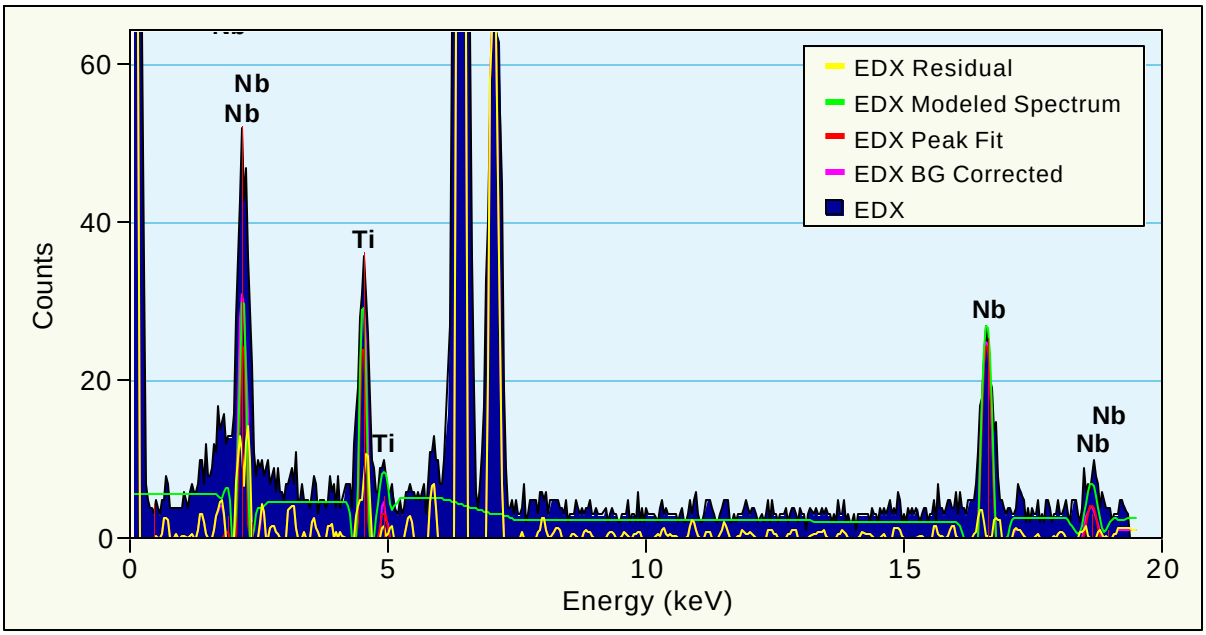

(b)

Figure 57 EDX spectra corresponding to (a) lower arm and (b) center locations of the star-like precipitate shown in Figure 56

5.3.3.2.2 Steel Conditions E and ET. The EDX measurements were made on arms and center as indicated in Figure 58 and Figure 60 for steels prior to and after the tunnel furnace, respectively. Their spectra are shown in Figure 59 and Figure 61 accordingly.

5.3.3.2.2.1 As-Cast Condition – Steel E

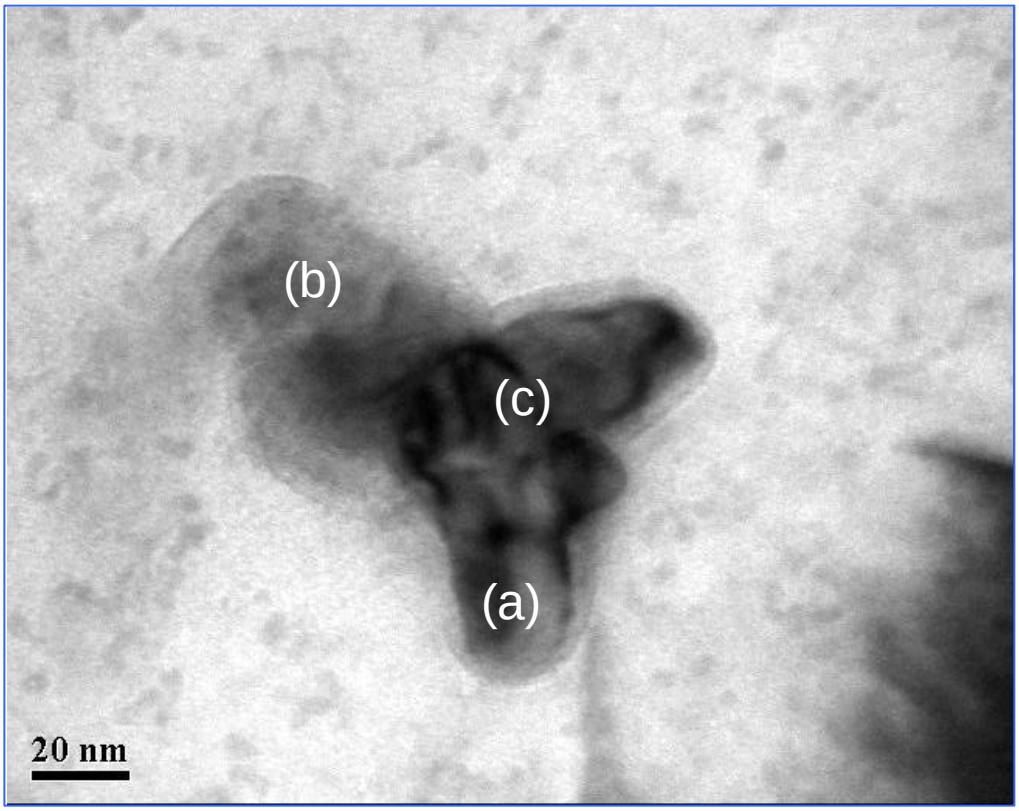

Figure 58 STEM micrograph showing the locations where EDX analysis was performed on a star-like precipitate from surface region of steel E, (a) lower arm, (b) upper arm and (c) center.

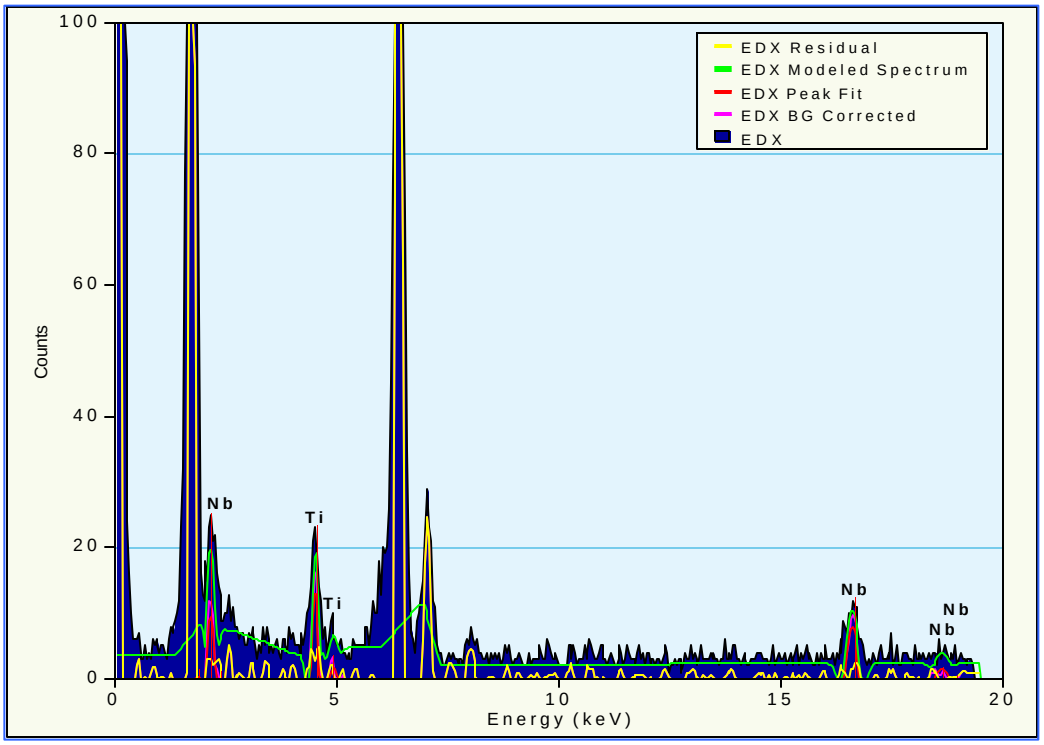
EDX Residual
EDX Modeled Spectrum
EDX Peak Fit
EDX BG Corrected
EDX
Counts
Energy (keV)
Nb
Ti
Ti
Nb
Nb
Nb
0
20
40
60
80
100
0
5
10
15
20

(a)

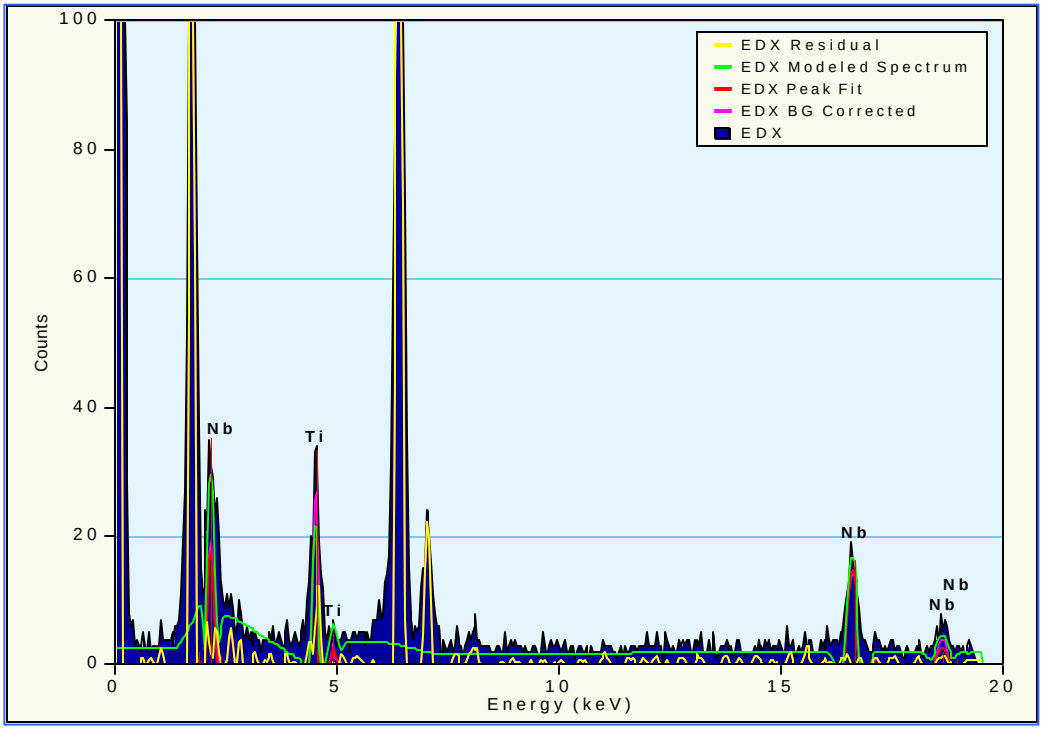
EDX Residual
EDX Modeled Spectrum
EDX Peak Fit
EDX BG Corrected
EDX
Counts
Energy (keV)
Nb
Ti
Ti
Nb
Nb
Nb
0
20
40
60
80
100
0
5
10
15
20

(b)

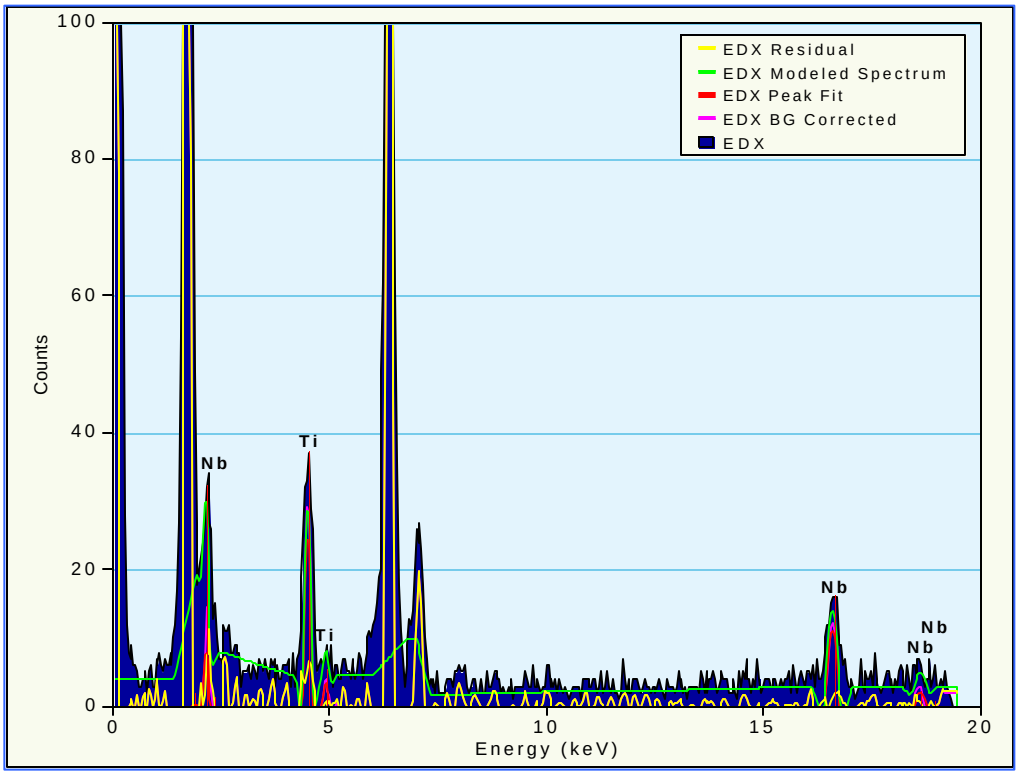

(c)

Figure 59 EDX spectra corresponding to (a) lower arm, (b) upper arm and (c) center locations of the star-like precipitate shown in Figure 58.

5.3.3.2.2.2 As-Equilibrated Condition – ET

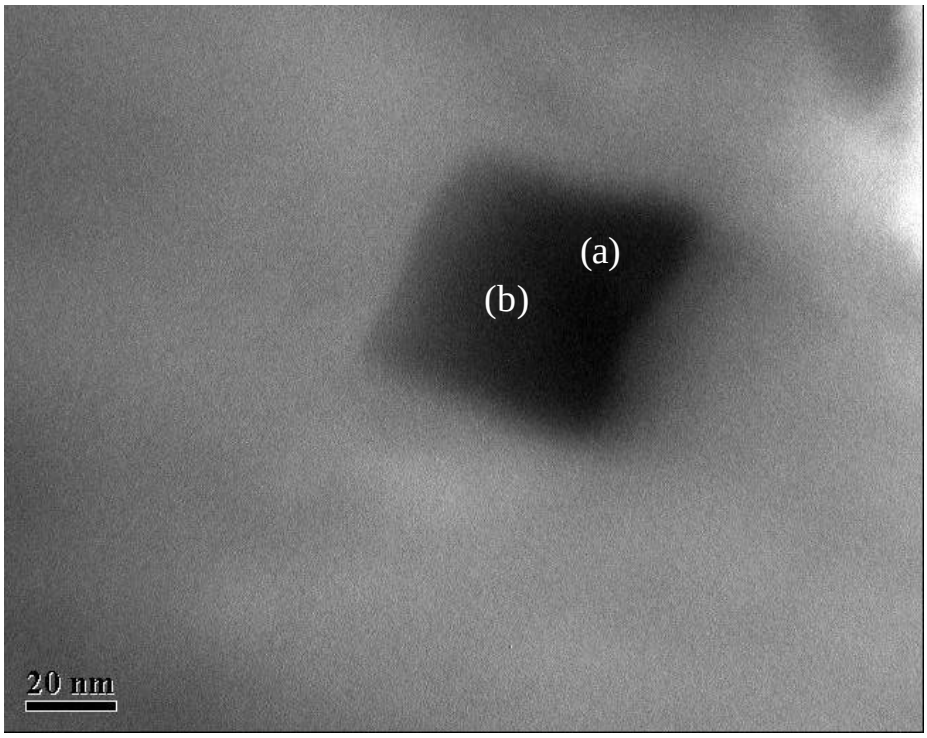

Figure 60 STEM micrograph showing the locations where EDX analysis was performed. (a) Right arm and (b) center of a star-like precipitate (from quarter point region of as-equilibrated steel ET)

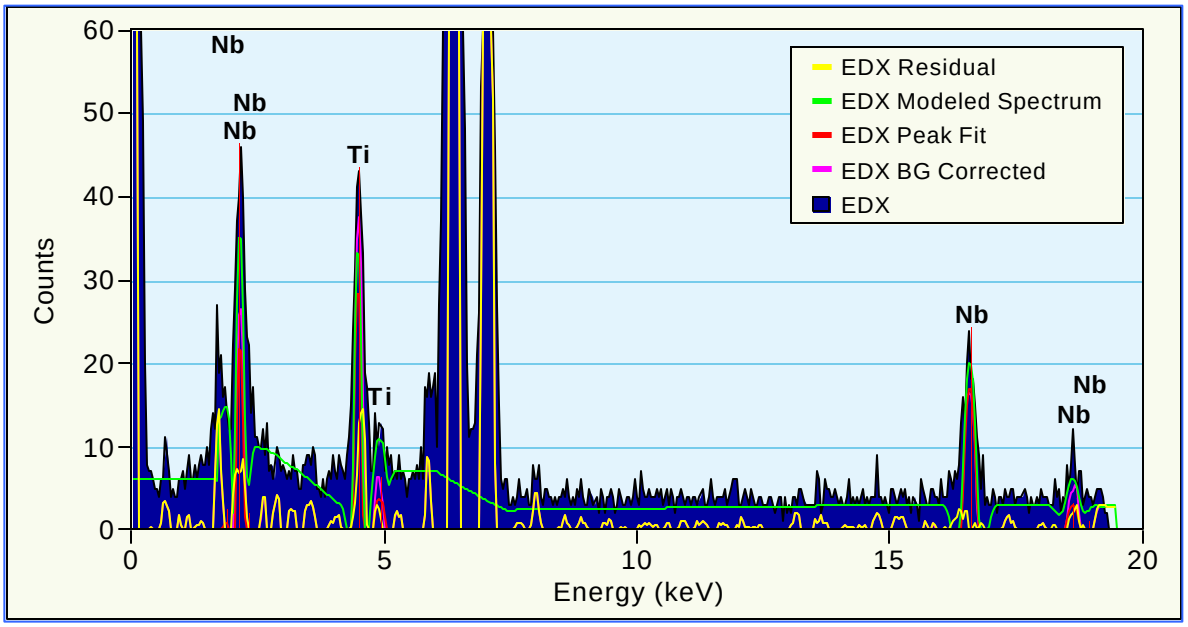

(a)

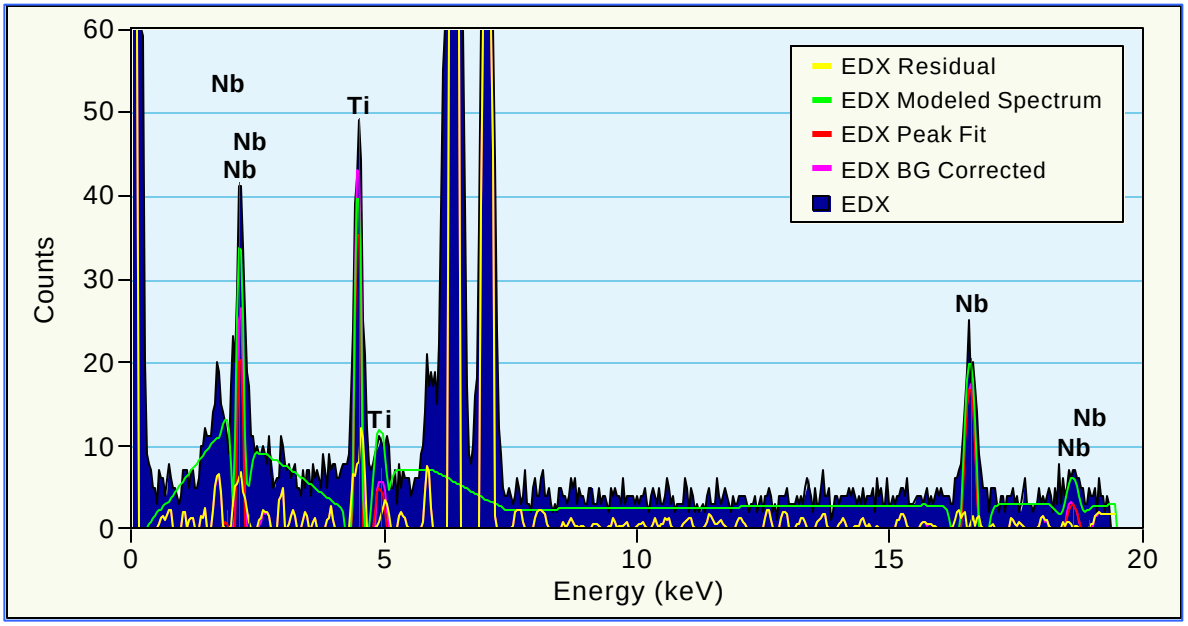

(b)

Figure 61 EDX spectra corresponding to (a) arm and (b) center locations of the star-like precipitate shown in Figure 61.

5.3.3.3 Kinetics of Formation of Complex (Ti, Nb)(C, N) Star-like Precipitates

5.3.3.3.1 Re-Melting Study. The re-melting experiments applied to steel E showed that when the steel is cast and cooled down to 1150 ºC, and water quenched to room temperature there is no evidence of complex (Ti, Nb)(C, N) star-like precipitates, even though the Nb and Ti contents are high.

The re-melting practice of steel E, which was cast and cooled down to 1050 ºC and water quenched to room temperature, now named steel EN, in deed, showed the beginning of the star-like precipitation - Figure 62. It can be observed that the arms (rich in Nb according to the EDX measurements) of what would be a star-like precipitate begin to grow from the core, which was Ti rich according to the EDX analysis. The Nb/(Nb + Ti) ratio of the particle depicted in Figure 62 ranged from 0.32 to 0.50.

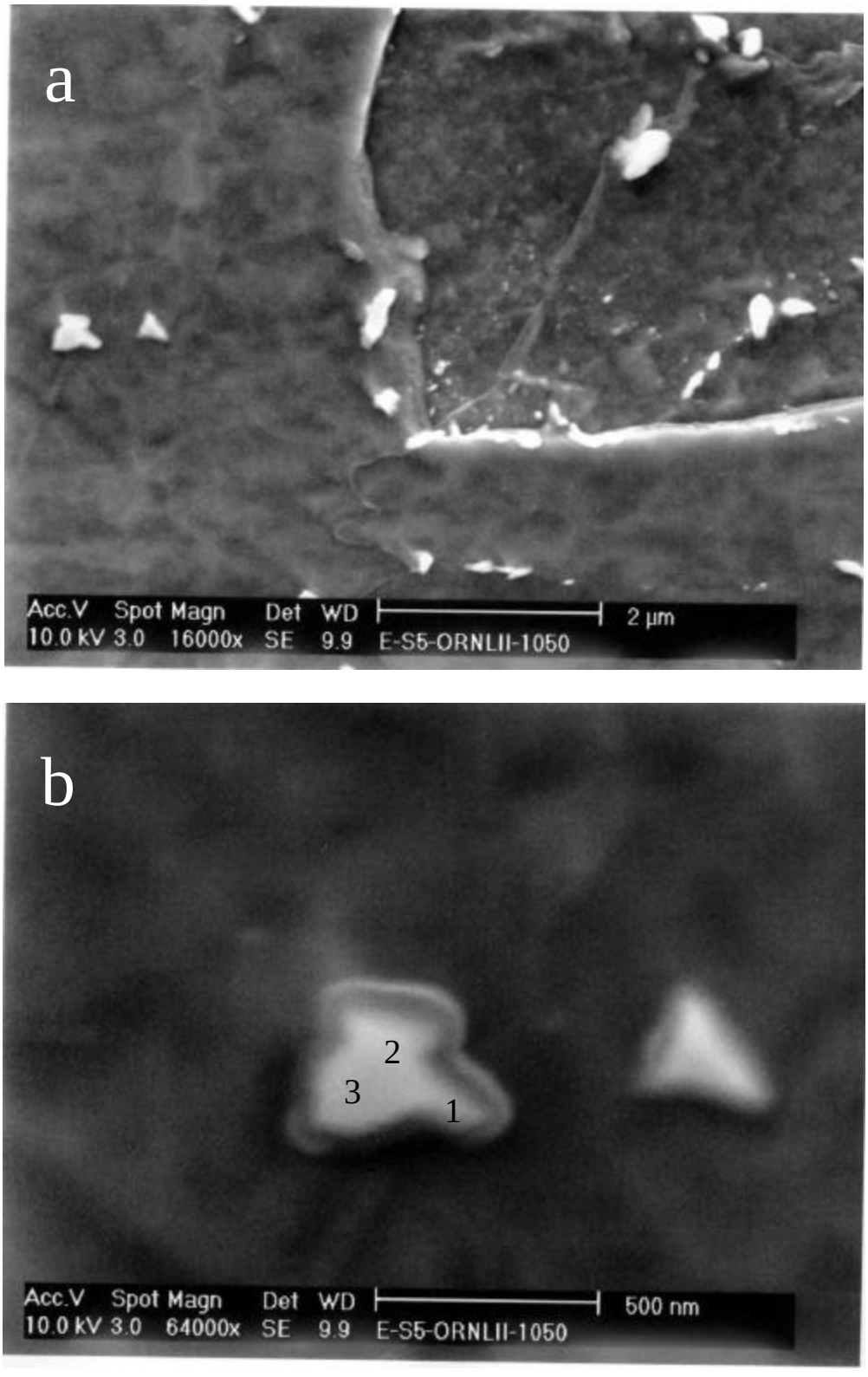

Figure 62 SEM micrographs of steel EML, showing (a) the beginning of star-like precipitates formation and (b) SEM-EDX locations for quantitative analysis.

5.3.3.3.2 CSP Thermal Simulation. Based on the results obtained in the re-melting practice, steel E (0.063% Nb, 0.04% Ti, and 0.069% C) was selected for this experiment. This experiment was carried out in the same research group by Y Ma[110] at the University of Pittsburgh and consisted in simulating the typical commercial CSP process rolling schedule, but without deformation in order to identify at what temperature the complex precipitates started to form. It is important to remark that it was a thermal simulation only. A typical CSP process rolling schedule can be found in Appendix 3 for reference. The experiment consisted in re-heating the steel to a temperature high enough to make sure the star-like precipitates were dissolved. After the reheating, the steel sample was mounted in the mechanical testing system (MTS) in which the cooling rate, which was varied (5 ºC/s, 10 ºC/s, and 20 ºC/s) for reproducibility purposes, could be controlled and finally water quenched the samples to room temperature.

The results showed the initiation of the formation of new star-like precipitates, in which NbC precipitated epitaxially on the already formed cuboidal TiN. The temperature at which these precipitates started to form was determined to be ~1090 ºC at a cooling rate of ~10 ºC/s. These results are consistent with the re-melting results.

6.0 DISCUSSION

This section is divided into 4 parts which refer to the major areas of analysis of the two steels (B and E) commercially produced by the CSP process. The first one refers to the microstructural characteristics of steels B, BT, E and ET including hardness measurements through the slab thickness; the second section refers to the segregation analysis; the third is about the precipitation behavior observed at different conditions of both steels B and E, which includes the kinetics of formation and dissolution of the major types of precipitates, and the fourth and last section refers to the quantitative analysis made on these precipitates, and the effect they may have in terms of the efficiency of Nb additions.

Other studies have been made on this type of material, but most of them are laboratory simulations of the process, hence, there are variations in compositions and processing conditions.

6.1 MICROSTRUCTURAL CHARACTERIZATION

The formation of non-polygonal ferrite was observed almost through the entire thickness of both as-cast steels. Some proeutectoid ferrite was observed, decorating the prior austenite grains, at the center location of the slab and in a lower amount at one of the surfaces of the slab which is believed to occur due to the efficiency of the cooling process, where the bottom surface is not as exposed to the cooling as is the top surface in addition to being exposed to temperature gradients with the environment, hence having an effect on the carbon diffusion and leading to the alteration of the microstructure on one of the surfaces. Furthermore, the cutting and quenching efficiency after the caster to obtain the material for the present study can have an added effect on the formation of a non-homogeneous microstructure.

Higher levels of polygonal ferrite were observed in the as-cast steels than those in the as-equilibrated conditions, which means that the equalizing treatment homogenized the microstructure to a great extent; a large part of the non-polygonal ferrite disappeared after being held in the tunnel furnace for 20 minutes - Figure 25 and Figure 26.

Although the equalizing treatment showed an effect on the microstructure homogenization, no effect of this treatment was observed on the prior austenite grain size. The results are shown in Table 5. They are smaller than the ones reported in the literature of up to ~1mm [29, 36, 38, 39], and they are in agreement with the ones reported by Sellars et al.[23], who reported D_γ of 500 – 600 μm. All of these are reported from

simulations of the direct charging process; therefore, there are variations regarding compositions and processing conditions.

R Kaspar and P Flub[100], in a laboratory simulation, proved that the finer the as-cast microstructure after the casting of a thin slab, the more homogeneous the micro segregation distribution by demonstrating the effect of the rate of solidification on the microstructure of a low-carbon microalloyed steel. The fact that the $D_?$ is coarse after casting means that the microstructure does not have a homogeneous microsegregation distribution, although, the prior austenitic grain sizes found in this work are smaller than the ones they reported in a later study. Also, the $D_?$ after the tunnel furnace looked very similar to that of as-cast steels, suggesting that the Nb content did not seem to have a very strong effect on controlling it. However, the standard deviation of steel with the higher Nb content, both before and after the tunnel furnace, is smaller than that of the steel with a lower Nb content.

6.1.1 Microhardness

As seen in Figure 27, the microhardness values are higher in as-cast steel E than in B, which was expected as steel E has a higher level of niobium than B. The higher levels of non-polygonal ferrite were thought to have an effect on the microhardness peaks shown at the quarter point locations on both as-cast materials, in order to verify if the variation in hardness values at the different locations through the thickness was significant. The statistical analysis (analysis of variance) was performed in three ways. For the first test, S1, QP2, C3, QP4 and S5 were considered, for the

second test, S1, QP2, and C3 were considered, and for the third test C3, QP4 and S5 were used – Appendix 1.

For significant variations, the statistical parameter Asymp. Sigma (AS) must show a value of less than 0.05 (the AS value corresponding to every test can be found on the third table of every test in Appendix 1). If the value is higher, the significance of the difference in microhardness is not of major importance.

In the first case, the (AS) showed a value of 0.175, meaning the variation is not significant. The same result was obtained for the second case, where only the first three locations through the thickness were considered. The AS was 0.557, even much higher than the first test. The third test, where the last three locations were considered, seemed to be the closest to 0.05, with an AS value of 0.066, which means that if the power had been higher, that is, if the number of measurements per point were increased, the variation in microhardness may be significant.

The microhardness values in the as-equilibrated samples were higher at one surface of the slab and decreased through the thickness direction as shown in Figure 27. This change in the overall microhardness behavior is more likely associated to the efficiency of the quench after reheating, hence affecting the resulting microstructure.

6.2 SEGREGATION ANALYSIS

As shown in Figure 28, section 5.2, the dendritic structure shows an increase in size and width from the surface and towards the center location of the slab as is characteristic of low carbon microalloyed steels.

6.2.1 Secondary Dendrite Arm Spacing (SDAS)

The secondary dendrite arm spacings (SDAS) also increase from surface to the center of the slab on both steels B and E used in this work – Figure 29. Steel B (low Nb – 0.035wt %) shows higher SDAS values than steel E (high Nb – 0.063wt %) especially at the surface and quarter point regions. The two fold difference at the surface, 100 to 200?m, and at the quarter point, 125 to 250?m, is attributed to the significantly higher cooling rate at the meniscus of the funnel-shaped casting mold used in thin slab casting. It is important to mention that both steels come from different sources and the processing parameters may be different. This difference can also result from the higher Nb and Ti content of steel E having an effect on the width and size of dendrites, and causing the decrease in SDAS.

The SDAS in steel B are comparable to those reported by G Flemming et al. [55] of a conventionally produced 230 mm thick slab. The surface and quarter point locations are similar, steel B shows higher values, which suggests that either the cooling rate of B was much slower or, more likely, the effect of microalloying elements such as Nb and Ti

had an effect on controlling the initial solidification structure in Flemming's study. The center of the thick slab shows higher values as in the regular case.

In contrast to these results, Engl et al. [56], reported SDAS from about 50 µm at the edge of the slab to about 160 µm at the center. This study was a simulation of the TSC and Rolling process at the Thyssen Krupp Stahl AG in Germany. Flemming's study on a 50 mm slab (from SMS)[55], reported from a laboratory test carried out at Buschhutten pilot plant, SDAS from 50 µm at the surface, 75 µm at the quarter point and 125 µm at the center of the slab supporting Engl's results. The fact that these tests are based on simulations may lead to finer SDAS by applying faster and controlled cooling rates, which is not as easy in the regular TSC process. An example of this is the study by Sellars et al.[23], who reported SDAS from 24 µm at the edge to 32 µm at the center by using cooling rates as low as 1 K/s and a different chemistry for the simulation by substituting the C-Mn steel for a Fe-30Ni alloy.

6.2.2 Microsegregation Analysis

The result of the rapid solidification may be less chemical segregation and a more homogeneous microstructure. An EDX linescan analysis was performed on both steels in order to look for solute segregation in the interdendritic regions. High amounts of precipitates were found in the interdendritic regions compared to the dendritic regions due to segregation. Precipitates in both steels showed three types: 1) Complex (Ti, Nb,) (C, N) with a star-like shape, most of them large in size. 2) Cuboidal TiN, and 3) some small spherical NbC precipitation. These precipitates showed general interdendritic

distributions. They were arranged in rows or random in the matrix, in some cases, they even precipitated in bands. These characteristics suggested a high degree of segregation occurring in those zones. Steel E, whose Nb and Ti levels are higher than those in B, showed higher volume fractions of these precipitates. As seen in Figures 32 and 33, EDX line scans across the interdendritic precipitate rows were performed. The segregation is shown in terms of the intensity of Nb and Ti. It is observed that as the line scan detector crosses the row of precipitates, an increase in intensity occurs, which explains the enrichment of solute in those regions during solidification. Mathematical modeling software, JMat-Pro®, was used to calculate the distribution coefficients of Nb and Ti, and the segregation enrichment factors based on the initial concentrations and the fractions in the solidus and the liquidus after the solidification. The JMat-Pro® calculations for the distribution coefficients, and segregation factors are based on the Scheil-Gulliver solidification equations. L Kuchar[101 102] defined K_o as the isothermal proportion of the admixture concentration on the solidus curve X_M^S, to the concentration on the liquidus curve X_M^L in a binary diagram metal-admixture.

$$Ko\ ?\ Fe_{Nb} \quad and \quad Ko\ ?\ Fe_{Ti}$$

Where,

$$Ko\ ?\ \frac{X_M^S}{X_M^L}$$

C is the concentration or fraction of the metal in the solidus and in the liquidus, respectively, after the solidification.

The calculated thermodynamic distribution coefficient of Nb in d-Fe is K=0.24 with a segregation enrichment factor of ~4.3, whereas for Ti in d-Fe, K=0.25 with a segregation enrichment factor of ~3.9. The segregation enrichment factor of Nb in Fe is in good agreement with the one reported by L Kuchar[95] of 3.75, whereas for Ti in Fe, A Kothe et al.[96] reported a segregation factor of 3. In both cases the values are higher; the first one may be due to the model equations they based their calculations on (Brody and Flemings Model), and the second may have been due to the fact that the segregation factors were experimentally calculated from simulation test results; however, higher Ti enrichment segregation factors with values of up to 9 were reported in the same study. These were measured at spots where 3 or more microsegregation zones met.

The next step was the verification of microsegregation across the entire interdendritic regions on both steels B and E. Figure 34, Figure 37 and Figure 38 reveal the existence of microsegregation, shown in terms of the solute intensity peaks, which stand out as the line scan crosses the interdendritic pool and reaches lower intensity values as it approaches the dendrite arm.

For the verification of this behavior, one of the steels (steel E) was selected to be austenitized to 1300 ºC for 3 minutes, in order to confirm that as the material is exposed to higher temperatures, a homogenization of the initial segregation that took place during solidification could be achieved. The steel called EA (austenitized) was then especially etched to reveal the dendritic structure. The observations resulted, as depicted on Figures 35 and 36, from the structure homogenization by showing a lower

and more uniform solute intensity (below the average shown by steel E) across one of the interdendritic regions analyzed by SEM-EDX line scan.

6.3 PRECIPITATION ANALYSIS

It is important to mention that precipitation hardening was not considered in this study, but rather, precipitation for microstructure control.

It is known that the additions of microalloying elements (MAE) such as Nb, Ti, and V and interstitial elements such as N and C help to improve the mechanical properties of HSLA steels by having a strong impact on the microstructure evolution throughout the process and up to the final product. This occurs as a result of the combination of both alloying and interstitial elements bringing about the formation of different types of precipitates. See section 5.3.1.

The precipitation results in both steels were found to be strongly influenced by the local enrichment of microalloying elements resulting from interdendritic segregation. This is supported by the results found by S V Subramanian and G C Weatherly[103], who studied the degree of heterogeneity in the size and dispersion of precipitates and the microchemistry of meta-stable precipitates in a Ti-Nb microalloyed steel. Also, C Zhou and R Priestner[28], and Engl et al.[56], stated that increasing the solute above a critical level, hence over passing a certain level of supersaturation, would lead to interdendritic precipitation of carbo-nitrides.

For comparison purposes, a complete description of the quantitative measurements results of all steels conditions consult Table 8, at the end of this section.

6.3.1 As-Cast and As-Equilibrated Conditions

In the present work, the formation of cuboidal TiN precipitates was observed in both as-cast and as-equilibrated steels. It was found that these precipitates are interdendritic since they form at high temperatures during solidification. These precipitates were also observed by R Priestner et al.[28] in steels containing similar levels of Ti to steel E.

The volume fraction of these precipitates was higher in steel E, 1.43 $x10^{-5}$, as a result of its high Ti content (0.04 wt %) and the levels of segregation in the interdendritic zones, as compared to the lower volume fraction of this type of precipitates, 1 x 10^{-6}, in steel B, whose original titanium content was ten times less. It was found that in steel ET, after the tunnel furnace, that the TiN size was not affected by the equilibrating treatment, where it was held for 20 minutes, due to its stability at high temperatures, according to T Gladman[104], the studies of the solubility of TiN have indicated that of all the microalloy carbides and nitrides, TiN is the most stable. TiN precipitates do not seem to grow or dissolve during or after the equalizing heat treatment. Various dissolution temperatures of TiN in liquid and in austenite for comparison purposes are shown in Figure 63. The TiN precipitates in steel BT showed a decrease in size due to the dissolution of the NbC, which precipitated epitaxially on the cuboidal TiN - Figure 40 and Figure 46. The dissolution temperature of NbC, shown

in Figure 64 was calculated in terms of the solubility of NbC in austenite by two authors for comparison purposes.

While most studies agree with the size and distribution of TiN precipitates, only a few refer to the presence of the complex star-like or cruciform (Ti, Nb)(C, N) or (Ti, Nb, V)(C, N) precipitates before the equilibrating heat treatment[28, 29, 30] and other more recent studies[105, 106].

Star-like precipitates were observed in as-cast steels, E (0.063% Nb) and B (0.035% Nb) - Figure 42, Figure 43 and Figure 44. The volume fraction of star-like precipitates was much higher in steel E than in B, 0.062%, and 0.009%, respectively, which is a reflection of the steels compositions. Their morphology is associated with the epitaxial precipitation of NbC over the TiN previously formed as it was also predicted by S V Subramanian et al.[103]. Also, based on the mutual solubility shown by nitride-forming microalloying elements such as titanium, niobium and vanadium, they may form complex carbo-nitrides and may exist as a single constituent phase[107]. Star-like precipitates in the lower Nb content steel showed smaller sizes and looked more symmetrical than those of steel E. This could be related to the NbC precipitated epitaxially on the TiN precipitates - Figure 41. Since steel E had much higher Nb and Ti contents, the arms of the star-like precipitate would grow larger on a larger TiN precipitate (core) and not as well defined as those in steel B. This can be explained in terms of the difference in atomic ratios Nb/(Nb + Ti) calculated between the arms and center of precipitates in both as-cast and as-equilibrated steels. The atomic ratios are reported in Table 6 and for further comparison with other steels conditions in Table 8. Figure 65 for steel E (all conditions) and Figure 66 for steel B (all conditions including

hot band observations) show the atomic ratios plotted as a function of the position on the precipitate from all the conditions. The procedure to obtain such information is described in section 5.3.3.2.

In steel E, the Nb/(Nb + Ti) measured ratio was 0.056 – 0.067 at the center and arm positions on the precipitate respectively; meaning that the arms of the precipitates were not as rich in Ti as was the center of the precipitate, the arms show a higher ratio which meant they were Nb rich. In the as-equilibrated condition (ET), where the precipitates were partially dissolved, the atomic ratio measured in the arms showed a decrease, from 0.67 (as-cast-E) to 0.61 and a slight increase in the center, from 0.056 (as-cast -E) to 0.575, explaining the partial dissolution of NbC (arms) during the heat treatment in the equilibrating furnace for 20 minutes and the exposure of the TiN core as this occurs. A similar type of behavior was observed in steel B and BT. The ratios measured ranged from 0.66 in the center up to 0.78 in the arms, which explains the absence of Ti, and the probable enrichment of Nb after the equilibrating treatment, where the average size of the precipitates decreases from 66 to 39 nm. Some small TiN precipitates were observed as the NbC arms dissolve during the equilibrating treatment and after reheating treatments to higher temperatures as seen on steel E. The volume fraction of star-like precipitates in steel ET was still higher than that of BT, 0.0083% and 0.0018%, respectively, after the 20 minutes holding time in the tunnel/equilibrating furnace at an approximate temperature of 1150 ºC-Table 8.

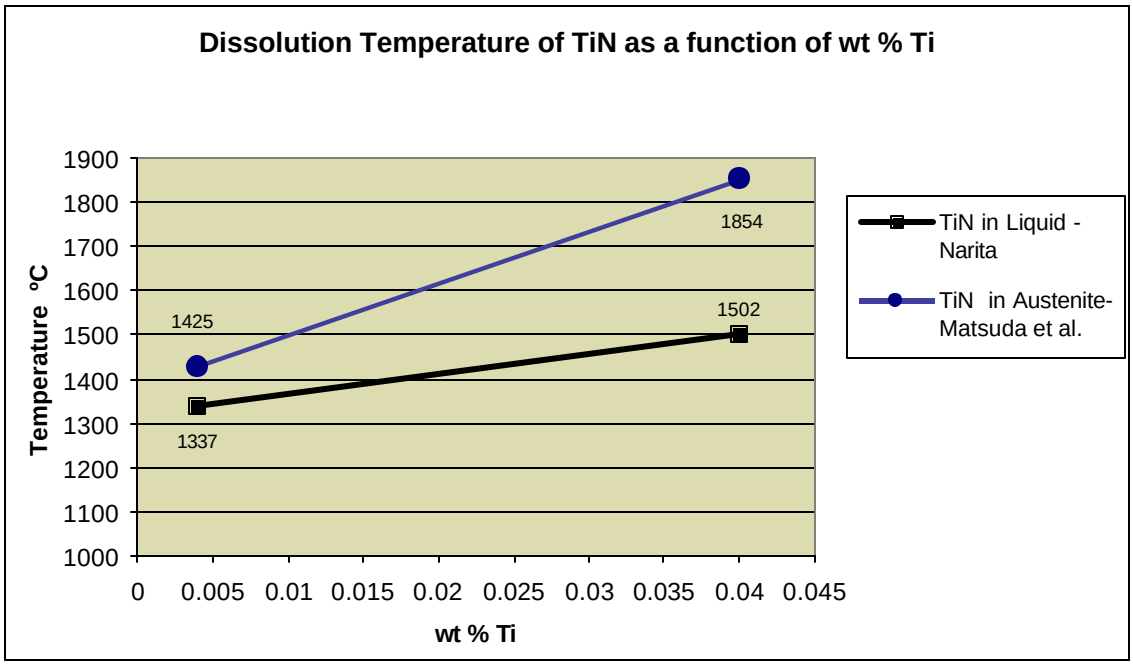

Figure 63 Dissolution temperature (ºC) of TiN based on titanium content – Two different solubility product conditions: Narita[81] and Matsuda et al.[85]

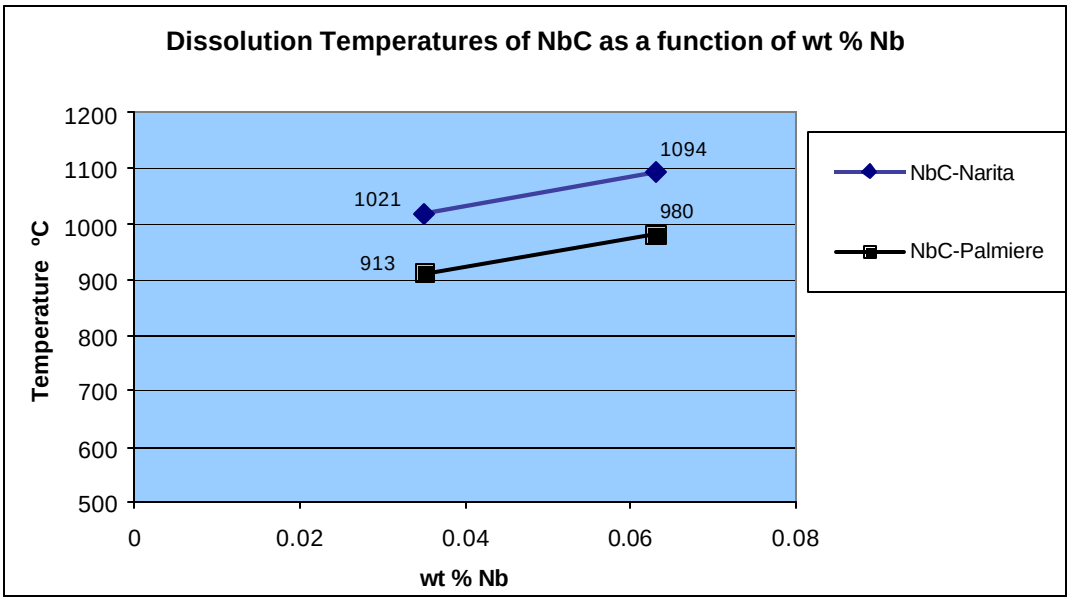

Figure 64 Dissolution temperature (ºC) of NbC based on niobium content – Two different solubility product calculations: Narita[81] and Palmiere[58]

6.3.2 Kinetics of Dissolution and Formation of Star-Like Precipitates

These complex star-like precipitates (Ti, Nb)(C, N) dissolve as the temperature is progressively increased and, according to M Prykril et al. [30], although in a different system (Ti, V, Nb microalloyed steel), if the holding time is prolonged, in addition to the complex carbo-nitride progressive dissolution, there is titanium enrichment.

6.3.2.1 As-Reheated Conditions – BR1, ER1 (1175 ºC – 20 mins.) and BR2, ER2, (1200 ºC – 20 mins.)

The increase in temperature in the equilibrating stage of the process led to complex precipitates dissolution, however, the NbC arms of star-like precipitates in steel ER1 seemed to reach a dissolution limit. The precipitates average size decreased from 55 nm (as-equilibrated-ET) to 50.5 nm (as-reheated to 1175 ºC-ER1). Although the numbers seem to be fairly constant, the volume fraction in the ER1 condition, 0.00316%, and was still lower than that of the ET condition, but only by a factor of 2.6.

The Nb/(Nb + Ti) ratio in the center decreased slightly, from 0.575 (ET) to 0.54 (ER1), which means there was a gain of Nb, and remained constant in the almost completely dissolved arms, 0.61, most likely due to the almost complete dissolution of NbC after being held in the equalizing furnace for 20 minutes at a temperature as high as 1175 ºC.

In the lower Nb and Ti content steel, the precipitate size decreased from 39 nm (as-equilibrated-BT) to 13 nm (as-reheated-BR1). The volume fraction decreased from 0.0018% in the BT condition to 0.00023% in the BR1 condition. Their atomic ratios were 0.54 – 0.61 and 0.68 – 0.78, respectively. This meant that there was an enrichment of Nb, which is somewhat similar to what was observed in steel ER1, although not as clear, due to the presence of TiN precipitates as a result of the higher Ti content.

In the second case of as-reheated condition, steels ER2 and BR2, the same complete analysis as with the previous conditions could not be made. It was observed that the precipitate average size decreased slightly by only 2.5 nm, from 50.5 nm (ER1) to 48 nm (ER2) after being reheated at a temperature as high as 1200 ºC for 20

minutes. The measured volume fraction of steel ER2 was, 0.00183%, decreasing even more, as expected, but only by a factor of 1.7 as compared to the factor of 2.6 between the ER1 and ET conditions, and a factor of 7.4 between the ET and E conditions.

Only a few TiN precipitates were observed in condition BR2, the size of some of the few precipitates found, ranged from 20 to 100 ?m as a result of the dissolution of the NbC that had precipitated epitaxially on the TiN. Star-like precipitates in the BR2 condition were completely dissolved; therefore, no information could be obtained about this kind of precipitation.

The increase in atomic ratios observed in the as-reheated conditions of both steels (ER1 and BR1) may lead to a re-precipitation of NbC and even growth and coarsening of complex precipitates at longer equalizing holding times[28, 30, 105] or during the rolling process[29].

Table 8 Quantitative and chemical analysis results of star-like precipitates prior to and after the tunnel furnace including reheated conditions and hot band

Steels	Average precipitate size (nm)	Volume Fraction (%)	Precipitate composition		Location
			Precipitate type	Nb/(Nb+Ti) (mol/mol) Core - Arm	
E	113	0.062	(Ti, Nb) (C, N)	0.56 – 0.67	Interdendritic regions and random in matrix
ET	55	0.0083	(Ti, Nb) (C, N)	0.57 - 0.61	random in matrix
ER1	50	0.00316	(Ti, Nb) (C, N) Partially dissolved	0.54 - 0.61	random in matrix
B	66	0.009	(Ti, Nb) (C, N)	0.66 - 0.74	Interdendritic regions and random in matrix
BT	39	0.0018	(Ti, Nb) (C, N)	0.68-0.78	random in matrix
BR1	13	0.00023	(Ti, Nb) (C, N) Partially dissolved	0.60 – 0.70	random in matrix
Hot Band-E	150	0.060	(Ti, Nb) (C, N)	0.68 – 0.72	random in matrix

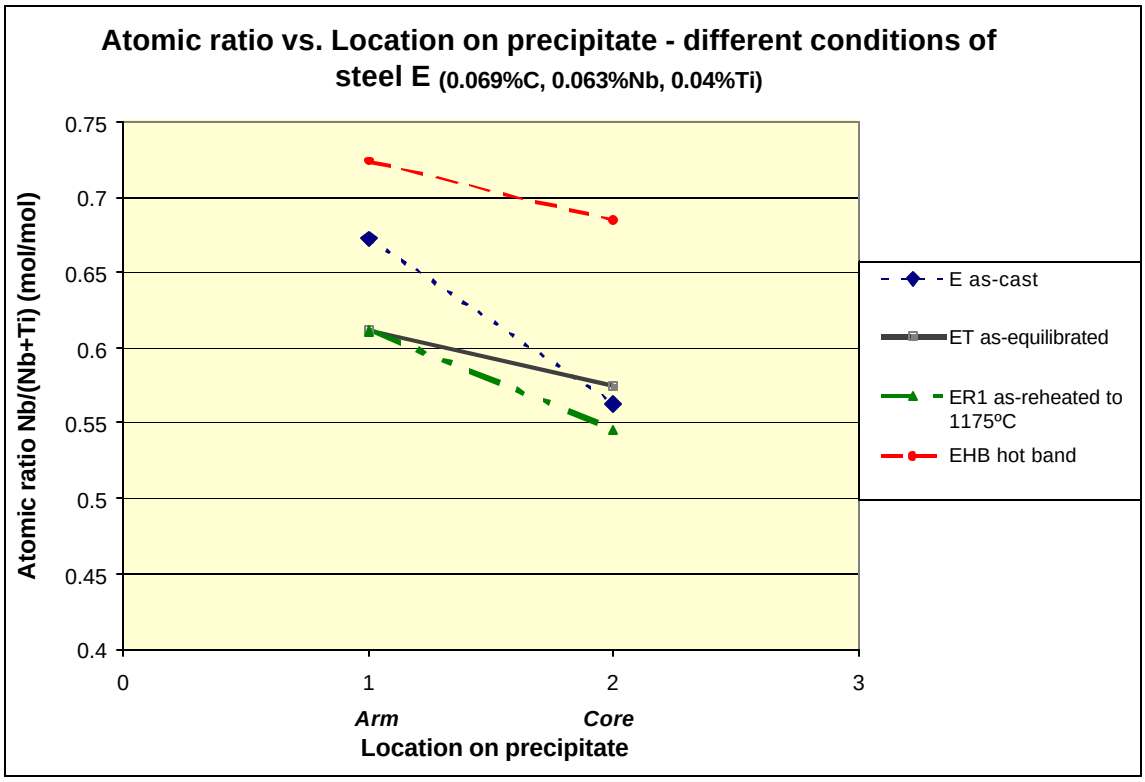

Figure 65 Nb-Ti content distribution in star-like precipitates from different conditions of steel E, including EHB -hot band for comparison purposes

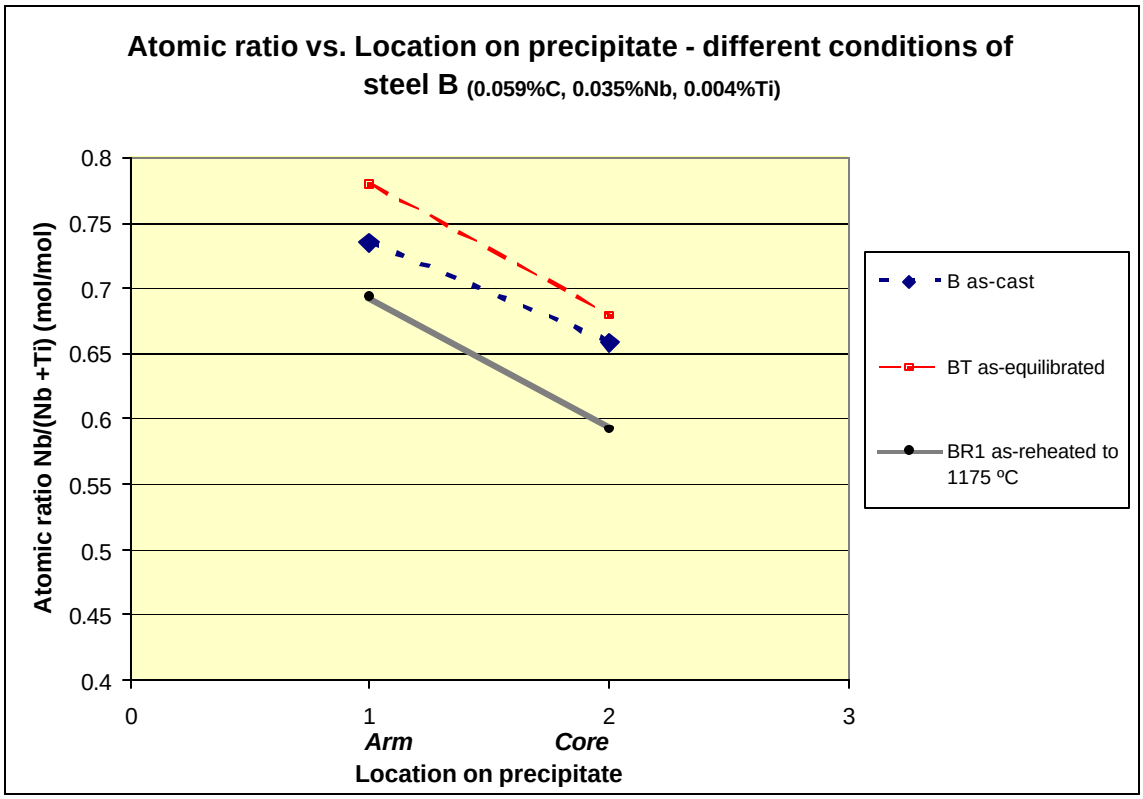

Figure 66 Nb -Ti content distribution in star-like precipitates from different conditions of steel B

6.3.2.2 Kinetics of Formation

The results of the re-melting analysis, when cooling down to two different temperatures, (1150 ºC and 1050 ºC) followed by water-quenching to room temperature, suggested the beginning of the formation of star-like precipitates takes place at a temperature in between the two temperatures used for this practice. Based on this, Y Ma carried out the thermal simulation at different cooling rates, cooling down to different temperatures paying especial attention to the temperature range between 1150 ºC and 1050 ºC. The determined start or critical temperature at which these precipitates formed

was approximately 1090 ºC at a cooling rate of ~9 ºC/sec. Meaning that, the formation of such complex star-like precipitates in the industrial practice occurs before the slab enters the equalizing furnace, reaching temperatures as low as 1000 ºC.

6.4 QUANTITATIVE ANALYSIS

This section refers to the chemical analysis performed on one of the steels (as-cast steel E). The analysis was performed at a research institute in China (CISRI). Also, based on the Nb/(Nb + Ti) ratios measured in the present study, a mass balance was made in order to see how much of the Nb is consumed for the formation of the complex (Ti, Nb)(C, N) star-like precipitates and how much is still available in solution for further processing. Results are compared to steel EHB, named after the hot band condition of steel E. The analysis of this steel condition was performed by R Wang[108] in the same research group (BAMPRI) at the University of Pittsburgh.

6.4.1 Chemical Analysis and Mass Balance

The chemical analysis showed that the total amount of precipitate phase in the form of $M(C_x, N_y)$(wt %) constituted 0.114 wt% in steel E. Star-like precipitates represented the 48 %, which contained Ti, Nb, C and N and constituted 0.055 wt% of

the total amount of precipitate phase. C and N constitute 15.8%, whereas Ti and Nb represented 84.2% of the total.

By multiplying the 84.2 % times the calculated volume fraction of complex star-like precipitates in as-cast steel E, 0.0618 %, the total amount of Ti and Nb in the star-like precipitates was obtained. Taking into account the Nb/(Nb + Ti) average ratio measured for this condition, which was 0.753, times 0.00052, which is the total amount of Ti and Nb in the star-like precipitates, resulted in a value of 0.039 wt % of Nb, and a 0.013 wt % of Ti, representing the approximate amounts of Nb and Ti, respectively, consumed in the formation of these complex precipitates.

It was assumed that the volume fraction of NbC is equal to the mass fraction of the same by a factor of 1.0092[109]:

$$fv_{(NbC)} = 1.0092 \times W_{(NbC)}$$

Where,

fv = Volume Fraction

W – Weight

This means there was an approximate amount of 0.024 wt % of Nb in solution for further processing.

Taking these calculations as a reference, the approximate wt% of Nb tied up in star-like precipitates was calculated for the ET and ER1 conditions. The results are shown in Figure 67.

Other analyses for the Nb distribution in steel EHB conducted at CISRI showed that the 0.0378 wt% of Nb was in star-like precipitates, the 0.0172 wt% was held in other precipitates and 0.0075 wt% was still in solid solution, which corresponded to a 60%, 27.5% and 12% of the total Nb content in steel E, respectively.

It is clearly observed that the amount of Nb dissolved after the equalizing treatment is high, and even higher dissolution levels are reached when the steel is exposed to higher heating temperatures. Interestingly enough, this Nb that was expectedly dissolved, is unexpectedly drawn back from the matrix to form the same type of precipitates and even a very similar volume fraction as it can be observed in Figure 67, suggesting that the formation of complex carbo-nitride star-like precipitates takes place either between the equalizing furnace and the rolling mill or during the rolling process. Therefore, it is required to control the temperature at which the slab enters the hot rolling mill or the time it takes to go inside the milling train in order to avoid the formation of these complex (Nb, Ti)(C, N) star-like precipitates which consume the Nb at a greater extent than expected.

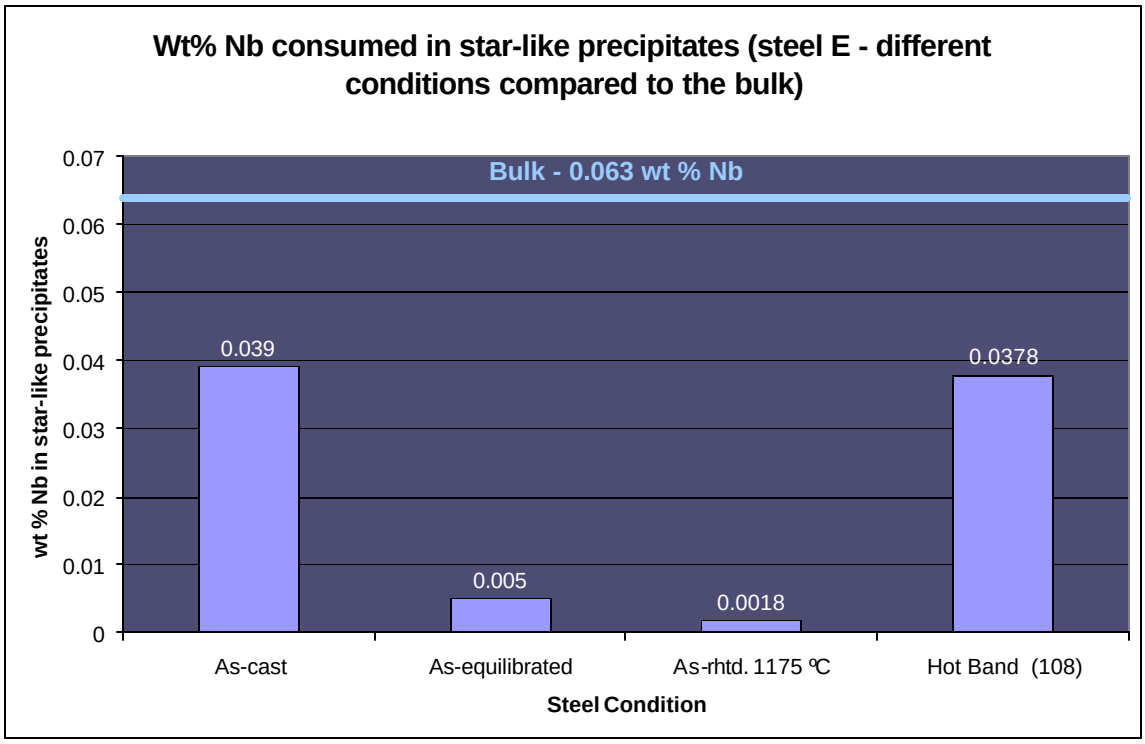

Figure 67 Weight percent of Nb consumed in the formation of complex (Nb, Ti)(C, N) precipitates with a star-like morphology as a function of the different conditions of steel E including the wt % Nb from the hot band stage (EHB) [108].

7.0 CONCLUSIONS

The equalizing heat treatment seemed to have a good effect on the homogenization of the microstructure since the high levels of non-polygonal ferrite observed in the as-cast structure decreased with the equilibrating heat treatment resulting in a more homogeneous microstructure.

The VHN microhardness peaks observed at the quarter points through the thickness of the as-cast slabs showed no sign of macrosegregation at those specific regions.

The fact that the microhardness in the as-equilibrated condition showed higher values at one of the surfaces and decreased through the thickness direction was attributed to the quenching efficiency after the sample was cropped from the slab for investigation, resulting in a microstructural inhomogeneity.

Even though the D? values ranged from 635 to 750 ?m, they were not as large as the ones reported in the literature of 1mm in average (from laboratory simulations of the TSC process), it could be suggested that the microstructure of the steels studied in this work would be more homogeneous, based on the fact that a finer cast structure after thin slab casting brings about a more homogeneous microstructure.

There is no significant effect of alloying elements such as Ti in controlling the prior austenitic grain size D?

Segregation of microalloying elements during solidification was observed reflected in the high degree of interdendritic precipitation.

The D? nucleation occurs at the d/d boundaries and its growth is controlled by the SDAS and the presence of TiN. Microalloying elements apparently did not precipitate as TiN interdendritically at the d/d boundaries; hence the growth control of D? is not observed.

As the SDAS of steel E is not as large as that of steel B, we suggest that the first steel underwent a more effective quenching treatment, since higher cooling rates lead to more homogeneous distribution of microsegregation.

Although the effect of TiN was not clearly observed, the prior austenitic grain size is smaller in E than in B, which suggested that the higher Ti content steel may have had some effect in controlling D?.

Two major types of precipitates, were observed in the as-cast condition: cuboidal TiN and complex (Ti, Nb)(C, N) star-like precipitates, which had a K-S relationship to the matrix,. Also but not significantly, small spherical NbC and needle-shaped precipitates were observed.

The formation of star-like precipitates occurs at an temperature of 1090 ºC.

Star-like precipitates undergo several changes after the equalizing treatment: they reduce in size and lose their initial symmetry.

During the equalizing treatment there is not a complete precipitate dissolution.

When the steels are exposed to higher temperatures than the typical equilibrating temperature of 1150 ºC, the arms of star-like precipitates seem to progressively dissolve until the TiN core is reached.

Although the equalizing temperature treatment appeared to have dissolved part of the NbC, the fact that it is put back in solution and stays there for subsequent processing depends very much on the diffusion coefficient of Nb and C, and the speed at which the slab is charged in to the hot rolling mill. The reason for this is that as the temperature decreases, the formation of the complex star-like precipitates may take place again consuming a high amount of the available Nb.

It was observed that the volume fraction of star-like precipitates was the same in both as-cast and the hot band conditions of steel E. This suggested that the temperature at which the slab was charged in to the rolling mill went below the critical temperature for the formation of star-like precipitates, resulting in the re-precipitation of NbC in the form of complex (Nb, Ti)(C, N) star-like precipitates epitaxially on the undissolved TiN.

Based on the mass balance the amount of Nb consumed in the formation of star-like precipitates is approximately the 60% of the initial concentration, which can also be observed in the hot band condition.

The amount of Ti and N in HSLA steels produced by the CSP process has to be optimized with the purpose of either avoiding or reducing the formation of star-like precipitates.

Control the slab temperature (over 1090 ºC) through the casting, equalizing and rolling treatments, in order to avoid the formation of star-like precipitates.

The CSP practice does not utilize Nb very efficiently.

APPENDIX 1

SPSS (STATISTICAL ANALYSIS SOFTWARE)

Proficiency with statistical software packages is indispensable today for serious research in the sciences. SPSS (Statistical Package for the Social Sciences) is one of the most widely available and powerful statistical software packages. It covers a broad range of statistical procedures that allow you to summarize data (e.g., compute means and standard deviations), determine whether there are significant differences between groups (e.g., t-tests, **analysis of variance**), examine relationships among variables (e.g., correlation, multiple regression), and graph results (e.g., bar charts, line graphs).

SPSS software was the software used for the analysis of variance in microhardness explained in section 4.2.1.

Analysis of variance (ANOVA) spreadsheet is only used when the samples (statistical samples) follow a normal distribution or Gauss shape / Bell-shape curve. For this or other analysis of variance, e. g. the t-tests, the analysis can be performed, but the power (number of samples/measurements) has to be very high, usually more than 30 per point.

When measuring microhardness (VHN), sometimes it is not possible to achieve such amount due to the sample dimensions or the required separation between each of

the measurements. In the case of the steels tested for VHN measurements in this work, neither of the requirements mentioned above was met.

Steels B and E showed an increase in hardness at the quarter point regions through the thickness of the slab. To statistically verify the significance of the hardness variations at those points, the use of a non-parametric test was required, that means a test where the number of tests or the power is not a rigorous requirement. Although, as it is the case in every statistical analysis, the higher the power, the more representative and reliable the analysis results.

Steel B VHN microhardness curve was selected for the analysis since it was the one that showed a more outstanding variation in hardness among the different locations through the thickness, namely, S1, QP2, C3, QP4, and S5. See Figure 68.

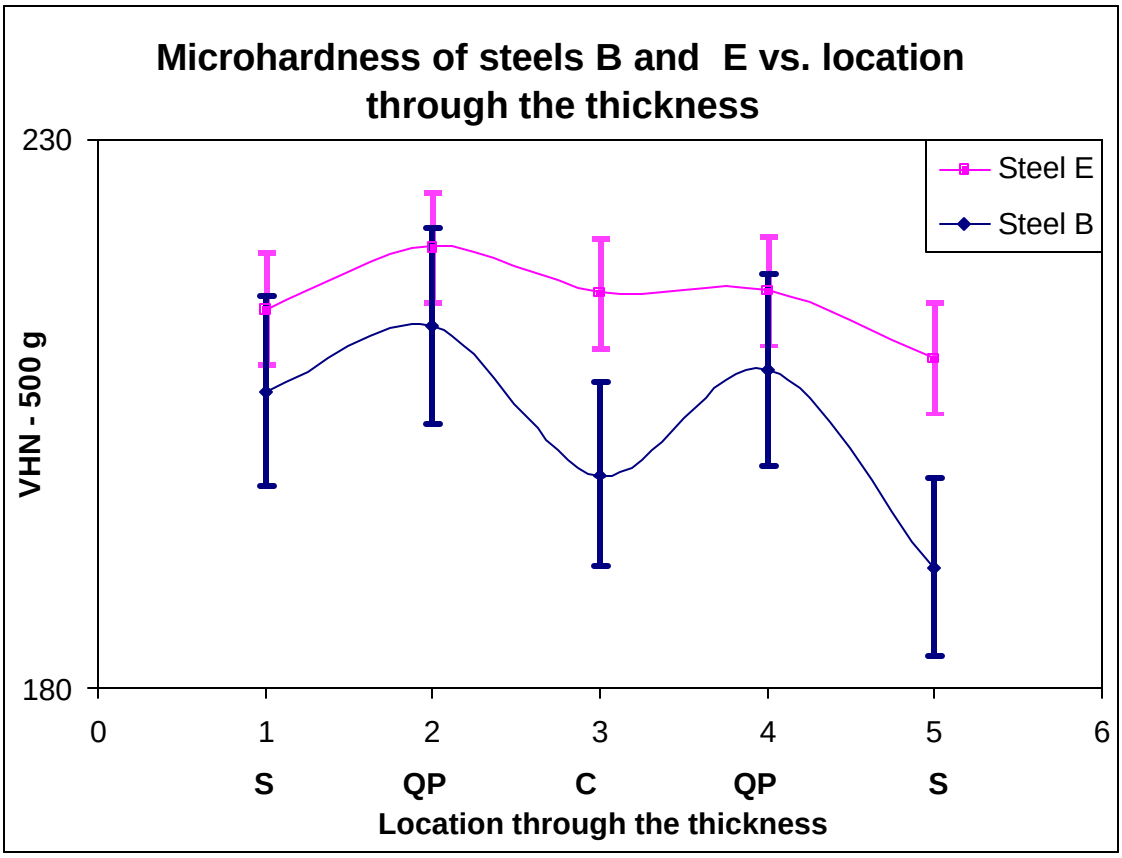

Figure 68 Microhardness of as-cast steels B and E as a function of location through the slab thickness. Steel B (lower curve) was selected for statistical analysis.

Firstly, the SPSS analysis was performed on the five locations, S1, QP2, C3, QP4 and S5 using the non-parametric test Kruskal-Wallis. The results were as follows:

```
NPAR TESTS
  /K-W=measure   BY site (1 5)
  /STATISTICS DESCRIPTIVES
  /MISSING ANALYSIS.
```

NPar Tests

Descriptive Statistics

	N	Mean	Std. Deviation	Minimum	Maximum
MEASURE	30	203.90	17.375	173	241
SITE	30	3.00	1.438	1	5

Kruskal-Wallis Test

Ranks

	SITE	N	Mean Rank
MEASURE	1	6	17.00
	2	6	20.17
	3	6	13.50
	4	6	18.17
	5	6	8.67
	Total	30	

Test Statistics (a, b)

	MEASURE
Chi-Square	6.344
df	4
Asymp. Sig.	**.175**

a Kruskal Wallis Test
b Grouping Variable: SITE

Secondly, for the locations S1, QP2, and C3, which showed a normal distribution.

Using the non-parametric test Kruskal-Wallis the results were as follows:

```
NPAR TESTS
  /K-W=measure   BY site (1 3)
  /STATISTICS DESCRIPTIVES
  /MISSING ANALYSIS.
```

NPar Tests

Descriptive Statistics

	N	Mean	Std. Deviation	Minimum	Maximum
MEASURE	30	203.90	17.375	173	241
SITE	30	3.00	1.438	1	5

Kruskal-Wallis Test

Ranks

	SITE	N	Mean Rank
MEASURE	1	6	9.92
	2	6	10.92
	3	6	7.67
	Total	18	

Test Statistics (a, b)

	MEASURE
Chi-Square	1.169
df	2
Asymp. Sig.	**.557**

a Kruskal Wallis Test
b Grouping Variable: SITE

The final statistical test included locations C3, QP4 and S5, which also had a normal distribution and by using the non-parametric test Kruskal-Wallis, also.

```
NPAR TESTS
  /K-W=measure   BY site (1 3)
  /STATISTICS DESCRIPTIVES
  /MISSING ANALYSIS.
```

NPar Tests

Descriptive Statistics

	N	Mean	Std. Deviation	Minimum	Maximum
MEASURE	30	203.90	17.375	173	241
SITE	30	3.00	1.438	1	5

Kruskal-Wallis Test

Ranks

	SITE	N	Mean Rank
MEASURE	3	6	9.33
	4	6	13.17
	5	6	6.00
	Total	18	

Test Statistics (a, b)

	MEASURE
Chi-Square	5.426
df	2
Asymp. Sig.	**.066**

a Kruskal Wallis Test
b Grouping Variable: SITE

APPENDIX 2

SEM – EDAX – EDX AUTO

LINE SCAN PROFILE

a. From the **MAIN MENU**, select **EDX**.

b. Click on **EDX- Auto**

c. Set up – preset the clock for collection times (seconds).

d. **Image** – **collect**

e. Press **START** to collect spectrum. To automatically show identified elements, go to **ID - AUTO**

f. If you want to add other elements or subtract from the identified ones, select the desired elements and click on **add or remove/clear** elements from the screen.

g. **Image** - **collect** again for EDX Auto to pull the selected image from the microscope mode.

h. Click on **LOCA-S** – select **Line**. It will change to **LOCA-L**

i. Draw a line on the collected image across the desired location for analysis and click on save icon **S**.

j. Go to **LOCA-L** again and select **TABLE**

k. Under the cell corresponding to **No – X**, highlight the cell and change the number of points you want the line scan analysis along the line drawn. The default is **10**, if it is desired to run more than 10 spots along the line, change to X number and click on copy icon **C**, click **OK** to return.

l. Click on LOCA-L, select **Show all locations and numbers** for the locations to be analyzed to appear on the collected image.

m. Go to **LOCA-L** to save image for records, or go to **Photo-playback** to print it from the microscope mode.

n. Click on **Set up** – **Auto output** to name and save the file with a ".csv" spreadsheet extension, which is the one you will transfer to Microsoft Excel to view the results.

o. Go to **AUTO – SUMMARY** to save file with a ".smy" spreadsheet extension file, click **OK**. Note: if the file is note saved in with the SUMMARY option, the data will not be retrieved from the system.

p. Go to **SUMMARY** to check the line scan results.

APPENDIX 3

TYPICAL CSP PROCESS HOT ROLLING SCHEDULE

Figure 69 shows the CSP process hot rolling schedule followed for the simulation experiments for the kinetics of formation of star-like precipitates - steel E[110]

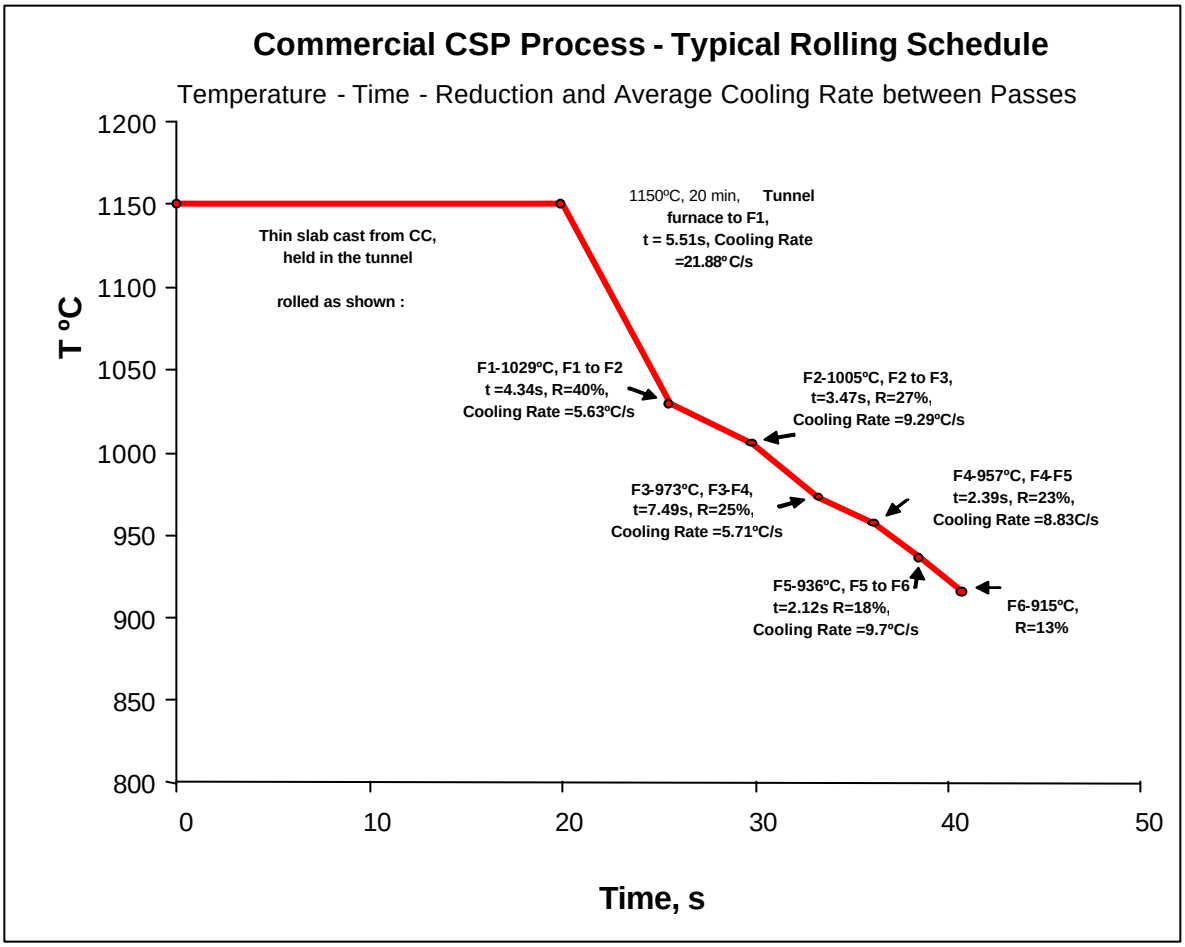

Figure 69 Schematic representation of the typical rolling schedule during the CSP processing of steel sheet

BIBLIOGRAPHY

1. D.T. Llewellyn and R.C. Hudd, *Steels: Metallurgy and Applications*, 3rd ed., Butterworth-Heinemann, London, 1998, ch. 1

2. K.P. Porotov, H.P. Mayorov, A.A. Skvortsov and A.D. Akimenko, *The Continuous Casting of Steel in Commercial Use*, Pergamon Press, London, 1960, Ch. 1

3. E.N. Simons, *Steel Castings*, Chemical Publishing Co., Inc., New York, 1947, Ch. 2

4. G.N. Fogel, *Continuous Production from Molten Metal*, Gosplanizdat, 1940

5. M.A. Boichenko, U.S. Rutes, N.A. Nocolayev, *Continuous Casting of Steel*, Izd. Akad. Nauk, SSSR, 1956

6. S.M. Boichenko, V.S. Rutes and V.V. Ful'makht, The Development of the Continuous Casting of Steel, Metallurg, No. 2, 1956

7. V.S. Rutes, N.A. Nicolayev and V.P. Druzhinin, *Investigation of the Continuous Casting Process*, Stal', No. 1, 1956

8. Continuous Casting of Steel, I.S.I. Special Report 184, 1977

9. W.C. Newell, *The Casting of Steel*, Pergamon Press, London and New York, 1985, Ch. 1

10. H.F. Taylor, E.A. Rominsky and C.W. Briggs; Trans. Amer. Foundry men Association, 1941, 49, 1

11. J.E. Worthington, Proc. Inst. Brit. Foundrymen, 1950, 43, A, 144

12. P.R. Beley, Iron and Steel, 1949, 22, 451

13. M.M. Wolf, "Hystorical Perspectives on Continuous Casting", Near Net Shape Casting in the Minimills, Proceedings of the International Symposium, Vancouver, B. C., Canada, 1995, pp 3-22

14. M.M. Wolf, “History of Continuous Casting”, Steelmaking Conference Proceedings, Vol. 75, 1992, pp 83-137

15. M.M. Wolf, “Advances in Clean Steel Technology”, Steel Times, Vol. 220, 1992, 408, pp 411-412

16. M.M. Wolf, “Strand Bending with Liquid Core-The Ultimate Solution is Concast Continuous Straightening”, Steels and Metals Magazine, VOl. 26, 1988, pp 325-329

17. A. Chatterjee and S. Chandra, “Thick, Thin, or Ultrathin – That is the Question in Slab Casting”, Steel World, Vol. 3, No. 2, pp 45-60

18. K. Wunnenberg and K. Schuerdtfeger, “Principles in Thin Slab Casting”, Iron and Steelmaker, April, 1995, pp 25-31

19. J.K. Brimacombe, “Empowerment with Knowledge-Toward the Intelligent Mold for the Continuous Casting of Steel Billets”, Iron and Steelmaker, Vol. 20, 1993, pp 35-47

20. J. Dzierzawski, “The Continuous Casting of Beam Blanks”, Technical Report Continuous Casting Plants, SMS Demag, 2001

21. M. Cygler and M.M. Wolf, “Continuous Strip and Thin Slab Casting of Steel – An Overview”, Iron and Steelmaker, Vol. 13, 1986, No. 8, pp 27-33

22. J.K. Brimacombe and I.V. Samarasekera, “The Challenge of Thin Slab Casting”, Iron and Steelmaker, Nov. 1994, pp 29-39

23. S.J. Cobo and C.M. Sellars, “Microstructural Evolution of Austenite under Conditions Simulating Thin Slab Casting and Hot Direct Rolling”, Ironmaking and Steelmaking, 2001, Vol. 28, No. 3, pp 230-236

24. B.A. Pollock, “The Flat Roll Minimill Boom Continuous”, Iron and Steelmaker, May 1995, pp 55-57

25. B. Cooper, “Who is doing What in Thin Slab Casting?”, Steel Times International, 1993, No. 1, pp 8-9

26. J.K. Brimacombe and I.V. Samarasekera, “Fundamental Aspects of the Continuous Casting of Near-Net-Shape Steel Products”, Proc. of the Int’l. Symp. On Casting of Near-Net-Shape Products, , Honolulu, Hawaii, , eds. Shahai et al., TMS, Warrendale, PA, 1988, pp 3-24

27. R.B. Mahapatra et al., “Mold Behavior and Its Influence on Quality in the Continuous Casting of Steel Slabs: Part I. Industrial Trials, Mold Temperature Measurements, and Mathematical Modelling,” Metall. Trans. B, Vol. 22B, 1991, pp 861-874

28. C. Zhou and R. Priestner, “ The Evolution of Precipitates in Nb-Ti Microalloyed Steels During Solidification and Post-solidification Cooling,” ISIJ International, Vol. 36, 1996, No. 11, pp 1397-1405

29. Y. Li, D.N. Crowther, P.S. Mitchel, and T.N. Baker, “The Evolution of Microstructure During Thin Slab Direct Rolling of V, Nb and Ti Microalloyed Steels,” Proceedings from the Materials Solutions Conference 2002, October 2002, Colombus, OH, USA, ASM International, pp 5-15

30. M. Prikryl, A. Kroupa, G.C. Weatherly, and S.V. Subramanian, “Precipitation Behavior in a Medium Carbon, Ti-V-N Microalloyed Steel,” Metallurgical and Materials Transactions A, Vol. 27A, May 1996, pp 1149-1165

31. H.J. Ehrenberg, L. Parschat, F.P. Pleschiutschnigg, W. Rahmfeld and C. Prosser, Casting and Cast-Rolling of Thin Slabs at the Mannesmannrohgren-Werke A. G.”, Metall. Plant and Tech. Intl., 1989, Vol. 12(3), pp 52-69

32. G. Holleis, A. Flick, and R. Welburn, “ CONROLL Technology for Integrated Compact Mills,” Near Net Shape Casting in the Minimills, Proceedings of the International Symposium, Vancouver, B. C., Canada, 1995, pp 305-325

33. K.L. Schwaha, A. Flick, and B. Lindorfer, “Near Net Shape Casting-A status report from VAI,” Proc. Conf. on Continuous Casting of Steel in Developing Countries, Beijing, China, The Chinese Society for Metals, 1993, pp 438-450

34. R. Gottardi, L. Nannini, and A.D. Martegani, “ Net and Near Net Shape Continuous Casting – New Developments in Minimills,” Metall. Plant and Tech. Intl., Vol. 15, No. 3, 1992, pp 428-437

35. R.B. Mahapatra, J.K. Brimacombe and I.V. Samarasekera, “Mold Behavior and Its Influence on Quality in the Continuous Casting of Steel Slabs: Part II. Mold Heat Transfer, Mold Heat Flux, Formation of Oscillation Marks, Longitudinal Off-corner Depressions, and Surface Cracks,” ,” Metall. Trans. B, Vol. 22B, 1992, pp 875-888

36. Y. Li, D.N. Crowther, P.S. Mitchel, and T.N. Baker, “The Evolution of Precipitation During the Processing of Thin Slab Cast Vanadium Microalloyed Steel,” HSLA Steels 2000 Conference Proceedings, 2000, pp 326-332

37 W. Loser, S. Thiem, and M. Jurisch, Materials Science and Engineering, 1993, A173, pp 323-326

38. P. Uranga, A.I. Fernandez, B. Lopez, J.M. Rodriguez-Ibabe, “Improvement of Microstructural Homogeneity in Thermomechanical Processed Nb Steels by Thin Slab Casting,” 43rd MWSP Conference Proceedings, ISS, VolXXXIX, 2001, pp 511-529

39. R. Kaspar, N. Zentara, and J.C. Herman, “Direct Charging of Thin Slabs, of a Ti-Microalloyed Low Carbon Steel for Cold Forming,” Steel Research 65, 1994, No. 7, pp 279-283

40. M.C. Flemmings, *Solidification Processing*, McGraw Hill, NY, 1974 Ch 1 p 6

41. C.R. Brooks, *Principles of the Austenitization of Steels,* Elsevier Applied Science, London and New York, 1992

42. W.C. Winegard, *An Introduction to the Solidification of Metals, Institute of Metals*, London, UK, 1964

43. B. Chalmers, *Principles of Solidification*, Wiley, New York, USA, 1964

44. C.R. Brooks, *Structure, Heat treatment and Properties on Non-Ferrous Alloys*, ASM, Park, OH, USA, 1982, Ch. 1

45. I. Minkoff, *Solidification and Cast Structure*, John Wiley and Sons Ltd., New York, 1986, Ch 2

46. A. Sauveur, *The Metallography and Heat Treatment of Steel*, 4th edition, The University Press, Cambridge, UK, 1935

47. P.S. Hurd, *Metallic Materials*, Holt, Rinehard and Winston, New York, USA, 1968

48. C.R. Brooks, *Principles of the Austenitization of Steels,* Elsevier Applied Science, London and New York, 1992, Ch 2, p 9

49 M.C. Flemings, *Solidification Processing*, McGraw Hill, NY, 1974 Ch 5 p 135

50. G.F. Vander Voort, *Metallography, Principles and Practice*, McGraw –Hill, New York, 1984, Ch 1, p 13

51. N.S. Pottore, “The Evolution of Microstructure during the Solidification and Subsequent Cooling of Low Alloy Steels, PhD Thesis, University of Pittsburgh, 1986

52. B. Bramfitt, Metals Handbook, Vol 9, 9th ed., ASM, Metals Park, OH, USA, 1985, p.624

53. M.C. Flemings, D R Poirer, D R Barone, and H D Brody, J Iron and Steel Institute, 208, 371, 1970

54. T.F. Bower, H.D. Brody, and M.C. Flemings, Trans AIME, 236:624, 1966

55. G. Flemming et al., "Rolling of Continuously Cast Strips and the Technical Consequences with Respect to the Design of Hot Strip Production Plants.", Metall. Plant and Tech., Vol. 11, 1988, pp. 16-35

56. B. Engl and C. Klinkenberg, "Influence of Thin Slab Casting on the Properties of Microalloyed Steels for Cold Forming Requirements", Materials Science Forum, Vols. 284-286, 1998, pp. 301-308

57. S.J. Cobo and C.M. Sellars, "Microstructural Evolution of Austenite under Conditions Simulating Thin Slab Casting and Hot Direct Rolling", Ironmaking and Steelmaking, 2001, Vol. 28, No. 3, p 234

58. E. Palmiere, "Suppression of Recrystallization during the Hot Deformation of Microalloyed Austenite," PhD Thesis, University of Pittsburgh, 1991

59. A.J. DeArdo, C.I. Garcia and E.J. Palmiere, "Thermomechanical Processing of Steel", *ASM Handbook, Vol. 4: Heat Treating*, ASM International, Materials Park, OH, 1991, pp 237-255

60. E.J. Palmiere, C.I. Garcia and A.J. DeArdo, "The Influence of Niobium Supersaturation in Austenite on the Static Recrystallization Behavior of Low Carbon Microalloyed Steels", *Met. Trans. A, Vol. 27A*, 1996, pp 951-960

61. W.A. Smith, *Structure and Properties of Engineering Alloys*, 2nd ed., McGraw Hill, 1993, pp 114-118

62. C. Dasarathy, and T.J. Goodwyn, Metals and Materials, 21, January, 1990

63. W.A. Smith, *Structure and Properties of Engineering Alloys*, 2nd ed., McGraw Hill, 1993, pp 119-123

64. A.J. DeArdo, ed., *IF Steels 2000 Conference Proceedings*, ISS Warrendale, 2000

65. W.B. Morrison, " Past and Future Development of HSLA Steels," *HSLA Steels '2000*, Beijing, China, 2000, p 11

66 L .. Cuddy, *Metall. Trans., Vol. 12A*, 1981, p 1313

67. E.J. Palmiere, C.I. Garcia and A.J. DeArdo, " Suppression of Static Recrystallization in Microalloyed Steels by Strain-Induced Precipitation", *International Symposium on*

Low-Carbon Steels for the 90's", edited by G Tither, The Minerals, Metals and Materials Society, 1993, pp 121-130

68. L.J. Cuddy and J.C. Raley, *Metall. Trans. A., 14A*, 1989 (1983)

69. A.C. Keissl, G. Posch, C.I. Garcia, and A.J. DeArdo, "Precipitation and Recrystallization During TMP of Complex Microalloyed HSLA Steels", *International Symposium on Low-Carbon Steels for the 90's", edited by G Tither, The Minerals, Metals and Materials Society,* 1993, pp 113-119

70. L.J. Cuddy, *Plastic Deformation of Metals*, Academic Press, New York, 1975, p 129

71. Y. Sakuma, D.K. Matlock, and G. Krauss, "Developments in the Annealing of Sheet Steels," The Minerals, Metals and Materials Society, 1992, p 131

72. O. Matsumura, Y. Sakuma, and H. Takechi, ISIJ International, 32, 1014, 1992

73. ASTM: A715-92a, Steel Sheet and Strip, Hot Rolled, High Strength, Low Alloy, with improved formability, Oct. 1993.

74. D.Q. Bai, S. Yue, T. Maccagno, J.J. Jonas, "Effect of Deformation and Cooling Rate on the Microstructure of Low Carbon Nb-B Steels", ISIJ International, 1998, N4, pp 371-379

75. J. Krauss, S.W. Thomson, "Ferritic Microstructures in Continuously Cooled Low and Ultra-Low Carbon Steels", ISIJ International, 1995 (35), N8, pp 937-945

76. S. Zajac, R. Lagneborg and T. Siwecky,"The Role of Nitrogen in Microalloyed Steels," Microalloying 95. Conference Proceedings, 1995, pp 331-338

77. W. Bleck, J.J. Esser, "Effect of Hot Charging on the Properties of Cold Forming Steels", Steel Times, 1995, pp 379-383

78. A.M. Sage, "An Overview of the Use of Microalloys on HSLA Steels with particular attention to Vanadium and Titanium", Proceedings of the 2nd International Conference on HSLA Steels, Processing, Properties and Applications, ed. by G Titer, TMS, Beijing, China, 1990, p 52

79. T. Gladman, *The Physical Metallurgy of Microalloyed Steels*, The Institute of Materials, London, UK, 1997, Ch 3, p 81

80. H. Nordberg and B. Aronsson, J. of the Iron and Steel Institute, 1968, 206, pp 1263

81. K. Narita, Trans. of the Iron and Steel Institute, Japan, 15, 147, 1975

82. T. Gladman, *The Physical Metallurgy of Microalloyed Steels*, The Institute of Materials, London, UK, 1997, Ch 3, p 102

83. T. Gladman, *The Physical Metallurgy of Microalloyed Steels*, The Institute of Materials, London, UK, 1997, Ch 5, p 206

84. T. Gladman, *The Physical Metallurgy of Microalloyed Steels*, The Institute of Materials, London, UK, 1997, Ch 5, p 207

85. S. Matsuda and N Okumura, *Trans. Iron and Steel Inst*., Japan, Vol. 18, 1978, p 198

86. G.C. Weatherly et al. "The Response of Carbonitride Particles in HSLA Steels to Mold Thermal Cycles,"

87. D.C. Houghton, G.C. Weatherly, and J.D. Embury, "Thermomechanical Processing of Austenite,"ed. A J DeArdo, G A Ratz and P J Wang, Met. Soc. AIME, 1982, p 267

88. B. Loberg, A. Nordgren, J. Strid and K.E. Easterling,"The Role of Alloy Composition on the Stability of Nitrides in Ti-Microalloyed Steels during Weld Thermal Cycles," Metall. Trans. A, Vol. 15, 33, 1984

89. J. Strid and K.E. Easterling, "On the Chemistry and Stability of Complex Carbides and Nitrides in Microalloyed Steels," Acta Metall., Vol 33, 1985, p 2057,

90. M.J. Crooks, A.J. Garratt-Reed, J.B. Vander Sande and W.S. Owen, "Precipitation and Recrystallization in Some Vanadium and Vanadium-Niobium Microalloyed Steels," Metall. Trans. A, Vol. 12, 1981, p1999

91. H.B. Aaron and G.R. Kotler, "Second Phase Dissolution," Metall. Trans. Vol. 2, 1971, p 351

92. R.A. Tranzilli and R.W. Heckel, " Numerical Solution to the Fine, Diffusion-Controlled, Two-Phase, Moving Interface Problem (with Planar, Cylindrical and Spherical Interfaces," Trans. Metall. Soc. AIME, Vol. 242, 1968, p 2313

93. N.K. Balliger and R.W.K. Honeycombe, *Met. Sci.* 14, 1980, p 121

94. G.L. Dunlop and R.W.K. Honeycombe, *Met. Sci*. 14, 1980, p 367

95. L. Kuchar and J. Drapala, "Solidus and Liquidus Curves and Distribution Coefficients of Admixtures in Iron and Prediction of the Solidification Interval in Low-Alloyed Steels," Hutchnike listy c. 4-7/2000, pp 59-66

96. A. Kothe, J. Kunze, G. Backmann and C. Mickel, "Precipitation of TiN and (Ti, Nb)(C, N) during Solidification, Cooling and Hot Direct Deformation," Materials

Science Forum, Vols. 284-286, Trans Tech Publications, Switzerland, 1998, pp 493-500

97. K.W. Andrews, D.J. Dyson, and S.R. Keown, *Interpretation of Electron Diffraction Patterns,* 2nd edition Plenum Press, New York, 1978, pp 228

98. B. Fultz and J.M. Howe, *Transmission Electron Microscopy and Diffractometry of Materials,* Springer, Germany, 2001. Ch 6, p 292

99. O. Dahmen, "Orientation Relationships in Precipitation Systems," Acta Metallurgica, Vol. 30, 1982, p 63

100. R. Kaspar and P. Flub, " Laboratory Simulation of the Direct Rolling of Steel," Steel Research, Vol. 62, 1991, pp 501 - 506

101. L. Kuchar, J. Drapala, and L. Kuchar Jr., "Distribution of Admixtures in Aluminum Alloys and Calculation of Solidification Interval," Transactions of the Universities of Kosice, 4/1999, pp 11-18

102. L. Kuchar, "Contribution of the Theory of Segregation During Primary Crystallization," Metallurgy, Refractories and Environment.

103. S.V. Subramanian and G.C. Weatherly, "Precipitate Evolution in Ti-Nb and Ti-V Microalloyed Steels," Thermec '97, The Minerals, Metals and Materials Society, 1997, pp 827 – 835

104. T. Gladman, *The Physical Metallurgy of Microalloyed Steels*, The Institute of Materials, London, UK, 1997, Ch 3, p 92

105. H.J. Jun, K.B. Kang and C.G. Park, "Effects of cooling rate and Isothermal Holding on the Precipitation Behavior during Continuous Casting of Nb-Ti Bearing HSLA Steels," Scripta Materialia, Vol. 49, 2003, pp 1081 - 1086

106. M.J. Cancio, G. Echaniz and T.E. Pérez, "Characterization of Microalloy Precipitates in the Austenitic Range of HSLA Steels," Steel Research 73(8), 2002, pp 340-346

107. T. Gladman, *The Physical Metallurgy of Microalloyed Steels*, The Institute of Materials, London, UK, 1997, Ch 3, p 82

108. R. Wang, Unpublished Research, University of Pittsburgh, Basic Metals Processing Research Institute (BAMPRI), 2003-2004

109. V. Thillou,"Precipitation of Nb in Ferrite in High Strength - Low Carbon - Low Alloy Steels," BAMPRI-University of Pittsburgh, PA, 1997, p 147 (Unpublished Research)

110. Y. Ma, Unpublished Research, University of Pittsburgh, Basic Metals Processing Research Institute (BAMPRI), 2003